NATURAL AND ARTIFICIAL IONOSPHERIC IRREGULARITIES IN THE AURORAL E REGION

A Dissertation

Presented to the Faculty of the Graduate School

of Cornell University

in Partial Fulfillment of the Requirements for the Degree of

Doctor of Philosophy

by

Robert J. Miceli

August 2015

NATURAL AND ARTIFICIAL IONOSPHERIC IRREGULARITIES IN THE AURORAL E REGION

Robert J. Miceli, Ph.D.

Cornell University 2015

Ionospheric irregularities are small-scale structures in plasma density aligned with the magnetic field that are formed by plasma instability processes and occur frequently in the auroral region of the ionosphere. Coherent scatter radar echoes from these irregularities convey information about the fine-scale structure of the auroral ionosphere during periods of geomagnetic activity. This subject has been studied extensively, however, the relationship between the coherent scatter spectral measurements and the ionospheric state parameters is not fully understood. Models of plasma waves, instability mechanisms, irregularities, and coherent echoes are required to further develop this understanding.

This thesis presents three studies of the auroral E region ionosphere that use radar measurements and computational models to understand the significance of radar backscatter from field aligned irregularities observed by a 30 MHz coherent scatter radar in Homer, Alaska. The first study models the Farley Buneman instability by combining the global, 2-D ionospheric model, SAMI2, with a local, heuristic model developed by *Milikh and Dimant* [2002]. The model estimates profiles of wave phase speed, magnetic aspect width, wave heating rates, and ionospheric state variables. This model shows promising agreement with incoherent scatter radar measurements from the Poker Flat Incoherent Scatter Radar (PFISR) and coherent scatter radar measurements from the Homer radar. The second study uses an empirical model to invert measured coherent scatter spectra into estimates

of convection velocity and then fits for the overall convection pattern. This model is informed by the simulations of *Oppenheim et al.* [2008]; *Oppenheim and Dimant* [2013] and formulas calculated by *Nielsen and Schlegel* [1985]. Comprehensive agreement between the convection velocity estimates and the convection pattern indicates an incompressible flow and validates the inversion. The third study examines E region ionospheric modification experiments that cause plasma instabilities and artificial irregularities. The study analyzes the threshold power needed to generate artificial irregularities due to the thermal parametric instability. SAMI2 was modified to simulate the propagation of the HF pump waves and their heating effects. The model revealed that active suppression of the artificial irregularities occurs entirely due to D region absorption. This thesis concludes with a summary of these studies and suggestions for future research.

BIOGRAPHICAL SKETCH

Robert Jonathan Miceli attended Half Hollow Hills High School West in Dix Hills, New York and graduated in June 2005. After completing high school, he attended Cornell University in Ithaca, New York to pursue his interests in engineering. He received a B.S. in Electrical and Computer Engineering in May 2009. He continued at Cornell University as a graduate student in the School of Electrical and Computer Engineering. After passing his A-exam, he was granted a M.S. degree, which was conferred in August 2013.

To my parents,

Donna and Robert

ACKNOWLEDGEMENTS

There are many people that need to be thanked for their contributions to this research. I would first like to acknowledge my advisor, Dave Hysell for his incredible insight, guidance, and patience. I am also very grateful for the advice and assistance from my committee members, Mike Kelley and Mark Psiaki. Their efforts and hard work improved this thesis as a result.

I am also indebted to Paul Kintner who introduced me to ionospheric research while I was an undergraduate. He unfortunately passed away too soon. His passion for research was inspirational, and I will never forget his dedication and humility. Special thanks to Muawia Barazangi for the coffee, countless advice, and failed efforts to convert me to seismology. Working with Steve Powell taught me an incredible amount about sounding rocket and GPS instrumentation. Additionally, I want to thank Jens Munk at the University of Alaska for his assistance with the Homer radar.

I owe many thanks to my family, friends, officemates, co-workers, and especially my girlfriend, Alex. I really could not have done this without them. Finally, I would like to thank my parents for their continuous love and support.

TABLE OF CONTENTS

LIST OF TABLES

LIST OF FIGURES

CHAPTER 1

INTRODUCTION

This thesis presents a detailed study of plasma density irregularities in the E region of the auroral ionosphere and the instability mechanisms that generate them. One way irregularities can form is through the Farley Buneman instability, which generates meter scale electrostatic plasma waves when the electron drift velocity relative to the ions exceeds a threshold velocity. Another way field aligned irregularities are generated is by artificially heating the ionosphere with high powered radio waves. Characteristics of these irregularities are observed with ground based radar and modeled computationally to understand the underlying physics for both instability mechanisms. The purpose of this research is to develop an understanding of the relationship between the parameters of unstable ionospheric plasma waves and their coherent scatter spectral measurements through computational models and inverse methods. This would allow coherent scatter radars and models of the plasma instabilities to be used as diagnostic instruments that can help to understand the fine structure in the auroral ionosphere.

1.1 Thesis organization

This chapter provides a general background of the ionosphere and more specifically, the auroral ionosphere. A short description of two instabilities, the Farley Buneman instability and the thermal parametric instability, are presented. These two instability processes are responsible for generating the field aligned irregularities that are studied in this thesis.

In Chapters 2 and 3, we review the experimental and theoretical history of

auroral ionospheric field aligned irregularities (FAIs). Chapter 2 covers radar and sounding rocket experiments, while Chapter 3 derives the dispersion relation for the Farley Buneman instability and the thermal parametric instability. Additionally, the features of SAMI2, a global ionospheric model, are outlined. SAMI2 is used as a basis for modeling artificial heating experiments and Farley Buneman wave propagation. Chapter 4 gives an overview of coherent and incoherent radar techniques and discusses the instrumentation used in this research. The central instrument used to study FAIs is a coherent scatter radar in Homer, Alaska. This radar is used for both natural and artificial field aligned irregularity (AFAI) experiments. The work up to this point constitute a review of existing knowledge, while the following chapters (Chapters 5, 6, and 7) represent new contributions.

In Chapter 5, a heuristic model of Farley Buneman waves is described, and the specific heuristic equations used in the model are presented and justified. The modeled results are discussed in detail, and their validity is evaluated using coherent and incoherent scatter radar measurements. Chapter 6 presents coherent scatter radar data and describes a technique to invert the Doppler spectra into estimates of the auroral convection speed and convection pattern.

Experimental analysis of an artificial heating experiment is presented in Chapter 7. The threshold to generate artificial irregularities is evaluated theoretically, and coherent scatter radar measurements are used to verify the theoretical estimate. A model of this ionospheric modification experiment is developed to determine how temperature influences the generation of AFAIs.

Finally, Chapter 8 concludes this thesis. It summarizes the main findings and gives recommendations for future work.

1.2 The ionosphere

The ionosphere is a thin shell of weakly ionized plasma that surrounds the surface of the Earth, where there are a significant number of free thermal electrons and ions greater than 1 eV in energy [*Schunk and Nagy*, 2009]. By this definition, the ionosphere extends from approximately 60 to 3000 km altitude. It is mainly formed by the ionization of neutral particles due to ultraviolet (UV), extreme ultraviolet (EUV), and X-ray radiation from the sun. A typical electron density profile for the daytime and nighttime ionosphere is shown in Figure 1.1. This thesis mostly focuses on the E region, which lies between approximately 90 and 150 km altitude and is mainly ionized by UV and X-ray radiation. The E region was the first to be discovered, and the regions above and below the E region were appropriately named the F and D regions, respectively. In the F region, electron density peaks at approximately 300 km and is mainly ionized by EUV radiation. In the D region, ionized particle density is low, and the neutrals tend to dominate the dynamics. Profiles of the electron, ion, and neutral particle densities are shown in Figure 1.2.

Currents in the ionosphere play an important role in the dynamics of charged particles and in the interaction between the magnetosphere-ionosphere system. This current is formed by differences in election and ion mobilities. In the F region, the ions are magnetized and they travel along the magnetic field lines at approximately the same velocity as the electrons, therefore, perpendicular electric fields, and currents are not easily formed in the region. In the E region, the velocity difference between the ions and electrons is large because the electrons travel at the $\mathbf{E} \times \mathbf{B}$ drift velocity and the ion motion is governed by collisions with neutral particles. The neutral particles in the E region have densities over a million times greater than the charged particles and have a large effect on the ion velocities since

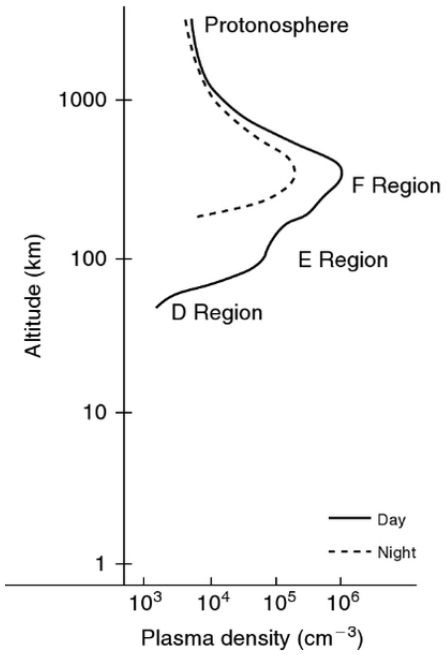

Figure 1.1: Typical day and nighttime electron density profiles. From *Kelley* [2009].

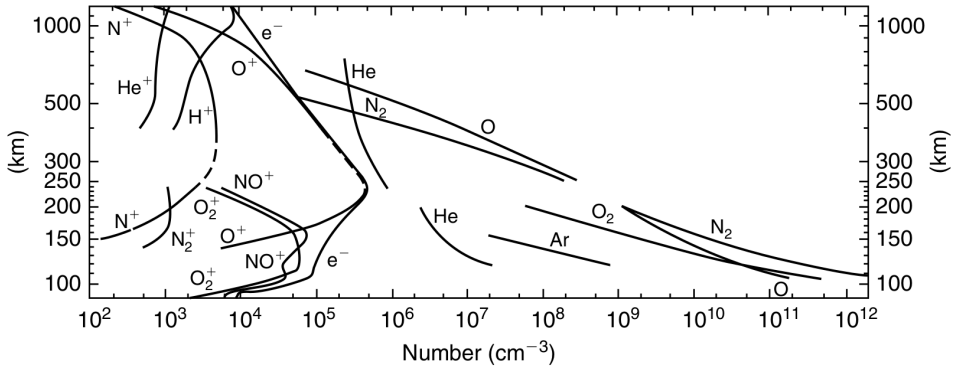

Figure 1.2: Ion, electron, and neutral densities from 100 to 1000 km. From *Johnson* [1969].

they have comparable mass. As a result of the large velocity differences, stronger currents form in the E region.

The current, $\mathbf{J}$, is related to the ion and electron velocities by

$$\mathbf{J} = ne(\mathbf{v}_i - \mathbf{v}_e) \tag{1.1}$$

where n is the electron density, e is the charge of an electron, $\mathbf{v}_i$ is the ion velocity, and $\mathbf{v}_e$ is the electron velocity. The current can also be expressed in the form of Ohm's law, $\mathbf{J} = \sigma \cdot \mathbf{E}$, where $\mathbf{E}$ is the electric field and σ is the conductivity tensor. Due to the finite conductivity in the ionosphere, an electric field forms when a current develops. The conductivity tensor, σ, is written as

$$\sigma = \begin{pmatrix} \sigma_P & -\sigma_H & 0 \\ \sigma_H & \sigma_P & 0 \\ 0 & 0 & \sigma_0 \end{pmatrix} \tag{1.2}$$

where the Pedersen conductivity, σ_P, the Hall conductivity, σ_H, and the parallel conductivity, σ_0, are given by [*Rishbeth and Garriott*, 1969]

$$\sigma_P = \frac{ne^2\nu_i}{m_i(\Omega_i^2 + \nu_i^2)} + \frac{ne^2\nu_e}{m_e(\Omega_e^2 + \nu_e^2)} \tag{1.3}$$

$$\sigma_H = \frac{ne^2\Omega_i}{m_i(\Omega_i^2 + \nu_i^2)} - \frac{ne^2\Omega_e}{m_e(\Omega_e^2 + \nu_e^2)} \tag{1.4}$$

$$\sigma_0 = \frac{ne^2}{m_i\nu_i} + \frac{ne^2}{m_e\nu_e} \tag{1.5}$$

Pedersen currents are aligned perpendicular to the magnetic field and parallel to electric field. Hall currents are aligned opposite the $\mathbf{E} \times \mathbf{B}$ direction. The parallel current is aligned parallel to magnetic field. The conductivities are dependent on the electron-neutral and ion-neutral collision frequencies, $\nu_{e,i}$, which has units of

rad/sec. They also depend on the electron density, n, and the electron and ion gyrofrequencies, given by

$$\Omega_{e,i} = \left| \frac{q_{e,i} B}{m_{e,i}} \right| \tag{1.6}$$

The conductivity tensor is anisotropic and inhomogeneous, and as a result, complex current and electric field structures form in the ionosphere. In the E region, $\Omega_e \gg \nu_e$ and $\Omega_i \ll \nu_i$. Physically, this means that the electrons tend to travel along the magnetic field lines, while the ions are mostly influenced by collisions with neutral particles and contribute to the Hall and Pedersen currents.

Profiles of typical daytime, mid-latitude conductivities are plotted in Figure 1.3. Conductivity parallel to the magnetic field lines is the largest, which allows electric fields in the magnetosphere to map into the lower E region. Reduced conductivity above and below the E region leads to an accumulation of charged particles at these boundaries. This causes the formation of large scale vertical electric fields. These fields are present globally during everyday, undisturbed conditions and provide the background conditions necessary for the formation of plasma instabilities. The region between 90 and 150 km, where the current is strongest, is called the auroral electrojet. A similar region exists in the equatorial ionosphere.

Chemistry is an important consideration in the auroral E region due to the low temperatures, molecular ions (NO^+,O_2^+, N_2^+), and weak ionization. Since recombination rates for molecular ions are significant, the E region density decreases quickly after sunset. The illustration of typical nighttime plasma densities in Figure 1.1 shows how the E densities can change from the daytime case. The reactions

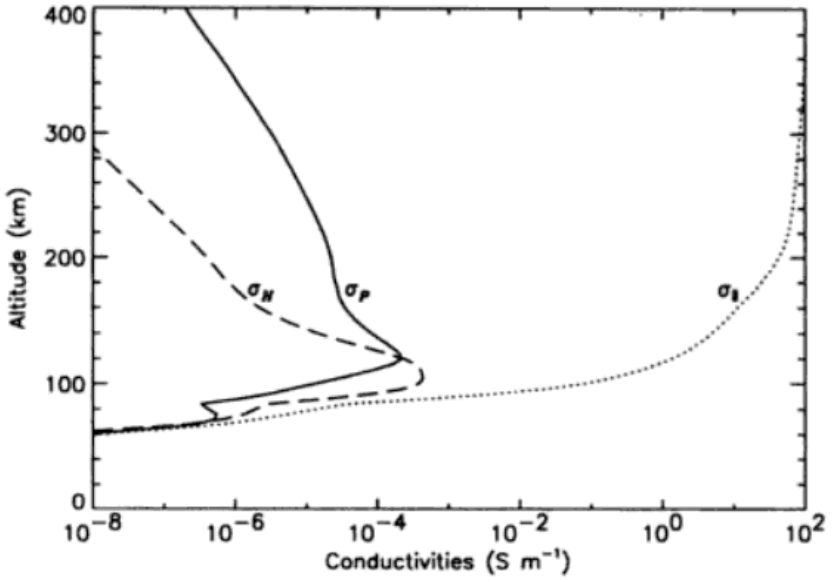

Figure 1.3: Mid-latitude, daytime Hall (dashed line), Pedersen (solid line), and parallel (dotted line) conductivity profiles from *Volland* [1995].

responsible for recombination in the E region include

$$NO^+ + e^- \rightarrow N + O \tag{1.7}$$

$$O_2^+ + e^- \rightarrow O + O \tag{1.8}$$

$$N_2^+ + e^- \rightarrow N + N \tag{1.9}$$

The recombination rates for these reactions are higher than the rates for atomic ions that exist at higher altitudes. Therefore, the density of the E region decreases rapidly once the photochemical ionization from solar radiation stops.

At night, plasma density can increase from convection from higher density regions or from energetic particle precipitation. Energetic electrons with energies of 3-10 keV are primarily responsible for most of the ionization, but protons, ions, and secondary electrons have some effect on the ionization of the neutral gas. Energetic particle precipitation is also responsible for visible light emissions that

form the visible aurora.

This visual aurora created an interest in the high latitude ionosphere centuries ago. Since its discovery, people have made observations of the aurora and tried to explain their existence. Since the late 1930s, radars have been popular instruments to remotely study the auroral ionospheric plasma. By probing the auroral ionosphere with radars, the backscatter of radio waves from ionospheric density irregularities was discovered and termed the radar aurora.

The occurrence of the optical aurora and radar aurora is interconnected and results from the dissipation of energy from the magnetosphere, which is coupled to the ionosphere. During geomagnetic storms, more energy is coupled to the E region of the ionosphere, and intense currents arise in the auroral electrojet. These strong currents ultimately lead to the Farley Buneman instability.

1.3 Farley Buneman instability

The Farley Buneman (F-B) instability [*Farley*, 1963; *Buneman*, 1963], or modified two-stream instability, is a mechanism that produces meter-scale electrostatic waves that propagate nearly perpendicular to the magnetic field in the Hall drift direction. They form when the electron drift velocity relative to the ions exceeds the ion-acoustic speed. This threshold is often met in the equatorial electrojet. It is not met as often in the auroral electrojet, but the relative electron drift velocity in the auroral zone during periods of geomagnetic activity is typically much larger than at the equator and Farley Buneman waves can occur.

The ion-acoustic speed is the threshold velocity to form Farley Buneman waves

and is defined as

$$C_s \equiv \sqrt{\frac{\gamma_e K_B T_e + \gamma_i K_B T_i}{m_i}} \tag{1.10}$$

where $\gamma_{e,i}$ is the ratio of specific heat for the electrons and ions, respectively, $T_{e,i}$ is the electron and ion temperature, respectively, m_i is the ion mass, and K_B is Boltzmann's constant. The ion acoustic speed in the E region is on the order of $\sim 350 - 400$ m/s and for electric fields of 20 mV/m, E/B is ~ 400 m/s at high latitudes. Since the ion acoustic speed depends on the electron and ion temperatures and their specific heat ratios which vary with altitude, the ion acoustic speed should not be taken to be fixed constant.

The linear theory of Farley Buneman waves describes many characteristics of the meter-scale irregularities described below. Different nonlinear theories have been developed to explain features like the small perpendicular orientation of the irregularities, waves propagating at large flow angles, or the saturation of the wave phase velocity near the ion-acoustic speed. These nonlinear theories will be discussed in Section 3.2.3.

1.3.1 Characteristics of the irregularities

Some of the main characteristics and features of irregularities discovered from experiment and theory are listed here. These experiments and theories will be discussed in more detail in Chapters 2 and 3, respectively.

1. The formation of the waves and irregularities depends on the electron drift velocity relative to the ions being greater than a threshold velocity that is close to the ion acoustic speed. This property was confirmed by many experiments and

predicted by the linear kinetic and fluid theories.

2. Another feature of the irregularities is that they are highly aspect sensitive. In the auroral ionosphere, the Earth's magnetic field lines are nearly perpendicular to the surface of the Earth. As the angle between the radar wave vector and the magnetic field decreases, the backscattered power drops off significantly. This suggests that the irregularities are strongly field-aligned and that the component of the wave vector perpendicular to the geomagnetic field is much larger than the parallel component.

3. The Doppler spectra of the backscattered signal generally have either large Doppler shifts with narrow spectra or a broader spectra with small Doppler shifts.

4. The strongest echoes come from low elevation angles. Since the auroral irregularities are strongly aligned with the magnetic field, the experimental geometry for a high latitude radar requires that it is located equatorward of the irregularities and must operate at low elevation angles. This implies that the irregularities are travelling nearly parallel to the electron drift velocity.

5. Coherent scatter radar experiments have shown that the echo strength and Doppler shifts vary with flow angle (the angle between the wavevector and the radar line of sight). Experiments and simulations have shown that the observed Doppler shifts are proportional to the wave phase velocity times the cosine of the flow angle, and the spectral widths are proportional to the phase velocity times the sine of the flow angle.

1.4 Thermal parametric instability

Field aligned irregularities can also be generated artificially by an electromagnetic O-mode pump wave through the process of the thermal parametric instability. *Vaskov and Gurevich* [1975] first discovered that these artificial plasma irregularities in the F region could be generated by O-mode waves and that they were strongly aligned with the magnetic field at altitudes close to the upper hybrid resonance height. The instability process originates when a transmitted electromagnetic wave encounters an initial density irregularity in the ionosphere and the wave scatters into electrostatic waves. These waves are primarily upper-hybrid waves that propagate perpendicular to the magnetic field. Wave heating then causes the electrostatic waves to grow in amplitude, starting the instability process.

The thermal parametric instability is similar to the Farley Buneman instability in that it requires a minimum threshold electric field to excite the instability that, in turn, generates field aligned irregularities. The major difference is that the thermal parametric instability is driven by artificial electromagnetic pump waves. *Dysthe et al.* [1983] theoretically calculated the threshold, growth rate, and spatial scale for the thermal parametric instability in the F region. *Hysell et al.* [2010] modified these calculations for the E region.

Previously, heating experiments were difficult to perform in the E region due to the low pump mode frequencies required to match the upper-hybrid resonance height. The HAARP facility was the first facility of its kind to transmit at such low frequencies. Chapter 7 presents data from these E region experiments that evaluate the threshold of the thermal parametric instability, as well as a model of the O-mode and X-mode waves to study their effects on the ionospheric plasma.

CHAPTER 2

EXPERIMENTAL BACKGROUND

Most of the knowledge of plasma density irregularities comes from observations from radars and sounding rockets. Radars provide measurements of the Doppler spectra of plasma irregularities with scale sizes that are equal to half of the radar wavelength. The spatial resolution of a radar is typically several kilometers. Sounding rockets provide measurements in-situ with very fine spatial resolution (less than a meter), but only for a short period of time and within a small volume. They are capable of measuring the entire spectrum of plasma irregularities. This chapter outlines the history of auroral E region experiments using radars and sounding rockets.

2.1 Radar experiments

The first observations of radar backscatter in the auroral E region were made by *Eckersley* [1937] and *Harang and Stoffregen* [1938]. Using a 9 MHz coherent scatter radar with a pair of receiving antennas spaced 20 m apart, Eckersley measured coherent backscatter and calculated that the echoes were reflected between 100 and 300 km altitude. The phase difference of the backscattered signal was measured between the two antennas and was used to determine the angle of arrival. Harang and Stoffregen observed other echoes as well, but calculated that the echoes originated at higher equivalent heights between 850 km and 1,600 km.

Experiments performed several years later at VHF provided more insight into the radar echoes. *Lovell et al.* [1947] recorded backscatter measurements at VHF frequencies (46 MHz and 72 MHz) and were able to estimate the electron density

in the region, since backscatter was visible on the 46 MHz radar, but not on the 72 MHz frequency. This meant that the critical frequency (the lowest frequency where incident waves penetrate through the ionosphere and are not reflected) was between these two frequencies. The range of electron densities were then estimated from these frequencies using the relation

$$N_e = 1.24 \times 10^{-8} f^2 \tag{2.1}$$

where N_e is the electron density in cm^{-3} and f is the critical frequency of the ionosphere.

At this time, the origin of these echoes was unknown. *Bowles* [1954] recorded the Doppler spectrum of auroral echoes and found that the Doppler shifts of the echoes did not correlate with changes in their range. Due to the geometry of an auroral radar, this implied that the backscatter was aligned with the Earth's magnetic field. Several experiments were performed to determine whether the location of the echoes was related to the location of the visual aurora. Using pulsed transmissions at 35 and 74 MHz, *Harang and Landmark* [1954] found that the presence of echoes was closely connected to geomagnetic activity, but the range of the coherent echoes did not correlate with the position of the aurora in space. They also directed their antennas directly towards visible aurora and measured no backscatter. Other experiments by *Bullough and Kaiser* [1954] and *McNamara* [1955] contradicted the previous study and reported that the echoes were due to direct reflection from large auroral arcs. This lead to several theoretical models of the ionosphere to explain the observed Doppler spectra.

Soon after, it was explained by *Booker* [1956] through theory and modelling that the observed echoes from VHF experiments were reflected from plasma density irregularities aligned with the magnetic field. Additionally, the spatial scales of the

irregularities were modeled and estimated to be roughly 5 to 10 m in length along the magnetic field and less than 1 m transverse to the magnetic field. *Flood* [1960] conducted experiments to confirm Booker's work with 3 VHF radars to study the wavelength dependence of auroral echoes and found that measurements of the irregularity scale size agreed with Booker's model, after accounting for absorption.

Bowles et al. [1963] conducted experiments with the Jicamarca incoherent scatter radar at the magnetic equator and found similar echoes arising from plasma density irregularities aligned with the magnetic field. The development of these irregularities was theorized to be the result of the Farley Buneman waves [*Farley*, 1963; *Buneman*, 1963]. The theory of these waves, the associated instability process, and the resulting density irregularities will be discussed in more detail in the next chapter.

Leadabrand et al. [1965] performed experiments at VHF and UHF and showed that the field aligned irregularities existed in the altitude range between 100 and 130 km. Further experiments using interferometry found that the echoes arrive from 95 to 125 km altitude [*Unwin*, 1967; *Sahr et al.*, 1991]. At VHF, Bragg-like backscatter from the ionosphere implies meter-scale density irregularities. Analysis of backscatter at different frequencies has shown that the dominant wave number for Farley Buneman waves is approximately 1 m^{-1}.

The characteristics of the radar backscatter echoes have been classified based on the shape of the Doppler spectrum. Type 1 echoes have Doppler shifts close to the ion acoustic speed and narrow spectral widths. They are observed when the electron convection speed is greater than the ion acoustic speed. For small flow angles (the angle between the radar line-of-sight and the electron convection), the measured backscatter is more intense. Type 2 echoes are broader and have smaller

Doppler shifts, in some circumstances close to the line of sight electron drift speed. *Balsley and Farley* [1971] discovered that, in the equatorial region, type 1 echoes were observed more often for higher frequency radar signals (146.25 MHz) with relatively constant strength across all frequencies, while type 2 echoes occurred more often at lower frequencies (16.25 MHz) with higher strength at lower frequencies. They also proposed that the type 2 irregularities were excited from nonlinear interactions with the larger irregularities. The relationship between the wave phase velocities at different frequencies roughly agreed with the linear theory.

It was generally thought that type 1 and 2 echoes arose from Farley Buneman instability and gradient drift instability, respectively. This nomenclature has been also used to characterize type 3 and 4 echoes, which are similar to type 1 echoes but have Doppler shifts above or below the ion acoustic speed. However, this naming convention has been used inconsistently as discussed in *Sahr and Fejer* [1996], and we will refrain from using this terminology.

Irregularities have been observed at high latitudes when the ambient perpendicular electric field exceeds approximately 20 mV/m, corresponding to drift velocities of 400 m/s, although this threshold has been shown experimentally to vary based on the frequency of the radar. *Siren et al.* [1977] observed significant backscatter with their 50 MHz radar when the electric field was as low as 10 mV/m in the morning hours, while *Moorcroft* [1979] reported that the threshold was closer to 20 mV/m for observations with a 398 MHz radar for morning observations. In the evenings, the threshold electric field was observed to be about 30 mV/m using the same 398 MHz frequency [*Tsunoda and Presnell*, 1976].

Experiments performed at the VHF (140 MHz) Scandinavian Twin Auroral Radar Experiment (STARE) radar estimated electron drift velocity vectors by

combining the radial Doppler velocity measurements from the overlapping volumes of two radars [*Nielsen and Schlegel*, 1983]. For small convection velocities (< 700 m/s), the electron convection speeds estimated by STARE were consistent with ISR measurements of the convection velocity. For larger velocities, the convection velocity was routinely underestimated. This suggested that Farley Buneman wave phase velocities were limited to the ion acoustic speed, which is not predicted by the linear Farley Buneman instability theory. Additionally, analysis of the spectral widths showed that narrow spectra corresponded to small flow angles, while broad spectra were measured at large flow angles. One issue that these experiments faced was the poor spatial resolution of the common volumes (~ 50 km) of the STARE radar. This resolution is much larger than the spatial scales of the convection pattern, and the poor resolution may have had some impact on the results.

Using observations from the STARE coherent scatter radar and the EISCAT incoherent scatter radar, *Nielsen and Schlegel* [1985] determined an algorithm that predicted electron drift velocities from Doppler measurements obtained from STARE for small flow angles. Additionally, they showed that the wave phase speed was limited to the ion acoustic speed and argued that this was due to wave heating by Farley Buneman waves.

Many experiments have been performed to evaluate the relationship between the measured Doppler shift and the flow angle. This topic has been contentious and experiments have often produced contradictory results. Doppler spectra of E region irregularities have been observed by numerous coherent scatter radars at HF, VHF, and UHF, and the characteristics of the measured Doppler spectra change depending on the radar frequency. *Hanuise* [1983] analyzed E and F re-

gion irregularities using data from 13 radars at different frequencies between HF and UHF. The analysis found that the Doppler shifts of the echoes at VHF were proportional to the electron convection speed and varied as a function of the cosine of the flow angle. Additionally, the measured Doppler velocities were not limited by the ion acoustic speed. At UHF, Doppler measurements plateaued near the ion acoustic speed at extreme flow angles and monotonically varied in between these two regions. *Reinleitner and Nielsen* [1985] reinterpreted the Doppler velocity measurements from *Nielsen and Schlegel* [1985] and proposed that for small flow angles, the Doppler velocities were limited to the ion acoustic speed, while at large flow angles, the Doppler velocities were proportional to the convection speed times the cosine of the flow angle. This analysis assumed L-shell flow invariance over the entire radar field of view, although the magnetic field is always in a disturbed state when Farley Buneman waves are present.

Haldoupis and Schlegel [1990] highlighted the importance of considering a non-isothermal, temperature dependent ion acoustic speed, i.e., $\gamma_e \neq 1$ and $\gamma_i \neq 1$ in Equation (1.10). They found that $\gamma_e = 5/3$ and $\gamma_i = 1$ provided the best agreement between the phase velocity and ion acoustic speeds for 1 m waves, although no conclusive evidence was found to support one set of specific heat ratios.

Much confusion existed since the Jicamarca ISR measured Doppler spectra of Farley Buneman waves that propagated at the ion acoustic speed at any look angle in the east-west plane [*Bowles et al.*, 1960]. This is quite different in the auroral zone, where the waves generally propagated slower than the ion acoustic speed depending on the look angle. *Kelley et al.* [2008] resolved this by showing that the vector sum of the zero order electric field and the electric field due to large scale waves exceeds the acoustic threshold for any look angle near the equator. Such

large scale waves are very rare at high latitudes.

A portable 50 MHz coherent scatter radar called the Cornell University Portable Radar Interferometer (CUPRI) traveled to several high latitude and equatorial locations to study Farley Buneman waves. CUPRI has also performed simultaneous experiments with incoherent scatter radars and for sounding rocket campaigns [*Providakes et al.*, 1988; *Sahr et al.*, 1992]. The major findings from the CUPRI experiments verified that there is a small component of the parallel electric field which significantly contributes to anomalous electron heating.

The Super Dual Auroral Radar Network (SuperDARN) consists of over 30 HF coherent scatter radars that are primarily used to estimate the F region convection pattern at high latitudes [*Greenwald et al.*, 1995; *Greenwald*, 1996]. The radars have overlapping fields of view, which allows them to make vector velocity measurements and to estimate the overall convection pattern. Although the echoes mostly come from the F region, the radars also acquire backscatter from the E region. *Makarevich* [2008] analyzed three years of coherent backscatter from the auroral E region and found that electric field and magnetic aspect angle strongly influence echo occurrence in agreement with the linear theory.

As pointed out by [*Sahr and Fejer*, 1996], there are several challenges with conducting radar experiments and interpreting the data. Signal processing imposes some problems that can be addressed by compromising time/frequency resolution or range certainty/Doppler ambiguity. Additionally, different results from different radars could be shaped by the instrumentation or methodologies, which makes discerning the underlying plasma physics challenging. Other concerns include determining the angle of arrival or azimuth of the backscatter and separating the desired signal from interference and ground clutter.

In summary, the radar experiments described in this section have discovered many characteristics of radio aurora, field aligned irregularities, and the mechanisms that form these structures. The irregularities are strongly field aligned, exist between 95 and 125 km, are predominantly meter-scale, and often occur in conjunction with the visual aurora and with strong ionospheric currents. Farley Buneman waves are observed only when the electric field is greater than approximately 20 mV/m and have apparent phase velocities near the ion acoustic speed (300 to 500 m/s), although velocities greater than 1500 m/s have been observed.

2.2 Sounding rocket experiments

Sounding rockets provide in-situ measurements of Farley Buneman waves and have contributed a great deal of information about the auroral E region. They can directly measure the magnetic and electric fields, background density, and fluctuation density along the trajectory of the rocket.

Sounding rocket campaigns that focused on understanding the auroral E region began in the mid-1960s. Soon after, evidence for Farley Buneman waves was discovered. *Kelley and Mozer* [1973] measured oscillating electric fields and plasma density fluctuations with meter-scale wavelengths in the E region. Electric field probes indicate that density irregularities occur when the background electric field exceeds about 20 mV/m. Additionally, these waves propagated in the same direction of the electron convection speed, but with lower velocity, closer to the ion acoustic speed, as defined in Equation (1.10). This evidence supports the theory that non-linear wave interactions are responsible for slowing down the waves and maintaining marginal stability. These results were confirmed by *Holtet* [1973];

Bahnsen et al. [1978].

Ogawa et al. [1976] analyzed the observations of six sounding rockets launched from Antarctica between 1972 and 1973. Fluctuations in the electron density, $\langle \delta N \rangle$, were observed between 90 and 120 km in altitude with relative amplitudes of 10% of the background density and scale sizes from 5 to 200 m. These results were reported to be consistent with the linear theory for the Farley Buneman instability. *Pfaff et al.* [1984] reported similar results using data from rockets launched in the northern hemisphere.

Sounding rocket experiments were jointly conducted with coherent and incoherent scatter radars to measure a common volume of space along the trajectory of the rocket [*Pfaff et al.*, 1992; *Rose et al.*, 1992]. These campaigns confirmed that the data recorded in situ were consistent with coherent backscatter measurements. Spectral analysis by *Pfaff* [1995] showed that most of the energy was in the primary waves that propagated in the direction of the electron drift. However, the wave phase speed was consistently less than the convection speed. Secondary waves were also observed, but with less energy. These secondary waves propagate perpendicular to the primary waves and are generated by nonlinear wave interactions. They will be discussed in more detail in Section 3.2.3.

Additional findings from sounding rocket observations include: 1) The electric field is strongly aligned normally to the magnetic field, as predicted by linear theory. 2) Different spatial structure exists on the upper and lower altitude limits of the instability region [*Pfaff et al.*, 1992]. 3) In addition to meter-scale waves, spectral analysis also reveals hundred-meter and kilometer scales that exist within the irregularity region. 4) Irregularities mainly occur in or next to regions of particle precipitation.

The Joint Observations of Upper Latitude Electrodynamics (JOULE) campaign was conducted to measure vector electric fields and plasma densities with two instrumented sounding rockets, neutral winds with two chemical release rockets, and fine structure in the auroral convection pattern with a ground-based, 30 MHz coherent scatter radar [*Bahcivan et al.*, 2005]. Electric fields greater than 20 mV/m were measured along the trajectory of both instrumented spacecraft. The ground-based radar observed strong coherent backscatter corresponding to the same periods when the rockets measured an electric field above threshold. Additionally, the radar recorded both broad and narrow Doppler spectra. The Doppler shifts of the auroral echoes were found to be proportional to the ion acoustic speed times the cosine of the flow angle.

The JOULE II sounding rocket was launched into different ionospheric conditions and confirmed the results of the JOULE experiment [*Hysell et al.*, 2008a]. Irregularities during the first JOULE campaign were stronger, located at higher altitudes, and had a larger range of flow angles than during JOULE II. The radar measured only broad Doppler spectra as a result of the smaller range of flow angles. However, the radar data was still in agreement with the rocket observations.

CHAPTER 3

THEORETICAL BACKGROUND AND MODELING

This chapter presents an introduction to auroral E region irregularities which result from the Farley Buneman instability. First, kinetic and fluid linear theory for the instability is derived, and then improvements and non-linear extensions to the theory are discussed. Finally, the chapter summarizes recent work in modeling and simulations of Farley Buneman waves and gives an overview of the SAMI2 model of the ionosphere, which has been modified to model certain aspects of Farley Buneman waves or artificial wave heating. The specific changes to SAMI2 for modeling each experiment will be discussed in later chapters.

3.1 Auroral *E* region irregularities

Energy from the solar wind is coupled with the Earth's magnetosphere which, in turn, is coupled with the auroral E region ionosphere. The energy flow from the solar wind to the magnetosphere is the greatest when the interplanetary magnetic field is oriented southward. The magnetosphere transports this energy to the ionosphere by either accelerating particles to high energies or by driving currents along magnetic field lines. In the former case, when the high energy particles precipitate down the magnetic field, they excite particles in the ionosphere, resulting in optical emissions commonly referred to as the aurora. In the latter case, when current flow increases along the magnetic field lines, extra energy is dissipated through the resistive ionosphere by Joule heating. The increased current that arises in the auroral electrojet also drives instability processes which then generate density irregularities aligned with the magnetic field.

The instability mechanisms responsible for generating the irregularities were not well understood until *Farley* [1963] and *Buneman* [1963] derived the dispersion relations for the E region plasma waves. The linear theory they derived explains why the waves become unstable when the relative electron-ion drift speed exceeds the ion acoustic speed of the medium. However, many properties of the waves observed by coherent scatter radars were not completely explained by the linear theory. As a result, many quasilinear and nonlinear theories along with numerical simulations have been developed to account for experimental observations.

3.2 Farley Buneman wave theory

Farley Buneman waves form when the Hall drift of magnetized electrons is strong enough to generate an electric field that causes a polarization drift in the ions. These drifts enhance density irregularities, and when they overcome diffusion, the wave growth becomes unstable, and the mean state of the ionosphere is modified through wave heating and quasilinear diffusion [*St.-Maurice et al.*, 1981a; *Milikh and Dimant*, 2002; *Dimant and Milikh*, 2003; *Milikh and Dimant*, 2003]. The waves were first discovered in the equatorial electrojet and later found in the auroral electrojet by *Eckersley* [1937] and in mid-latitudes by *Schlegel and Haldoupis* [1994].

3.2.1 Linear theory

The dispersion relation for Farley Buneman waves was first derived by *Farley* [1963] and *Buneman* [1963]. Farley's method involved kinetic theory, while Buneman

used fluid theory. Both theories predict similar dispersion relations for wavelengths greater than about 50 cm. The main differences are (1) the kinetic theory predicts a finite growth rate that peaks at a specific wavelength, around 2-3 m [*Kelley*, 2009], while the fluid theory predicts infinite growth as the wavelength decreases and (2) the kinetic theory predicts lower wave frequencies than the fluid theory, which implies slower phase velocities. It will be shown later that the kinetic theory produces more realistic results at shorter wavelengths because it does not ignore the effects of ion Landau damping.

Linear fluid theory

The linear fluid theory derivation begins with the continuity and momentum equations for electrons and ions

$$\frac{\partial n_\sigma}{\partial t} + \nabla \cdot (n_\sigma \mathbf{u}_\sigma) = 0 \tag{3.1}$$

$$\frac{\partial \mathbf{u}_\sigma}{\partial t} + (\mathbf{u}_\sigma \cdot \nabla)\mathbf{u}_\sigma = -\nu_{\sigma n}\mathbf{u}_\sigma + \frac{q}{m_\sigma}(\mathbf{E} + \mathbf{u}_\sigma \times \mathbf{B}) - \frac{K_B T}{m_\sigma}\nabla \ln n_\sigma \tag{3.2}$$

where σ denotes either electrons or ions, n is the species density, $\mathbf{u}$ is the particle velocity, ν is collision frequency with neutrals, q is the electron charge, m is the particle mass, $\mathbf{E}$ is the electric field, $\mathbf{B}$ is the magnetic field, K_B is Boltzmann's constant, and T is the temperature. To satisfy quasineutrality, $n_\sigma = n_e = n_i$.

Linearizing the continuity equation, we expand the density and velocity terms to a background and perturbation value, i.e. $n = n_0 + n_1$. For the electrons, the continuity equation becomes

$$\frac{\partial n_1}{\partial t} + \mathbf{V}_{e0} \cdot \nabla n_1 + n_0 \nabla \cdot \mathbf{u}_{e1} + \frac{n_0 \mathbf{u}_{e0}}{L} = 0 \tag{3.3}$$

where L is the background transverse plasma density gradient scale length and the

term $\mathbf{V}_{e0}$ is the electron convection velocity. We assume that the term $\nabla\cdot(n_0 u_{e0}) = n_0 u_{e0}/L$. For the ions, we assume the background ion drift is zero and the linearized continuity equation becomes

$$\frac{\partial n_1}{\partial t} + n_0 \nabla \cdot \mathbf{u}_{i1} = 0 \tag{3.4}$$

In the auroral zone, the electrons are inertialess and magnetized, while the ions have considerable mass and are unmagnetized. Taking this into account, the linearized momentum equations are given by

$$0 = \nu_{en}\mathbf{u}_{e1} - \frac{q}{m_e}(\mathbf{E}_1 + \mathbf{u}_{e1}\times\mathbf{B}_0) - \frac{K_B T_e}{m_e}\nabla n_1 \tag{3.5}$$

$$\frac{\partial \mathbf{u}_{i1}}{\partial t} = -\nu_{in}\mathbf{u}_{i1} + \frac{q}{m_i}\mathbf{E}_1 - \frac{K_B T_i}{m_i}\nabla n_1 \tag{3.6}$$

Solving Equation (3.5) for the components of electron velocity,

$$u_{e1x} = \frac{eE_y}{m_e\Omega_e} - \frac{e\nu_{en}E_x}{m_e\Omega_e^2} - \frac{\nu_{en}K_B T_e}{m_e\Omega_e^2}\frac{\partial n_1}{\partial x} + \frac{K_B T_e}{m_e\Omega_e}\frac{\partial n_1}{\partial y} \tag{3.7a}$$

$$u_{e1y} = \frac{eE_x}{m_e\Omega_e} - \frac{e\nu_{en}E_y}{m_e\Omega_e^2} - \frac{\nu_{en}K_B T_e}{m_e\Omega_e^2}\frac{\partial n_1}{\partial y} - \frac{K_B T_e}{m_e\Omega_e}\frac{\partial n_1}{\partial x} \tag{3.7b}$$

$$u_{e1z} = -\frac{eE_\parallel}{m_e\nu_{en}} - \frac{K_B T_e}{m_e\nu_{en}}\frac{\partial n_1}{\partial z} \tag{3.7c}$$

Assuming that the fluctuations in the density, electron and ion velocity, and the electric field are proportional to $\exp[i(\omega t - \mathbf{k}\cdot\mathbf{r})]$, we can substitute the electron velocity above into Equation (3.3) to obtain

$$\left(1 + \frac{\Omega_e}{\nu_{en}L}\right)^{-1}[i\omega\tilde{n} - i\mathbf{V}_{e0}\cdot\mathbf{k}\tilde{n}] + \tilde{n}\frac{\lambda\nu_{en}}{\Omega_e^2}\frac{K_B T_e}{m_e}k_\perp^2 + i\frac{\lambda\nu_{en}}{B_0\Omega_e}\tilde{E}_\perp k_\perp = 0 \tag{3.8}$$

where

$$\lambda = 1 + \frac{\Omega_e^2}{\nu_{en}^2}\frac{k_\parallel^2}{k_\perp^2} \tag{3.9}$$

and where the quantities $\tilde{n} = n_1$ and $\tilde{E} = E_1$ represent the magnitude of the fluctuations.

Solving Equation (3.4) for the ion velocity and substituting the result into Equation (3.6) gives

$$i\omega(i\omega + \nu_{in})\tilde{n} + \frac{K_B T_i}{m_i} k^2 \tilde{n} - i\frac{\Omega_i}{B_0}\tilde{E}_\perp k_\perp = 0 \tag{3.10}$$

Multiplying Equation (3.10) by $\lambda\nu_{en}/\Omega_e\Omega_i$ and combining it with Equation (3.8) yields the dispersion relation

$$\omega - \mathbf{k}\cdot\mathbf{V}_{e0} = \frac{\psi}{\nu_{in}}\left[-\omega(i\omega + \nu_{in}) + ik_\perp^2 C_s^2\right]\left(1 + i\frac{k_\perp \Omega_e}{k^2 \nu_{en} L}\right) \tag{3.11}$$

where $C_s^2 = K_B(\gamma_i T_i + \gamma_e T_e)/m_i$ is the ion acoustic speed squared and $\gamma_{e,i}$ is the ratio of specific heat for electrons or ions. The term ψ represents the anisotropy of the wave propagation and is defined as $\psi \equiv \psi_o[1 + (\Omega_e^2/\nu_{en}^2)(k_\parallel^2/k_\perp^2)]$ with $\psi_o \equiv \nu_{en}\nu_{in}/\Omega_e\Omega_i$.

By substituting ω with $\omega_r + i\gamma$ in Equation (3.11), the Farley Buneman wave frequency and growth rate can be expressed as

$$\omega_r = \frac{\mathbf{k}\cdot\mathbf{V}_{e0}}{1+\psi} \tag{3.12}$$

$$\gamma = \frac{1}{1+\psi}\left[\frac{\psi}{\nu_{in}}(\omega_r^2 - k^2 C_s^2) - \frac{\nu_{in}}{\Omega_i L}\frac{k_\perp}{k^2}\omega_r\right] \tag{3.13}$$

To account for the background ion drift, we replace $\mathbf{V}_{e0}$ with $\mathbf{V}_{e0} - \mathbf{V}_{i0}$ and ω_r with $\omega_{ir} \equiv \omega_r - \mathbf{k}\cdot\mathbf{V}_{i0}$.

$$\omega_r = \frac{\mathbf{k}\cdot(\mathbf{V}_{e0} - \mathbf{V}_{i0})}{1+\psi} + \mathbf{k}\cdot\mathbf{V}_{i0} \tag{3.14}$$

$$\gamma = \frac{1}{1+\psi}\left[\underbrace{\frac{\psi}{\nu_{in}}(\omega_{ir}^2 - k^2 C_s^2)}_{\text{FB}} - \underbrace{\frac{\nu_{in}}{\Omega_i L}\frac{k_\perp}{k^2}\omega_{ir}}_{\text{GD}}\right] \tag{3.15}$$

This dispersion relation predicts many of the features of Farley Buneman waves that are observed in nature. The first term in the brackets, labeled "FB", is associated with the Farley Buneman instability, while the second term, labeled "GD", is associated with the gradient drift instability. In the absence of a vertical density gradient, i.e., $L \to \infty$, pure two stream waves will form, and Equation (3.15) predicts that wave growth will occur when the relative electron-ion phase velocity, ω_{ir}/k, exceeds the ion acoustic speed. The assumption of magnetized electrons and unmagnetized ions restricts the altitude range of the waves. These conditions are satisfied between 80 and 130 km. Additionally, wave detection is limited below 95 km due to low plasma density and high collisionality. It is further restricted by increased temperatures, which increase the instability threshold, above about 125 km. These conditions explain why echoes from Farley Buneman waves come from the E region in the auroral zone. Lastly, the dispersion relation predicts strong damping of waves with components parallel to the magnetic field. This results in waves that propagate nearly perpendicular to the magnetic field and irregularities that form nearly parallel to the magnetic field.

Linear kinetic theory

A similar dispersion relation can be derived using kinetic theory and expressed in terms of the ion and electron conductivities, σ_i and σ_e respectively, as derived by *Farley* [1963]. By using kinetic theory to describe the plasma dynamics, a more accurate dispersion relation can be obtained that accounts for thermal and collective effects, such as Landau damping. With this approach, the problem of finding the dispersion relation reduces to finding the electron and ion conductivities for the equation

$$\sigma_i + \sigma_e + i\omega\epsilon_o = 0 \tag{3.16}$$

Farley [1963] found the conductivities by writing the Boltzmann equation for a given distribution function, $f(\mathbf{r}, \mathbf{v}, t)$, for each particle species, linearizing, and assuming harmonic solutions of $f, \mathbf{B}$, and $\mathbf{E}$. This yields

$$\frac{\partial f}{\partial t} + \mathbf{v} \cdot \nabla f + \frac{q}{m}(\mathbf{E} + \mathbf{v} \times \mathbf{B}) \cdot \nabla_v f = \left[\frac{\partial f}{\partial t}\right]_c \tag{3.17}$$

where q, m, r, and v represent the charge, mass, position vector, and velocity vector of the particle, $\mathbf{B}$ is the geomagnetic field, and $\nabla_v f$ is the gradient of the distribution function in velocity space. Linearizing Equation (3.17) and assuming harmonic solutions of $f, \mathbf{B}$, and $\mathbf{E}$, the Boltzmann equation becomes

$$i(\omega - \mathbf{k} \cdot \mathbf{v}) f_1 + \frac{q}{m}\mathbf{E} \cdot \nabla_v f_0 + \frac{q}{m}(\mathbf{v} \times \mathbf{B}_0) \cdot \nabla_v f_1 = \left[\frac{\partial f}{\partial t}\right]_c \tag{3.18}$$

where the zero subscript refers to the constant, unperturbed value of the function and the one subscript refers to the small, first-order perturbation. This also assumes that f_0 is isotropic and therefore, $(\mathbf{v} \times \mathbf{B}) \cdot \nabla_v f_0$ is zero. *Farley* [1963] approximated the collision term on the right side of Equation (3.18) with

$$\left[\frac{\partial f}{\partial t}\right]_c = -\nu \left[f - \frac{N_1(\mathbf{r}, t)}{N_0} f_0\right] \tag{3.19}$$

where ν is the collision frequency and the number densities N_0 and N_1 are defined as

$$N_{0,1}(\mathbf{r}, t) = \int_v f_{0,1}(\mathbf{r}, \mathbf{v}, t) d^3 v \tag{3.20}$$

This collision term approximation allows for conservation of particles locally and does not cause longitudinal waves to be damped by collisions. However, it does not account for temperature fluctuations. Substituting Equation (3.19) into Equation (3.18) yields

$$i(\omega - i\nu - \mathbf{k} \cdot \mathbf{v}) f_1 + \frac{q}{m}\mathbf{E} \cdot \nabla_v f_0 + \frac{q}{m}(\mathbf{v} \times \mathbf{B}_0) \cdot \nabla_v f_1 = \frac{\nu f_0}{N_0} \int_{v'} f_1(\mathbf{r}, \mathbf{v}', t) d^3 v' \tag{3.21}$$

where ω was replaced with $\omega - i\nu$ to account for particle collisions. Equation (3.21) can then be solved for f_1, which can be used to find the components of the conductivity by calculating

$$J = q \int \mathbf{v} f_1 d^3 v = \sigma E \tag{3.22}$$

By assuming that f_0 is a Maxwellian distribution defined by

$$f_0(v) = (2\pi K_b T/m)^{-3/2} N_0 \exp\left(\frac{-mv^2}{2K_B T}\right) \tag{3.23}$$

we can solve Equation (3.21) using the analysis from *Dougherty* [1963]. The longitudinal conductivity term is equal to

$$\sigma_{zz} = \frac{ne^2\omega}{k^2 K_B T}\, y(\Theta, \xi, \phi, \alpha) \tag{3.24}$$

where

$$y = \frac{(\Theta - i\xi)G + i}{1 - \xi G} \tag{3.25}$$

The variable G is the normalized Gordeyev integral, $\Theta \equiv (\omega/k)/v_{ti}$ is the wave frequency normalized by the ion thermal velocity, $\xi \equiv (\nu_{in}/k)/v_{ti}$ is the ion-neutral collision frequency normalized by the ion thermal velocity, $\phi \equiv (\Omega/k)/v_{ti}$ is the gyrofrequency normalized by the ion thermal velocity, and α is the angle between the wave propagation direction and the magnetic field. Equation (3.24) can be used for either the electrons or ions. Making valid approximations for the electrojet, y can be simplified and the conductivity is equal to

$$\sigma = \frac{ne^2\omega}{k^2 K_B T_i}\left[\frac{xZ(x) + 1}{\xi Z(x) - i}\right] \tag{3.26}$$

where n is the electron number density, $x \equiv -\Theta + i\xi$, and Z is the plasma dispersion function calculated by *Fried and Conte* [1961] and defined as

$$Z(x) = 2ie^{-x^2} \int_{-\infty}^{ix} e^{t^2} dt \tag{3.27}$$

3.2.2 Improvements to linear theory

Lee et al. [1971] repeated the modified two-stream instability analysis for short wavelength, high frequency waves. The analysis found that an electron density threshold ($n_e \gtrsim 10^5$ cm^3) and a larger relative ion-electron drift velocity ($\sim$ three times the ion thermal speed) were required to excite the instability. Additionally, the calculations asserted that when a radar is not pointed parallel to the electron drift direction, it will observe different Doppler shifted frequencies, which cannot be predicted on the basis of a linear calculation. At UHF radar frequencies, the angular distribution of phase speeds versus flow angle becomes more isotropic.

Hysell et al. [2007] extended the dispersion relation derived by *Farley and Providakes* [1989] to incorporate electron thermal effects such as the election specific heat ratio, frictional heating, and collisional cooling into the electron conductivity. In the E region, the cooling effects play a significant role because the frequency of electron neutral collisions and the energy lost during each collision are both large. Electron heating has a smaller effect on the dispersion relation because the electron gyrofrequency is much larger than the collision frequency.

Michhue Vela [2010] later incorporated the RMS aspect width of the waves into the electron conductivity. With strong electron convection speeds, the aspect width of Farley Buneman waves can often exceed one degree, and the parallel components of the wave motion become more significant. As the aspect widths grow larger, wave heating increases, electron temperatures become elevated, and in turn, the ion-acoustic speed increases.

Both the thermal and aspect width considerations can be incorporated into the electron conductivity by using the equation describing the entropy of the electrons

$$n^{2/3}\frac{D}{Dt}\left(\frac{T_e}{n^{2/3}}\right) = \frac{2}{3}\nu_{en}\mu_e V_e^2 - \nu_{en}\delta_e(T_e - T_n) \tag{3.28}$$

where $\mu_e \equiv (m_e m_n)/(m_e + m_n)$ is the reduced mass of colliding electrons and neutrals, and δ_e is the average fraction of energy lost during a single electron neutral collision and is approximated for this analysis by $\delta_e = 5.0 \times 10^{-3}(185\text{K } K_B/T_e)^{3/2}$ [*Gurevich*, 1978]. The first term of the right side of Equation (3.28) represents frictional heating, while the second term represents collisional cooling rate due to electron neutral collisions.

Only the electron conductivity in Equation (3.16) needs to be modified to incorporate electron thermal effects and finite aspect widths into the dispersion relation. First, we combine Equations (3.7a) and (3.7b) to get the component of the velocity perpendicular to magnetic field, and use Equation (3.7c) as the parallel velocity component.

$$v_\perp = -\frac{e\nu_{en}\mathbf{E}_\perp}{m_e\Omega_e^2} - \frac{\nu_{en}\nabla_\perp(nT_e)}{m_e + \Omega_e^2 n} + \frac{\mathbf{E}\times\mathbf{B}}{B^2} + \frac{\nabla_\perp P_e \times \mathbf{B}}{enB^2} \tag{3.29a}$$

$$v_\parallel = -\frac{eE_\parallel}{m_e\nu_{en}} + \frac{\nabla_\parallel(nT_e)}{m_e\nu_{en}} \tag{3.29b}$$

Next, we linearize by assuming the electron density and temperature can be expressed as the sum of a constant and fluctuating term, and assume plane wave solutions such that, $\nabla \to ik$ and $\frac{d}{dt} \to i\omega$. The last two terms in the perpendicular velocity represent the diamagnetic gradient drift velocities, which can be ignored here.

$$v_\perp k_\perp = -\frac{e\nu_{en}\mathbf{E}_\perp k_\perp}{m_e\Omega_e^2} + \frac{ik_\perp^2\nu_{en}}{m_e\Omega_e^2}\left(T_1 + T\frac{n_1}{n}\right) \tag{3.30a}$$

$$v_\parallel k_\parallel = -\frac{eE_\parallel k_\parallel}{m_e\nu_{en}} + \frac{ik_\parallel^2}{m_e\nu_{en}}\left(T_1 + T\frac{n_1}{n}\right) \tag{3.30b}$$

Combining the perpendicular and parallel components using the equation, $\mathbf{v}\cdot\mathbf{k} = v_\perp k_\perp + v_\parallel k_\parallel$, we have:

$$\mathbf{v}\cdot\mathbf{k} = \left[-\frac{e\nu_{en}}{m_e\Omega_e^2} + \frac{\nu_{en}}{m_e\Omega_e^2}\left(T_1 + T\frac{n_1}{n}\right)\right]\left[\frac{k_\perp^2}{k^2} + \frac{k_\parallel^2}{k^2}\frac{\Omega_e^2}{\nu_{en}^2}\right] \tag{3.31}$$

Linearizing the momentum equation from Equation (3.28),

$$(i\tilde{\omega} + \nu_{en}\delta_e)T_1 - \frac{2}{3}i\tilde{\omega}T\frac{n_1}{n} = \frac{4}{3}\nu_{en}\mu_e V_d\mathbf{k}\cdot\mathbf{v} \tag{3.32}$$

where $\tilde{\omega} = \omega - i\mathbf{k}\cdot\mathbf{V}_d$ shifts the plasma motion into the ion frame of reference. The equation above can be expressed in terms of $T_1 + Tn_1/n$, which reduces to $(5/3)Tn_1/n$ for adiabatic electrons or to Tn_1/n for isothermal electrons. For electrons in between isothermal and adiabatic, Equation (3.32) is given by:

$$T_1 + T\frac{n_1}{n} = T\frac{n_1}{n}\underbrace{\frac{\frac{5}{3}i\tilde{\omega} + \nu_{en}\delta_e}{i\tilde{\omega} + \nu_{en}\delta_e}}_{R_1} + \frac{\frac{4}{3}\nu_{en}\mu_e\mathbf{V}_d}{i\tilde{\omega} + \nu_{en}\delta_e}\frac{\mathbf{k}\cdot\mathbf{v}}{k} \tag{3.33}$$

where R_1 is related to the heat electron ratio of specific heats and collisional cooling, which varies with the wave frequency. Combining Equations (3.31) and (3.33) and the linearized continuity equation ($n_1/n = k\cdot v/\tilde{\omega}$) yields:

$$\frac{\mathbf{v}\cdot\mathbf{k}}{k} = -\frac{e\nu_{en}}{m_e\Omega_e^2}\frac{E\tilde{\omega}}{\left(\frac{1}{\alpha} - R_2\frac{\nu_{en}^2}{\Omega_e^2}\right)\tilde{\omega} - D_e R_1 ik^2} \tag{3.34}$$

where

$$\alpha \equiv \frac{k_\perp^2}{k^2} + \frac{k_\parallel^2}{k^2}\frac{\Omega_e^2}{\nu_{en}^2}, \qquad D_e = \frac{T\nu_{en}}{m_e\Omega_e^2}, \qquad R_2 = \frac{\frac{4}{3}\mathbf{V}_d ik}{i\tilde{\omega} + \nu_{en}\delta_e} \tag{3.35}$$

The parameter, α, accounts for damping and dispersion for finite parallel wave numbers and R_2 is related to frictional heating and collisional cooling.

Finally, the electron conductivity can be resolved by substituting the velocity equation above into the current density given by:

$$J = -en\left(\frac{\mathbf{v}\cdot\mathbf{k}}{k} + \mathbf{V}_d\frac{n_1}{n}\right) = -\frac{en}{\tilde{\omega}}\left[\frac{\mathbf{v}\cdot\mathbf{k}}{k}(\omega - \mathbf{V}_d\cdot\mathbf{k}) + \mathbf{V}_d(\mathbf{v}\cdot\mathbf{k})\right] = \sigma_e E \quad (3.36)$$

$$\sigma_e = \frac{ne^2\omega\nu_{en}}{m_e\Omega_e^2\tilde{\omega}\left(\frac{1}{\alpha} - (\nu_{en}/\Omega_e)^2 R_2\right) - ik^2\nu_{en}K_B T_e R_1} \quad (3.37)$$

In the limit of $R_2 \to 0$ and $\alpha^{-1} \to 1$, Equation (3.37) becomes equal to the equation originally derived by *Farley and Providakes* [1989].

As the electron temperature rises in the E region, the ion-acoustic speed increases, ultimately resulting in a higher threshold for instability and a more limited growth rate. Additionally, the ion acoustic speed depends on the ratios of specific heat, which is related to the wave altitude, frequency, and wavelength [*Farley and Providakes*, 1989; *Kissack et al.*, 1997; *St.-Maurice et al.*, 2003; *Hysell et al.*, 2007; *Kagan et al.*, 2008]. This belongs to the domain of quasilinear theory.

3.2.3 Nonlinear theory

For small amplitude Farley Buneman waves, the linear theory describes the signal strength and aspect sensitivity of the coherent backscatter. However, many observed features of the waves cannot be fully explained with linear theory. The linear theory does not account for observations of waves with large flow angles, irregularities that are not strongly field aligned, and waves that are limited to the ion acoustic speed, even when drift velocity is much greater than the ion acoustic speed. Additionally, the spectral width of the echoes, observations of vertically

propagating Farley Buneman waves, and the k-spectrum of the waves are not explained by the linear theory.

The easiest way to extend the linear fluid theory into the nonlinear regime is to include the largest nonlinear term which is proportional to $\mathbf{B} \cdot \nabla n \times \nabla \phi$, where $\nabla \phi$ is the perturbed electric field. Nonlinear theories accounting for this term among others have found that kilometer-scale waves likely generated from large-scale gradients can modulate the meter-scale irregularities. Additionally, the nonlinear theories have been able to describe the observations of spectral width. See *Sahr and Fejer* [1996]; *Fejer and Kelley* [1980] for reviews.

Dougherty and Farley [1967] presented a qualitative nonlinear theory of equatorial irregularities and suggested that many of the weaker features of coherent echoes could be explained by wave-wave interactions. The nonlinear interaction between the waves generates new waves that cannot be directly excited. These theorized secondary irregularities can account for many of the unexplained features of the observed backscatter.

Greenwald [1974] applied this nonlinear equatorial electrojet theory to irregularities in the auroral zone E layer and to the diffuse radar aurora. The magnetic field geometry, presence of density gradients along the magnetic field lines, and large driving electric fields in the auroral zone prevents the application of the equatorial nonlinear theory. The analysis suggests that the secondary waves are more stable due to the increased background magnetic field and decreased ion-neutral collision frequency.

Several studies have shown that electron temperature enhancements in the E region can be attributed to Farley Buneman wave electric fields. *Robinson* [1986]

derived a nonlinear theory that calculated the Doppler shift of auroral echoes from the electron convection speed. *St.-Maurice and Laher* [1985] offer an improved theory that agreed closer with observations by taking into account the effects from parallel electric fields. *Milikh and Dimant* [2002] later showed that when the convection electric field is above threshold, the parallel electric field component is the major contributor to the elevated electron temperatures in the region.

3.3 Ionospheric models

This section describes the numerics and physics of the open source ionospheric model, SAMI2 [*Huba et al.*, 2000]. This model provides steady state values of the electron and ion temperature, ion composition, electron density, heating and cooling rates, chemistry, and collision frequencies which are required to model instability processes that involve the plasma dynamics of the ionosphere. At the end of this section, we summarize the findings of previous Farley Buneman wave models.

3.3.1 SAMI2 model

SAMI2 is a model of the ionosphere that calculates plasma state variables from 85 km to several thousand kilometers. The output of the model includes ion densities, ion composition, ion velocities parallel to the magnetic field, ion temperatures, and electron temperatures. Electron density is calculated by assuming quasineutrality, i.e., electron density is equal to the sum of the density of all seven ion species (H^+, He^+, N^+, O^+, N_2^+, NO^+, and O_2^+). The model accounts for chemistry,

temperature dependent collisions and recombination rates, electron and ion thermal effects, and parallel transport. Neutral state variables and electric field forcing are incorporated from empirical models. Time stepping is controlled through evaluation of the Courant condition. SAMI2 has been extensively validated with radar and satellite data in a number of geophysical contexts [*Huba et al.*, 2002, 2003].

The model uses a fluid description of the ionospheric plasma, which is derived from the moments of the Boltzmann equation [*Bellan*, 2006; *Schunk and Nagy*, 2009]

$$\frac{\partial f_\alpha}{\partial t} + \mathbf{v} \cdot \frac{\partial f_\alpha}{\partial \mathbf{r}} + \left(\mathbf{g} + \frac{q_\alpha}{m_\alpha}\mathbf{E} + \frac{q_\alpha}{m_\alpha}\mathbf{v} \times \mathbf{B} \right) \cdot \frac{\partial f_\alpha}{\partial \mathbf{v}} = \frac{\delta f_\alpha}{\delta t} \tag{3.38}$$

where $\mathbf{g}$ is the acceleration due to gravity, $\mathbf{E}$ is the electric field, $\mathbf{B}$ is the magnetic field, q_α and m_α are the species charge and mass. The variable f_α is a distribution function that represents the number of particles of species α in a unit hypervolume in position and velocity, $(\mathbf{r}, \mathbf{v})$, phase space. The term $\delta f_\alpha / \delta t$ is the rate of change of distribution function due to particle interactions, e.g., collisions, chemistry, charge exchange, and photoionization.

Taking the zeroth, first, and second moments of Equation (3.38) yields the continuity, momentum, and energy equations, respectively. These three equations can be expressed as

$$\frac{\partial N_\alpha}{\partial t} + \nabla \cdot (N_\alpha \mathbf{u}_\alpha) = \frac{\delta N_\alpha}{\delta t} \tag{3.39}$$

$$N_\alpha m_\alpha \left(\frac{\partial \mathbf{u}_\alpha}{\partial t} + \mathbf{u}_\alpha \cdot \nabla \mathbf{u}_\alpha \right) + \nabla \cdot \mathbf{P}_\alpha - N_\alpha q_\alpha (\mathbf{E} + \mathbf{u}_\alpha \times \mathbf{B}) - N_\alpha m_\alpha \mathbf{g} = \frac{\delta M_\alpha}{\delta t} \tag{3.40}$$

$$\frac{\partial}{\partial t}\left(\frac{3}{2}p_\alpha\right) + \mathbf{u}_\alpha \cdot \nabla \left(\frac{3}{2}p_\alpha\right) + \frac{5}{2}p_\alpha(\nabla \cdot \mathbf{u}_\alpha) + \nabla \cdot q_\alpha + \tau_\alpha : \nabla \mathbf{u}_\alpha = \frac{\delta E_\alpha}{\delta t} \tag{3.41}$$

where : is the double dot product. The remaining variables are defined in terms of

the distribution function, f_α, and are given by

$$\text{Density: } N_\alpha \equiv \int f_\alpha \, d^3v \tag{3.42}$$

$$\text{Mean velocity: } \mathbf{u}_\alpha \equiv \frac{1}{N_\alpha} \int \mathbf{v} f_\alpha \, d^3v \tag{3.43}$$

$$\text{Scalar pressure: } p_\alpha \equiv \frac{m_\alpha}{3} \int |\mathbf{v} - \mathbf{u}_\alpha|^2 f_\alpha \, d^3v \tag{3.44}$$

$$\text{Pressure tensor: } \mathbf{P}_\alpha \equiv m_\alpha \int (\mathbf{v} - \mathbf{u}_\alpha)(\mathbf{v} - \mathbf{u}_\alpha) f_\alpha \, d^3v \tag{3.45}$$

$$\text{Stress tensor: } \tau_\alpha \equiv \mathbf{P}_\alpha - p_\alpha \mathbf{I} \tag{3.46}$$

$$\text{Heat flow tensor: } \mathbf{q}_\alpha \equiv \frac{m_\alpha}{2} \int |\mathbf{v} - \mathbf{u}_\alpha|^2 (\mathbf{v} - \mathbf{u}_\alpha) f_\alpha \, d^3v \tag{3.47}$$

The variable $\mathbf{I}$ is the unit dyadic, which has unity values along the diagonal. The terms on the right side of Equations (3.39) to (3.41) are defined in terms of moments of the rate of change of the distribution function, f_α,

$$\frac{\delta N_\alpha}{\delta t} \equiv \int \frac{\delta f_\alpha}{\delta t} \, d^3v \tag{3.48}$$

$$\frac{M_\alpha}{\delta t} \equiv m_\alpha \int \mathbf{v} \frac{\delta f_\alpha}{\delta t} \, d^3v \tag{3.49}$$

$$\frac{E_\alpha}{\delta t} \equiv \frac{m_\alpha}{2} \int |\mathbf{v} - \mathbf{u}_\alpha|^2 \frac{\delta f_\alpha}{\delta t} \, d^3v \tag{3.50}$$

In order to solve Equations (3.39) to (3.41), the distribution function is assumed to be a drifting local Maxwellian given by

$$f_\alpha(\mathbf{r}, \mathbf{v}, t) = N_\alpha(\mathbf{r}, t) \left(\frac{m_\alpha}{2\pi K_B T_\alpha(\mathbf{r}, t)} \right)^{3/2} \exp \left[- \frac{m_\alpha |\mathbf{v} - \mathbf{u}_\alpha(\mathbf{r}, t)|^2}{2 K_B T_\alpha(\mathbf{r}, t)} \right] \tag{3.51}$$

where K_B is Boltzmann's constant, and T_α is the temperature of the species α. Additionally, the heat flow vector, $\mathbf{q}_\alpha$, and stress tensor, τ_α, are ignored. The scalar pressure is equal to $p_\alpha = N_\alpha K_B T_\alpha$. With these equations and approximations,

Equations (3.48) to (3.50) can be reduced to

$$\frac{\delta N_\alpha}{\delta t} = P_\alpha - \sum_\beta R_\beta N_\alpha \tag{3.52}$$

$$\frac{\delta M_\alpha}{\delta t} = -\sum_\beta N_\alpha m_\alpha \nu_{\alpha\beta}(\mathbf{u}_\alpha - \mathbf{u}_\beta) \tag{3.53}$$

$$\frac{\delta E_\alpha}{\delta t} = Q_\alpha - \sum_\beta N_\alpha \frac{m_\alpha}{m_\alpha + m_\beta}\left[3K_B\tilde{\nu}_{\alpha\beta}(T_\alpha - T_\beta) + m_\beta\nu_{\alpha\beta}|\mathbf{u}_\alpha - \mathbf{u}_\beta|^2\right] \tag{3.54}$$

where P_α is the production rate, R_β is the recombination rate of species β, $\nu_{\alpha\beta}$ is the momentum transfer collision frequency for collisions between α and β, $\tilde{\nu}_{\alpha\beta}$ is the energy transfer collision frequency, and Q_α is the external heating rate.

The continuity equation for the ions becomes

$$\frac{\partial N_i}{\partial t} + \nabla \cdot (N_i \mathbf{u}_i) = \mathcal{P}_i - \mathcal{L}_i N_i \tag{3.55}$$

In SAMI2, the ion production and loss terms, $\mathcal{P}_i$ and $\mathcal{L}_i$, account for photoionization, radiative recombination, and chemistry. To solve for the electron continuity, SAMI2 uses the quasineutrality condition, $N_e = \sum_j N_j$, where j is the number of ion species.

To simplify the electron momentum equation, electron inertia is neglected, i.e., $m_e/m_i \ll 1$ and $m_e/m_n \ll 1$, and the electron collisional terms are also neglected because the electron collision frequency is much less than electron gyrofrequency. The electron momentum equation becomes

$$0 = -\nabla p_e - N_e e(\mathbf{E} + \mathbf{u}_e \times \mathbf{B}) \tag{3.56}$$

The parallel electric field can be solved from this equation and is equal to

$$E_\parallel = -\frac{1}{N_e e}\nabla_\parallel p_e \tag{3.57}$$

The perpendicular component of the electric field is computed by SAMI2 using an empirical model developed by *Scherliess and Fejer* [1999].

The ion momentum equation is

$$N_j m_j \left(\frac{\partial \mathbf{u}_j}{\partial t} + \mathbf{u}_j \cdot \nabla \mathbf{u}_j \right) = -\nabla \cdot \mathbf{P}_j + N_j q_j (\mathbf{E} + \mathbf{u}_j \times \mathbf{B}) + N_j m_j \mathbf{g} - \nu_{jn}(\mathbf{u}_j - \mathbf{u}_n) - \sum_{k \neq j} \nu_{jk}(\mathbf{u}_j - \mathbf{u}_k) \quad (3.58)$$

where ν_{jn} is the ion-neutral collision frequency, and ν_{jk} is the ion-ion collision frequency.

In SAMI2, the energy equations for the ions and electrons are expressed as temperature equations. For the ions, the temperature equation is written as

$$\frac{\partial T_j}{\partial t} + \mathbf{u}_j \cdot \nabla T_j + \frac{2}{3} T_j \nabla \cdot \mathbf{u}_j + \frac{2}{3} \frac{1}{N_j K_B} \nabla \cdot \mathbf{Q_j} = Q_{jn} + Q_{jk} + Q_{je} \quad (3.59)$$

where $\mathbf{Q}_j$ represents the ion heat flux, and the terms Q_{jn}, Q_{jk}, and Q_{je} are heating due to ion-neutral collisions, ion-ion collisions, and ion-electron collisions, respectively. For the electrons, the temperature equation is

$$\frac{\partial T_e}{\partial t} - \frac{2}{3} \frac{\mathbf{B}^2}{e^2 N_e K_B B_0^2} \frac{\partial}{\partial s} \kappa_e \frac{\partial T_e}{\partial s} = Q_{en} + Q_{ej} + Q_{\text{phe}} \quad (3.60)$$

where the terms Q_{en}, Q_{ej}, and Q_{phe} represent heating due to electron-neutral collisions, electron-ion collisions, and photoelectron heating, respectively. The variable κ_e is the electron thermal conductivity, which is mainly field aligned. Effects of artificial heating or Farley Buneman wave heating can be incorporated into this equation simply by adding an additional heating rate to the left hand side of Equation (3.60). Derivations of these additional heating terms will be discussed in Section 7.3.1 and Section 5.1.

To make the plasma fluid equations easier to solve computationally, SAMI2 converts the continuity, momentum, and temperature equations into a dipole magnetic coordinate system in (q_d, p_d, ϕ_d) space, where q_d is the component along the magnetic field line, p_d is the component orthogonal to q_d, and ϕ_d is the magnetic longitude. A line of constant p_d and ϕ_d defines a magnetic field line. These coordinates are computed from a spherical coordinate system centered on the offset and tilted magnetic dipole of the Earth, defined by (r_e, θ_e, ϕ_e). These coordinate systems are related by the following equations

$$q_d = \frac{R_E^2}{r_e^2} \cos\theta_e \tag{3.61}$$

$$p_d = \frac{r_e}{R_E} \frac{1}{\sin^2\theta_e} \tag{3.62}$$

$$\phi_d = \phi_e \tag{3.63}$$

where R_e is the radius of the Earth, θ_e is latitude, and ϕ_e is longitude. See *Huba et al.* [2000] for a complete derivation of the coordinate transformations and for the fluid equations expressed in dipole coordinates.

This griding of the dipole coordinate system was modified to provide higher resolution data in the high latitude D and E region by adding 3000 points between 80 and 140 km for the Farley Buneman wave model and between 50 and 110 km altitude for the artificial heating model. Other modifications were made to SAMI2 to model artificial heating experiments and Farley Buneman wave heating. These specific changes will be discussed in their respective chapters.

During each time step, the model first determines the neutral atmospheric densities, temperatures, and winds with two empirical models. NRLMSISE-00 [*Picone et al.*, 2002] estimates the neutral density and temperature and HWM93 [*Hedin et al.*, 1991] estimates the neutral wind velocities. Next, it updates parameters due

to the effects of parallel transport. This is accomplished by solving the parallel components of the ion momentum, ion continuity, electron temperature equation, and ion temperature equations. The density, velocity, and temperatures are evaluated and a partial time step is taken. Then, perpendicular transport effects are calculated and $\mathbf{E} \times \mathbf{B}$ drifts are updated with an explicit scheme. Finally, the model evaluates the Courant condition to calculate an appropriate time step. To resolve the equations, the required time step is generally between 1 and 12 seconds. The densities, velocities, and temperatures computed after these steps are recorded to disk and these steps are repeated.

3.3.2 Farley Buneman wave modeling

Computational power required to simulate Farley Buneman waves has not been sufficient enough until the last several years. Early simulations were able to recover many properties of Farley Buneman waves, however. *Newman and Ott* [1981] used fluid theory to model the waves and a wavelength dependent viscosity term to model Landau damping. They were able recreate propagating waves, but they did not have the resources to model the waves propagating in saturation. *Machida and Goertz* [1988] created a particle-in-cell (PIC) code to incorporate the kinetic effects of Farley Buneman waves. Their model revealed that the waves propagate between the ion-acoustic speed and the electron drift speed and that the waves are coupled with long wavelength modes. *Janhunen* [1994] also developed a PIC code that simulated Farley Buneman waves and accounted for several dominant nonlinear terms and the results mostly agreed with *Machida and Goertz* [1988].

More recently, *Oppenheim et al.* [2008]; *Oppenheim and Dimant* [2013] simulated the propagation of Farley Buneman waves using a high resolution, three-

dimensional, PIC model. The simulations were able to produce primary waves that propagated at a phase speeds close to the ion acoustic speed and secondary waves that propagated perpendicular to the primary waves. The coupling between these waves could account for phase speeds close to the ion acoustic speed. They also found that waves preferred marginal stability, had consistent phase speeds over a wide range of magnetic aspect angles, and were capable of significantly increasing electron temperature.

Oppenheim et al. [2008]; *Oppenheim and Dimant* [2013] also confirmed that the moments of the Doppler spectra measured by a radar should vary approximately cosinusoidaly with the flow angle. Additionally, backscatter from the secondary Farley Buneman waves were shown to produce large Doppler widths for large flow angles.

CHAPTER 4

INSTRUMENTATION

This chapter gives an overview of coherent backscatter from field aligned density irregularities, along with the instruments and numerical models used to measure and understand it. We consider field aligned irregularities generated from either Farley Buneman waves or ionospheric modification experiments. Irregularities that form as a result of the Farley Buneman instability are observed with a 30 MHz coherent scatter radar in Homer, Alaska and an incoherent scatter radar, called the Poker Flat incoherent scatter radar (PFISR), outside of Fairbanks, Alaska. Artificial irregularities are generated with HAARP, a HF transmitter in Gakona, Alaska, and observed with the same 30 MHz radar in Homer.

4.1 Measuring field aligned irregularities with coherent scatter radar

Density irregularities in the auroral region are more intense and produce stronger backscatter than at mid- to low-latitudes because of faster convection speeds in the auroral electrojet. However, the magnetic geometry and variable nature of the region makes radar experiments more challenging than at the equator. Joule and wave heating increase plasma temperatures which causes greater ion acoustic speeds and changes the threshold of the Farley Buneman instability. Additionally, strong neutral winds can alter the Doppler shifts of irregularities measured by radars. Although gradient drift instabilities are less frequent at high latitudes, they can still arise under conditions where the conductivity gradient has a significant component perpendicular to the magnetic field. Low elevation angles and

long ranges are necessary for the radar beam to be perpendicular with the magnetic field at E region altitudes. This makes it difficult to avoid refraction and range/frequency aliasing of the radar signal. The combination of these factors warrants careful processing and analysis of coherent backscatter measurements.

Coherent scatter radars provide many useful diagnostics for detecting and quantifying field-aligned irregularities with high spatio-temporal resolution and accuracy. They are capable of scattering from field-aligned irregularities with kilometer scale resolution and at a cadence of several seconds to a minute. The simplest way to process the measured echo is to convert the time delay and frequency shifts of the backscatter into range and Doppler velocity measurements. Incoherent and coherent integration of the returned signals can be used to increase statistical confidence and the signal-to-noise ratio, respectively. Power spectra analysis yields information about the signal-to-noise ratio, the Doppler shift, and the Doppler width of the coherent backscatter.

Properties of auroral irregularities can be measured using either continuous wave (CW) or pulsed radar techniques. Transmitting with CW offers excellent spectral resolution but provides limited information about the range of the target. Pulsed radars can transmit different pulse schemes including a single pulse, double pulse, multiple pulse [*Farley*, 1972], or phase coded pulses [*Gray and Farley*, 1973]. Single pulse transmissions are used to measure the range and Doppler velocity of irregularities. Double pulse experiments transmit two pulses, separated by a time τ. Complex return samples from the two pulses are multiplied together and averaged over a period of time. As a result, the uncorrelated clutter in the signal is removed and only the correlated signal remains. The values of τ are varied to form a complete auto correlation function (ACF), the Fourier transform of the power

spectra. Multiple pulse measurements follow the same principles as a double pulse experiment, but transmit more than two pulses with non-redundant spacing, so that the clutter is never correlated. Phase coded pulsing involves transmitting pulses modulated with a random or preselected code at a interval chosen to avoid both frequency and range aliasing. If a proper code is chosen, this technique can increase the signal-to-noise ratio without degrading the range resolution.

For pulsed radars, the time between pulses, or the interpulse period (IPP), must be carefully selected to limit range and frequency aliasing. An IPP that avoids aliasing must meet the following criteria

$$2|f_D|_{max} \leq \frac{1}{IPP} \leq \frac{c}{2R_{max}} \tag{4.1}$$

where $|f_D|_{max}$ is the largest expected Doppler shift, $f_D = u/\lambda$, u is the approach speed of the target, λ is the radar wavelength, c is the speed of light, and R_{max} is the largest expected range of the target. If the inequality on the left (right) is not met, frequency (range) aliasing will occur. When range and frequency aliasing are avoided, the target is underspread. If aliasing will necessarily be present, the target is overspread. Another important parameter to set is the pulse width, τ, which must be carefully chosen to balance the range resolution and system bandwidth. Shorter pulses decrease range resolution and increase the bandwidth, while longer pulses have the opposite effect. For an underspread target, a single pulse experiment will resolve the measurements without aliasing. For overspread targets, double or multi-pulse experiments are required to find the true range and Doppler shift of the target.

At higher F region altitudes or for systems with high signal bandwidths, measuring overspread targets can be an issue. F region radars like SuperDARN, which transmit at lower (8-20 MHz) frequencies, have to deal with overspread targets

because of potentially greater ranges to the target [*Greenwald et al.*, 1995]. To circumvent this, SuperDARN performs multiple-pulse experiments, which have a range resolution corresponding to the time between pulse groups and a frequency resolution corresponding to the spacing between the pulses. The additional, uncorrelated clutter can be removed to some degree with careful selection of the pulse repetition pattern and by averaging the signals over time. Averaging for longer periods improves the statistical confidence but degrades the time resolution. STARE also needs to use multiple pulse transmissions to avoid aliasing, but for different reasons. STARE is a high latitude VHF E region radar, and at these frequencies, the expected Doppler velocities can be as large as 2000 m/s [*Greenwald and Ecklund*, 1975]. This results in large values of $|f_D|_{max}$ and the targets for the STARE radar are underspread, and the left-hand side of the inequality in Equation (4.1) cannot be satisfied.

Typically, for single pulse experiments, the backscatter measurements are coherently processed by computing the Fast Fourier Transform (FFT) of the measured samples to form a Doppler spectrum at each time sample in each range bin. The nth moment of the spectra, $S(\omega)$, at is defined as

$$M_n = \frac{1}{S_0} \int_{-\infty}^{\infty} \omega^n S(\omega)\, d\omega \tag{4.2}$$

where the signal power is equal to

$$S_0 = \int_{-\infty}^{\infty} S(\omega)\, d\omega \tag{4.3}$$

The first three moments of the spectra contain information about the signal-to-noise ratio, the Doppler shift, and spectral width respectively. To improve statistical confidence, these Doppler spectra can then be incoherently integrated.

Figure 4.1: Geographic locations of instruments in Alaska

4.2 Instrumentation

The geographic locations of the instrumentation discussed in this section are mapped in Figure 4.1. The beam pointing of the 30 MHz coherent scatter radar in Homer can be configured to point in the E region above HAARP or above PFISR. The specific parameters of the Homer radar are discussed in the next subsection. This is followed by an overview of the HAARP and PFISR instruments.

4.2.1 Homer, Alaska VHF Coherent Scatter Radar

A 30 MHz pulsed Doppler radar located on Diamond Ridge (59.68 N, 151.63 W) in Homer, Alaska was deployed to observe field-aligned irregularities in the E region of the ionosphere. At 30 MHz, the radio aurora is an underspread target. For heating experiments the maximum span of possible ranges, R_{max}, for the Homer radar is approximately 200 km, and the maximum expected velocity is approximately 100 m/s. For auroral experiments, there is a larger span of ranges of $\sim$ 300 km and larger expected velocities of 675 m/s. Both of these experiments satisfy the inequality from Equation (4.1). This makes it possible to avoid range and frequency ambiguity by carefully selecting an IPP. Additionally, at 30 MHz, the signal undergoes enough refraction to align the radar wave vector perpendicular with the magnetic field without significantly shifting the altitude of reflection.

The radar is composed of 16 horizontally-polarized 3-element Yagi antennas, a 12 kW solid state transmitter, an arbitrary waveform generator, and a 6 channel digital receiver. A diagram of the radar antennas is shown in Figure 4.2. The 16 antennas are arranged into 6 groups; two groups are used for transmitting and all six groups are used to receive. The baselines between each group of antennas are labeled in the figure, as well. Pairs of antennas are separated by 5/8 of a wavelength and the largest baseline is 15 wavelengths. The half-power full beamwidth of the antenna transmission patter is approximately 10°. The transmitted pulses are modulated with a 13-bit Barker code. The radar line of sight is perpendicular to the magnetic field at 110 km altitude above HAARP and 112 km altitude above PFISR. The color contours in Figure 4.3 represent the locus of perpendicularity above the PFISR. A typical 11 beam configuration of the PFISR is plotted with black points. The figure shows that the backscatter within the common volumes

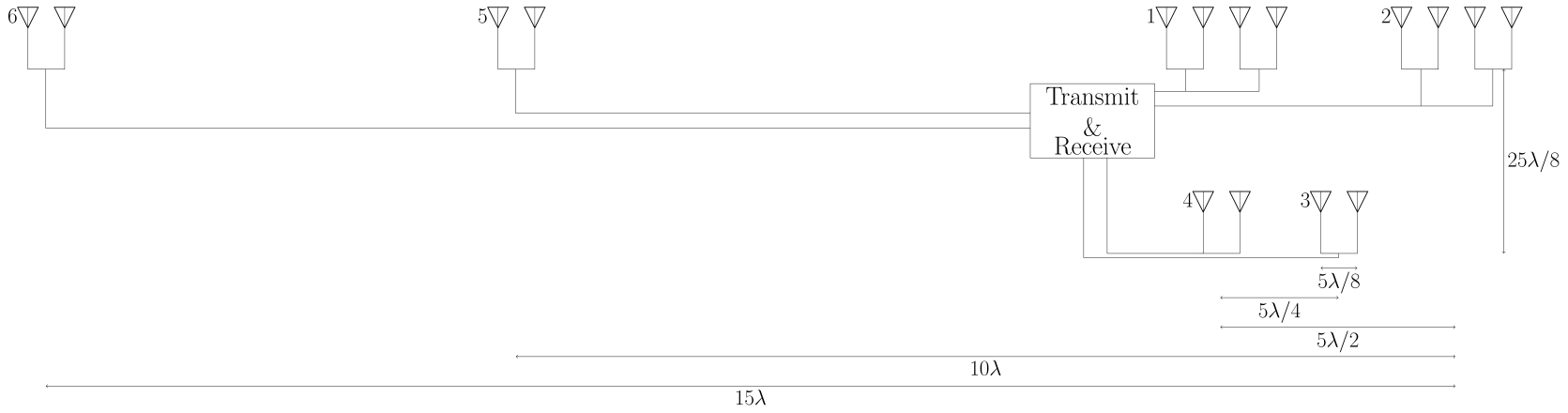

Figure 4.2: Six antenna groups of the Homer radar. Groups 1 and 2 are used to transmit and all the groups are used to receive.

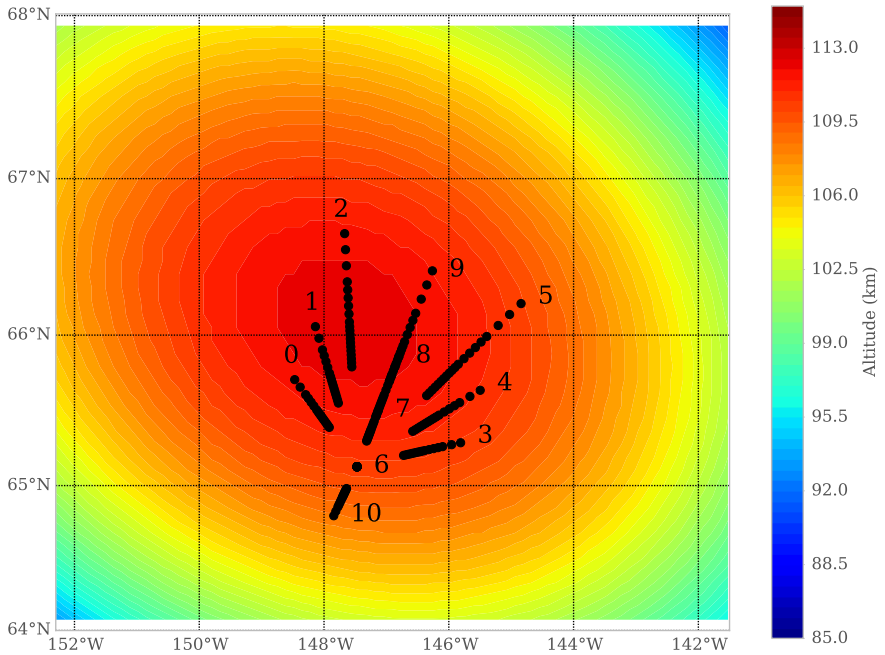

Figure 4.3: Altitude of the locus of perpendicularity (color-scale) for the Homer radar above the Poker Flat Research Range. The range bins of an eleven beam PFISR configuration are mapped to the geographic plane and are plotted in black points. Each beam labeled with its respective beam number.

of both radars is between 106 and 114 km altitude.

An overview of the radar parameters selected to measure coherent backscatter from E region irregularities is shown in Table 4.1. Different pulse configurations are chosen for active HF heating experiments and for natural auroral observations.

When the scattered signal returns to the antennas, it is sent through a series of limiters, amplifiers, then incoherently integrates the signal for $\sim$5 seconds and computes the spectra and cross-spectra for each receiver. The Doppler spectra can be calculated by taking the FFT of a uniformly-spaced set of complex samples and then multiplying the result by its complex conjugate. This spectra can be decomposed to signal amplitude, Doppler shifts, and spectral width.

parameter	artificial	auroral
frequency	29.795 MHz	
peak power	12 kW	
coding	13 bit Barker	
no. channels	6	
time resolution	5 s	
bandwidth	100 kHz	
no. ranges	120	
pulse length	19.5 km	23.4 km
duty cycle	5.27%	4.68%
IPP	370 km	500 km
r_0	40 km	140 km
δr	1.5 km	1.8 km

Table 4.1: Parameters of the coherent scatter radar in Homer for active and auroral experiments

The antennas are configured to form 15 non-redundant baselines, which allow the radar to function as an aperture synthesis radar. *Hysell and Chau* [2006] discuss the processing involved with inverting the visibility measurements into the scattered power density as a function of bearing, called the brightness. The visibility, $V(k\mathbf{d})$, is related to the brightness, $B(\sigma)$, through the integral transform,

$$V(k\mathbf{d}) = \int_{4\pi} A_N(\sigma) B(\sigma) e^{jk\mathbf{d}\cdot\sigma} d\Omega \tag{4.4}$$

where σ is a unit vector in the direction of a place in the sky being mapped, A_N is the normalized two-way antenna effective area, and $\mathbf{d}$ is the baseline vector between the receivers, and k is the radar wavenumber. In one dimension, the visibility measurements are represented as

$$V(kd_j) = \frac{\langle v_1 v_2^* \rangle}{\sqrt{\langle |v_1|^2 \rangle - N_1}\sqrt{\langle |v_2|^2 \rangle - N_2}} \tag{4.5}$$

which is the normalized complex spatial cross-correlation for the baseline d_j. The

variables $v_{1,2}$ and $N_{1,2}$ correspond to the quadrature voltage samples and noise estimates, respectively. The calculations carried out for the Homer radar imaging algorithm extend this equation into two dimensions.

Equation (4.4) could be inverted to solve for the brightness distribution through an inverse integral transform, if there were infinite antennas evenly spaced at $k\mathbf{d}$ intervals. This simple inversion cannot be applied to the Homer radar because the antennas are arranged in a non-uniform, finite array. Instead, an inverse method developed by *Wilczek and Drapatz* [1985] is used to estimate the most likely brightness distribution. The technique uses Bayesian regularization to maximize the Shannon entropy of the system. The Bayesian regularization model searches for the solutions that maximize the posterior probability distribution

$$P(f|g) = \frac{P(f)P(g|f)}{P(g)} \tag{4.6}$$

where f and g represent the model and visibility data, respectively, $P(g|f)$ is the probability that the visibility measurements arose from a given brightness distribution, $P(g)$ is a normalization constant related to the visibilities, and $P(f)$ is a model for a priori information about the image. The methods chosen by *Hysell and Chau* [2006] associate $P(f)$ with the Shannon entropy of the brightness distribution. The Shannon entropy of the system is given by

$$S = -f(\theta_i)\ln(f(\theta_i)/F) \tag{4.7}$$

where $f(\theta_i)$ is the real valued brightness in the i^{th} discretized zenith angle bin, and F is the total image brightness. This favors higher entropy brightness distributions and constrains the solution set to contain only positive brightnesses.

The solution that maximizes Equation (4.6) while satisfying the constraints of Equation (4.7) yields $2M + 1$ coupled, non-linear equations, where M is the

number of independent baselines. These equations are then solved with a hybrid method for numerical nonlinear equations [*Powell*, 1970].

The hybrid method yields estimates of the brightness for each range and azimuth bin in the radars field of view for each Doppler frequency bin. The summation of the brightness at each frequency is then used to calculate the spectra for each range and azimuth bin. The result is three dimensional, but only backscatter from near the locus of perpendicularity is considered. A scattering altitude of 110 km is assumed and each bin is mapped to the geographic plane in latitude and longitude. The zeroth, first, and second moments of the spectra from each bin relate to the signal to noise ratio, the Doppler shift, and the spectral width, respectively.

Figure 4.4 shows an example of a two dimensional Homer radar image from December 8, 2013 at 05:10 UT. The abscissa and ordinate of the plot correspond to the latitude and longitude of the field of view of the radar. The color value, hue, and saturation of each pixel represent the signal-to-noise ratio, Doppler velocity, and spectral width, respectively. The dashed line contours show the altitude locus of perpendicularity of the Homer radar. The symbols "P" and "F" represent the locations of the PFISR and Fairbanks, Alaska. In this example, Doppler shifts between $\pm$675 m/s and spectral widths as large as 675 m/s can be measured.

4.2.2 HAARP

The HAARP (High Frequency Active Auroral Research Program) facility near Gakona, Alaska (62.39 N,145.15 W) consists of 180 crossed dipole antennas in a 12$\times$15 array, designed to transmit up to 3.6 MW of power into the ionosphere

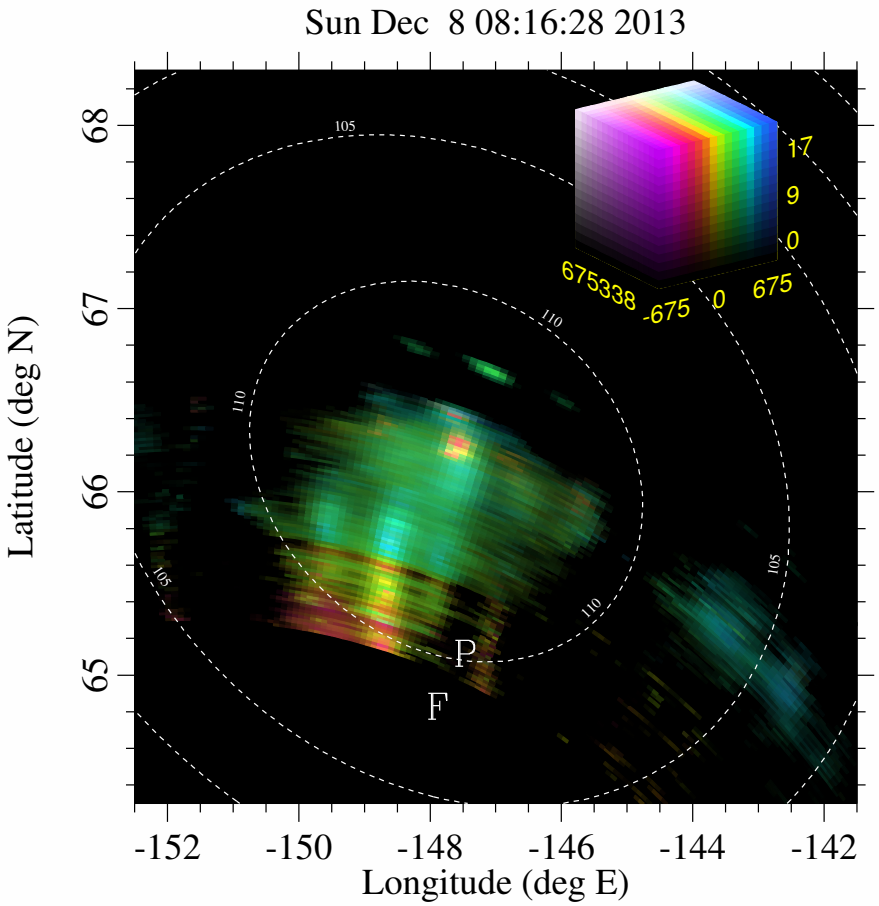

Figure 4.4: Homer radar coherent scatter imaging. Color values, hue, and saturation of each pixel represents signal-to-noise ratio, Doppler velocity, and spectral width of the spectra, respectively. PFISR and Fairbanks are labeled with "P" and "F" symbols.

at HF frequencies. Each antenna is connected to two 10 kW transmitters that can be controlled independently. The power, frequency, and polarization of the transmitted RF waves are configurable. Additionally, the phasing of the antenna array can be changed electronically, which allows the elevation and azimuth of the beam to be controlled.

The HAARP facility transmits electromagnetic (pump) waves that interact with the ionospheric plasma. These modification experiments can change the

plasma temperature and density, generate field aligned irregularities, cause absorption of radio waves, artificially enhance airglow emissions, and/or enhance ion and plasma lines in incoherent radar spectra [*Robinson*, 1989]. These effects have been studied by ground-based coherent and incoherent scatter radar, ionosondes, optical instruments, ionosondes, and in situ with satellites and sounding rockets.

Artificial field aligned irregularities generated by HAARP were first observed in the F region by *Hughes et al.* [2003] and later shown to be observable at multiple frequencies at HF and VHF [*Senior et al.*, 2004]. Due to lower densities in the E region, artificial irregularities are more difficult to generate and observe than in the F region. HAARP is capable of transmitting at frequencies as low as 2.75 MHz, which makes it possible to generate AFAIs in low E region densities at frequencies near the second electron gyroharmonic frequency. The geometry of the geomagnetic field lines at high latitude makes it possible to observe E region artificial irregularities with a coherent scatter radar pointed at a low elevation angle.

The high power electromagnetic waves transmitted by HAARP can excite many different plasma processes and waves. These include electron plasma waves, ion acoustic waves, upper hybrid waves, lower hybrid waves, electron and ion Bernstein waves, electron whistler waves, and ion cyclotron waves. The instability processes include the parametric decay instability, the thermal parametric instability, and the resonance instability. The physics of the instability mechanisms that generates these irregularities will be discussed in Chapter 7.

4.2.3 PFISR

Incoherent scatter radars measure the Doppler power spectrum of a signal that scatters from the random thermal motion of the electrons in the ionospheric plasma. This idea was first proposed by [*Gordon*, 1958] and the first ionospheric incoherent scatter radar experiment was performed by *Bowles* [1958]. For several years after this discovery, many theories were derived to explain the observed Doppler spectra [*Dougherty and Farley*, 1960; *Farley et al.*, 1961; *Dougherty and Farley*, 1963; *Farley*, 1963; *Swartz and Farley*, 1979; *Fejer*, 1960a, b, 1961; *Salpeter*, 1960, 1961; *Hagfors*, 1961; *Rosenbluth and Rostoker*, 1962; *Farley*, 1966]. In the original paper by *Dougherty and Farley* [1960], the scattering theory was based on the generalized Nyquist Theorem to derive a single admittance for the entire plasma to explain the scattering of radio waves from the thermal fluctuations of electron density in a collisionless plasma. The other theories used different approaches to arrive at equivalent results.

To measure the Doppler spectra, an incoherent scatter radar can transmit in many different modes, which can be modified depending on the types of phenomena being observed. Typical modes include double pulse, multi-pulse, which were discussed in Section 4.1. Other experiments use alternating codes [*Lehtinen and Hggstrm*, 1987], long pulse, or coded long pulse [*Sulzer*, 1986] techniques, which are used to take full advantage of the radar's duty cycle, while providing multiple measurements of the lags of the autocorrelation function.

The raw quantities that an incoherent scatter radar measures are the voltages of the reflected signal. These signals typically pass through several stages of filters, digitizers, and multipliers to mix the measured signal to baseband and produce two outputs called the in-phase and quadrature signals. These two channels are

digitally processed to produce the signal power and a complex autocorrelation function at individual range bins.

The autocorrelation functions contain information about the electron density, electron temperature, ion temperature, line of sight plasma velocity, and if the masses of the ion species are not close to one another, information about the ion composition can be evaluated. The autocorrelation functions at each range are inverted individually to estimate these plasma parameters in each bin. Alternatively, the plasma parameters at all ranges can be fit using the autocorrelation functions from every range. This method is called a "full profile analysis", which was first suggested by *Lehtinen* [1986], implemented by *Holt et al.* [1992], and further refined by *Lehtinen et al.* [1996]; *Hysell et al.* [2008b]. The full profile analysis can also incorporate regularization to enforce smoother profile fits.

The incoherent scatter radar data presented in this thesis comes from the Poker Flat Incoherent Scatter Radar (PFISR). It was built as the first radar in the Advanced Modular Incoherent Scatter Radar (AMISR) network, which consists of modular, transportable radars that measure the plasma parameters of the ionosphere. The PFISR is located outside of Fairbanks, Alaska (65.13 N, 147.47 W), consists of a phased array of 4,096 crossed dipole antennas and can transmit up to 2 MW of power. The antenna is tilted toward the geomagnetic north pole and is positioned near the center of the auroral oval. The radar can control the phasing of the transmitted signal from each antenna, which allows the radar beam to be steered electronically and redirected nearly instantaneously. If the electron density is large enough, the PFISR can measure backscatter from as low as 60 km altitude and as high as a few thousand kilometers. The measurements are fit to determine profiles of electron density, electron and ion temperature, ion velocity, and ion-

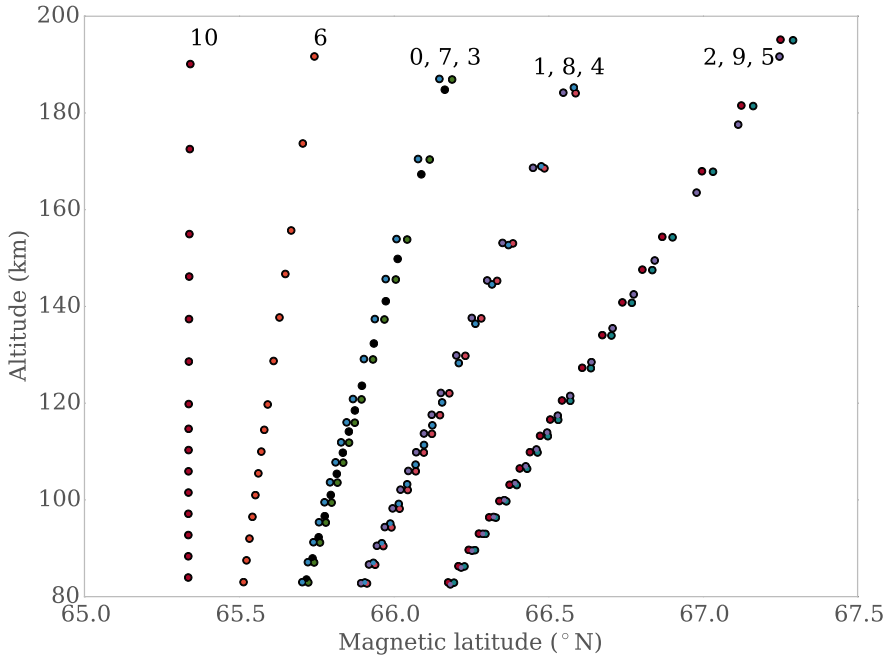

Figure 4.5: PFISR eleven beam pattern as a function of magnetic latitude and altitude. Labels at top of the plot correspond to the beam number.

neutral collision frequencies. The time resolution of the data typically ranges from 1 to 5 minutes.

For the ISR data presented in later chapters, the PFISR transmitted alternating codes with an eleven beam configuration shown in Figure 4.3. Each range and altitude bin within beam is plotted as a black point. The elevation of the beams in this configuration range from 48° to 90° and the altitude ranges from 83 to 195 km. Figure 4.5 shows the same eleven beam pattern plotted as a function of magnetic latitude and altitude. For drift measurements, the PFISR transmitted long pulse codes. The beam configuration and data processing scheme allows for plasma measurements over broad spatial scales and temporal scales of approximately 3 minutes.

CHAPTER 5

FARLEY BUNEMAN WAVE MODEL AND OBSERVATIONS

In this chapter, we outline a model of Farley Buneman waves and heating, which combines the local heuristic theory proposed in *Milikh and Dimant* [2002] and the global SAMI2 ionospheric model developed by *Huba et al.* [2000] as described in *Hysell et al.* [2013]. The model simulates Farley Buneman waves in the auroral E region for electron convection speeds between 400 and 1000 m/s. The wavelengths of the simulated waves were chosen to be 1 and 5 m, which bracket the dominant scale lengths of the plasma density irregularities. In the second section, the relationship between modeled Farley Buneman waves characteristics and both coherent and incoherent scatter radar measurements is evaluated. First, the modeled results of electron density, electron temperature, and ion temperature profiles are compared with incoherent scatter radar measurements of the E region ionosphere when Farley Buneman waves are present. The model is used with the incoherent scatter radar measurements to estimate the convection velocity. Then, modeled estimates for Farley Buneman wave phase velocity are compared with the Doppler spectra moments measured by the Homer VHF coherent scatter radar.

5.1 Farley Buneman wave and heating model

To understand the relationship of Farley Buneman wave heuristics and its global significance, we developed a model of Farley Buneman waves and heating combining the heuristics of *Milikh and Dimant* [2002]; *Dimant and Milikh* [2003] and *Milikh and Dimant* [2003] and the global ionospheric model SAMI2 [*Huba et al.*, 2000]. This section describes 1) the heuristic model of *Milikh and Dimant* [2002], 2) the general equations required to model Farley Buneman waves and heating, and

3) the specific modifications made to the SAMI2 model to combine the heuristics into the global model.

5.1.1 Heuristic model

Section 3.2.1 reviews the linear fluid theory for Farley Buneman waves. However, the linear theory does not account for many of the features observed experimentally. To reconcile some of the differences, many researchers developed quasilinear, weak turbulence, and non-linear theories. Additionally, heuristic models were formed as more data was collected from a variety of instruments, including coherent and incoherent scatter radars, sounding rockets, and satellites.

The model developed here and described in *Hysell et al.* [2013] combines the global SAMI2 model of the ionosphere with local Farley Buneman wave heating heuristics developed by *Milikh and Dimant* [2002]; *Dimant and Milikh* [2003] and *Milikh and Dimant* [2003]. The heuristic model of Farley Buneman waves assumes that

1. the RMS transverse electric field for Farley Buneman waves, $\sqrt{\langle \delta E_\perp^2 \rangle}$, is equal to the background convection electric field in the ion frame of reference, less the threshold for instability.
2. the magnetic aspect angle of Farley Buneman waves, $\theta = k_\parallel / k_\perp$, is as large as is necessary to maintain the condition for marginal growth, i.e., a linear growth rate near zero.

The basis for the first assumption is that when the waves are fully saturated, the major nonlinear term of the dispersion relation is of the same order of the largest

linear term. This nonlinear term is proportional to the temporal and spatial average values of the turbulent electric field, $\langle \delta E^2 \rangle$, and the linear term is proportional to the convection electric field in the ion frame of reference, E_C. Additionally, since the waves are strongly field aligned, the RMS values of the turbulent electric field is approximately equal to the RMS transverse electric field. This leads to the estimate that

$$\langle \delta E^2 \rangle \approx \langle \delta E_\perp^2 \rangle \simeq E_C^2 \tag{5.1}$$

For the second assumption, *Milikh and Dimant* [2002] argue that the linear growth rate of Farley Buneman waves is significant for a wide range of aspect widths which is supported by the findings of *Ossakow et al.* [1975]. The linearly unstable range can be determined from the fluid expression of the linear Farley Buneman growth rate [*Farley*, 1985]

$$1 + \psi \leq \frac{E_C}{E_{thr}}(1 + \psi_\perp) \tag{5.2}$$

where

$$\psi = \psi_\perp \left(1 + \frac{\theta^2 \Omega_e^2}{\nu_{en}^2}\right), \qquad \psi_\perp = \frac{\nu_{en}\nu_{in}}{\Omega_e \Omega_i} \tag{5.3}$$

represent the anisotropy of the propagating wave, $E_{thr} = C_s(1 + \psi_\perp)B_0$ is the threshold electric field at a given altitude, ν_{en} and ν_{in} are electron-neutral and ion-neutral collision frequencies, respectively, and Ω_e and Ω_i are the electron and ion gyrofrequencies, respectively. From Equation (5.2), the maximum value of ψ to maintain marginal stability is given by

$$\psi_{max} \equiv \frac{E_C}{E_{thr}}(1 + \psi_\perp) - 1 \tag{5.4}$$

With this, the maximum aspect angle to maintain marginal stability can be cal-

culated from Equations (5.3) and (5.4)

$$\theta^2_{max} = \frac{\nu^2_{en}}{\Omega^2_e}\left(\frac{E_C}{E_{thr}} - 1\right)\left(\psi_\perp^{-1} + 1\right) \tag{5.5}$$

This shows that as the convection increases, larger magnetic aspect angles are necessary to keep the growth rate close to zero. This results in increased wave heating, electron temperatures, and ion acoustic speeds. According to the Farley Buneman dispersion relation, the increased ion acoustic speed will increase the instability threshold and change the wave phase speed.

5.1.2 Modelling Farley Buneman waves and heating

The goal of the model is to compute profiles of electron density, electron and ion temperature, electron and ion heating rates, wave-phase velocity, and aspect width in the presence of Farley Buneman waves for convection speeds in intervals ranging from 400 to 1000 m/s. The SAMI2 model provides the framework for numerically simulating the state parameters of an undisturbed ionosphere. To incorporate the effects of Farley Buneman waves into the model, we require equations for the Farley Buneman dispersion relation, electron and ion heating rates due to wave heating, and the density perturbations caused by the waves.

Farley Buneman dispersion relation derived in Section 3.2.2 which includes considerations for the magnetic aspect width, $\langle k^2_\parallel / k^2 \rangle$, and the effects of frictional heating and cooling by inelastic collisions [*Farley and Providakes*, 1989; *Hysell*

et al., 2007; *Michhue Vela*, 2010] was used in the model and is given by

$$\sigma_i + \sigma_e + i\omega\epsilon_o = 0 \tag{5.6a}$$

$$\sigma_i = \frac{ne^2\omega}{k^2 K_B T_i}\left[\frac{xZ(x)+1}{\xi Z(x) - i}\right] \tag{5.6b}$$

$$\sigma_e = \frac{ne^2\omega\nu_{en}}{m_e\Omega_e^2\tilde{\omega}\left(\alpha^{-1} - (\nu_{en}/\Omega_e)^2 R_2\right) - ik^2\nu_{en}K_B T_e R_1} \tag{5.6c}$$

where $\sigma_{i,e}$ are the ion and electron conductivities, respectively, $\omega = \omega_r + i\gamma$ is the complex wave frequency, $x \equiv -\Theta + i\psi$, $\Theta \equiv (\omega/k)v_{ti}$ is the wave frequency normalized to the ion thermal velocity, $\psi \equiv (\nu_{in}/k)/v_{ti}$ is the ion neutral collision frequency normalized to the ion thermal velocity, and

$$\alpha \equiv \frac{k_\perp^2}{k^2} + \frac{k_\parallel^2}{k^2}\frac{\Omega_e^2}{\nu_{en}^2}, \qquad R_1 = \frac{\frac{5}{3}i\tilde{\omega} + \nu_{en}\delta_e}{i\tilde{\omega} + \nu_{en}\delta_e}, \qquad R_2 = \frac{\frac{4}{3}\mathbf{V}_d ik}{i\tilde{\omega} + \nu_{en}\delta_e} \tag{5.7}$$

The variable, δ_e, represents the fractional electron energy loss rate during electron neutral collisions. This is modeled as a function of the electron temperature given by $\delta_e = 4.8 \times 10^{-3}(185/T_e)^{3/2}$ [*Gurevich*, 1978]. The α parameter accounts for dispersion and damping associated with finite parallel wave numbers. *Oppenheim and Dimant* [2013] found that simulated Farley Buneman waves exhibit wave coupling between different parallel wave numbers and propagate within packets at phase speeds near the ion acoustic velocity while maintaining phase lock between the packets. This allows the $k_\parallel^2/k^2$ term to be replaced with the average of the entire packet, $\langle k_\parallel^2/k^2\rangle$. Additionally, the $k_\perp^2/k^2$ can be set to unity because of the field aligned nature of the waves, i.e., $k_\parallel \ll k_\perp \approx k$. With these considerations, $\alpha = 1 + \langle k_\parallel^2/k^2\rangle(\Omega_e^2/\nu_{en}^2)$. Other variables not defined here can be found in Section 3.2.1.

The unknown ionospheric parameters in Equation (5.6) are computed by the model, and the equations can be solved for the wave frequency and aspect width for

a given electron convection speed and Farley Buneman wavelength. The condition for marginal stability is enforced by setting $\gamma = 0$ and only considering the real components of the complex wave frequency. The values for wave frequency and aspect width are solved for iteratively using Powell's hybrid method, which finds the minimum of the function without calculating derivatives [*Powell*, 1964]. This process is repeated for every altitude point in the range between 95 and 130 km and for the 13 convection speeds between 400 and 1000 m/s.

The next step in the model is to calculate electron and ion heating rate profiles. At E region altitudes, the heating from electric fields parallel to the magnetic field and collisional cooling are more significant than the effects of frictional heating. The collisional cooling and frictional heating effects are accounted for with the R_1 and R_2 terms in the Farley Buneman dispersion relation. In the region where Farley Buneman waves propagate, it has been shown that the perpendicular component of the electric field, $\delta E_\perp$, does not account for the high electron temperatures measured experimentally and that the major source of anomalous electron heating is due to small components of the turbulent electric field parallel to the magnetic field, $\delta E_\parallel$ [*St.-Maurice and Laher*, 1985; *Providakes et al.*, 1988; *St.-Maurice*, 1990; *Milikh et al.*, 2001]. To account for this, the model calculates the electron heating rate using the parallel component of the wave number, $\langle k_\parallel^2/k^2 \rangle$ multiplied by an estimate of the transverse, wave-driven electric field. The electron heating rate is modeled with the heuristic equation,

$$Q_e = \begin{cases} (v'_{de} - v_o)^2 B^2 \langle k_\parallel^2/k^2 \rangle \sigma_{oe} & v'_{de} > v_o \\ 0 & v'_{de} \leq v_o \end{cases} \tag{5.8}$$

where σ_{oe} is the electron direct conductivity, v'_{de} is the electron $\mathbf{E} \times \mathbf{B}$ drift speed in the frame of reference of partially $\mathbf{E} \times \mathbf{B}$ drifting ions, and v_o is the threshold

velocity required for instability. When the electron drift speed is not above the threshold, v_o, the electron heating rate is zero. The term $(v'_{de} - v_o)B$ represents an estimate of the transverse, wave-driven electric field given by *Dimant and Milikh* [2003]. When this term is multiplied by $\langle k_\parallel^2/k^2 \rangle$, it produces an estimate for the wave-driven parallel electric field.

The formula for the ion heating rate was estimated to be equal to the Joule heating rate which is proportional to the convection electric field, i.e.,

$$Q_i = E_{cn}^2 \sigma_{pi} \tag{5.9}$$

where σ_{pi} is the ion Pedersen conductivity and E_{cn} is the convection electric field in the neutral frame of reference. The model assumes that E_{cn} is equal to a fraction of the electric field associated with the convection speed. This assumption does not fully account for the effects of varying neutral wind speeds, which are difficult to measure or model. The wind speed and direction mainly affects the Joule heating rates, which in turn, affects the overall heating rates [*Thayer*, 1998]. The effects of Joule heating on the model were examined by performing different model runs with magnitudes of E_{cn} varying from 0.1 to 1.0 times the electric field associated with the convection speed in intervals of 0.1. It was found that the ion heating with various convection electric fields occurred in regions outside of Farley Buneman wave propagation.

To estimate the electron density perturbations caused by the Farley Buneman waves, we start with the linearized electron continuity equation in the frame of reference of the ions and assuming quasineutrality

$$i\omega\delta n - ikn_0(v'_{de} - v_o) = 0 \tag{5.10}$$

This can be rewritten as

$$\delta n = \frac{(v'_{de} - v_o)n_0}{\omega/k} \tag{5.11}$$

From the estimate of the transverse wave electric field, the associated amplitude of the density can be substituted into Equation (5.11) to obtain

$$|\delta n| = (v'_{de} - v_o)B\frac{|\sigma_e|/e}{\omega/k} \tag{5.12}$$

assuming quasi-neutrality. This information can be used to estimate how radio waves will scatter from Farley Buneman wave for a span of altitudes. Since the density irregularities are not constant in altitude, coherent backscatter will be more intense in regions where the density perturbations are larger. However, this equation does not take the radar geometry or refraction into account. The scattering geometry of the Homer VHF radar and the finite width of the Farley Buneman wave scattering volume will be considered when comparing the model results with the coherent scatter radar measurements.

5.1.3 Modifications to SAMI2

As discussed in Section 3.3.1, the SAMI2 global model calculates ionospheric state parameters and includes the effects of heating, cooling, chemistry, temperature-dependent collisions, and parallel transport. This model was modified to combine Farley Buneman wave heuristics and equations described in the previous two subsections. A high resolution grid for the D and E regions was used with 3000 additional points between 80 and 140 km altitude.

Another modification was to calculate the heating generated by the Farley Buneman waves. These rates were calculated from Equations (5.8) and (5.9). The

aspect width of the waves is required to solve Equation (5.8) and it is calculated at each altitude point for each convection speed assuming that it is as large as necessary to maintain marginal stability. Additionally, complete thermodynamics for all ion species was added to the model to better estimate the auroral heating.

Profiles of wave-phase velocity and aspect width of Farley Buneman waves propagating through the ionosphere simulated by SAMI2 were calculated by solving the Farley Buneman dispersion relation, i.e., Equation (5.6), at every altitude. Profiles from a single flux tube were used for this analysis.

5.1.4 Model results

The profiles in Figure 5.1 show the results from the Farley Buneman wave model for 5 m wavelength waves. The left most plot shows groups of profiles corresponding to electron density and temperature, and ion temperature. The profiles within each group coincide with 13 discrete electron convection speeds ranging from 400 to 1000 m/s. The lowest (highest) convection speed corresponds with the leftmost (rightmost) profile in the group. As the convection speed increases, the instability reaches threshold, and wave heating causes the electron temperature to increase in the region between 105 and 120 km, reaching a maximum at approximately 112 km. The ion temperatures increase due to Joule heating, which largely depends on the neutral wind speed. The model assumes that the neutral wind speed is equal to 0.4 times the ion drift speed. This ratio was chosen because it produced temperature and density profiles that were most consistent with profiles measured by the PFISR (evidence of this will be discussed in the next section). Additionally, runs of the model showed that the effects of Joule heating occurred above 120 km altitude, outside the region of Farley Buneman wave heating, so we assume that

Joule heating will not significantly affect the model results. The elevated electron densities between 100 and 120 km result from increased electron temperatures which decreases the recombination rate.

The center panel of Figure 5.1 plots the RMS aspect width and phase velocity profiles of the Farley Buneman waves for the same range of convection speeds. The maximum phase velocity reaches 800 m/s while the maximum aspect width is about 1 degree. These profiles represent characteristics associated with marginal wave growth.

The right panel of Figure 5.1 shows groups of electron and ion heating rates, along with an averaging kernel, K, which is proportional to the electron density perturbation, $|\delta n|^2$, from Equation (5.12). The heating rates are largest at altitudes slightly below the maximum ion and electron temperatures. This difference arises because the electron and ion cooling rates (not shown on the plot) are higher at lower altitudes, and the combined heating and cooling effects result in maximal electron temperatures at approximately 112 km.

To maintain the condition of marginal stability, either diffusive damping or damping due to aspect width broadening is required. At altitudes above 110 km, diffusive damping is more prevalent due to higher ion-acoustic speeds. Below 110 km, the component of the wave vector parallel to the magnetic field needs to increase to compensate for the lack of diffusive damping. This results in greater RMS aspect widths at lower altitudes.

The bottom panel of Figure 5.1 plots the kernel-averaged values of the phase velocity and aspect width profiles. These points are proportional to measurements that a coherent scatter radar might observe. The kernel-averaged values account

for reflection from a finite span of altitudes, but do not account for propagation or flow angle effects. The vertical lines represent the range of possible ion-acoustic velocities, which are defined as

$$C_s \equiv \sqrt{\frac{\gamma_e K_B T_e + \gamma_i K_B T_i}{m_i}} \tag{5.13}$$

where $\gamma_{i,e}$ is the ratio of specific heat, $T_{i,e}$ is the ion or electron temperature, and K_B is Boltzmann's constant. The bottom point of each line corresponds to isothermal electrons ($\gamma_e = 1$), while the top of the line corresponds to adiabatic electrons with 1 degree of freedom ($\gamma_e = 3$). Ions were assumed to be adiabatic with 3 degrees of freedom ($\gamma_i = 5/3$) following *Farley and Providakes* [1989] for the purposes of plotting these lines. The kernel-averaged phase velocities calculated in this model run are generally in the middle of the adiabatic and isothermal limits. It is important to consider this range of ion acoustic speeds because this quantity cannot be directly measured and depends on numerous factors such as the electron and ion temperature, wave and Joule heating, heat transport, and the degree of adiabaticness of the ions and electrons.

Figure 5.2 plots the model output for 1 m wavelength Farley Buneman waves. Compared with the results from Figure 5.1, the electron temperature and density is less enhanced and the maximum enhancement occurs at a lower altitude. At shorter wavelengths, Landau damping becomes more prevalent, and the waves satisfy the condition of marginal stability at lower temperatures, slower phase velocities, and smaller aspect angles. The averaging kernel, K, shows that the density perturbations occur at lower altitudes and reach a maximum around 105 km. This indicates that the higher frequency components of Farley Buneman waves tend to be more focused at lower altitudes.

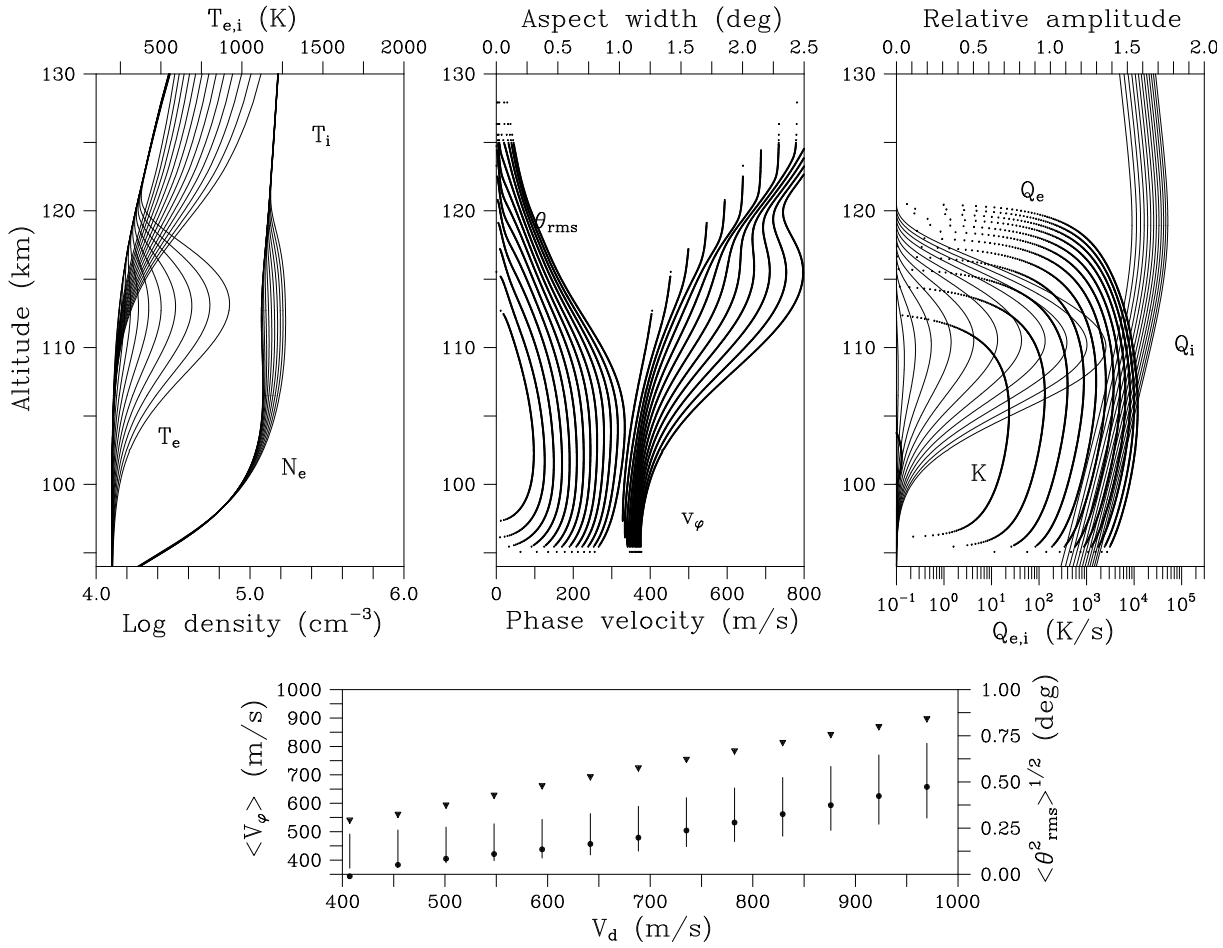

Figure 5.1: Results from FB wave model for 5 m wavelength. Left: Electron density, electron temperature, and ion temperature profiles. Middle: Phase velocity, and aspect width profiles. Right: Electron and ion heating rate, and amplitude averaging kernel profiles. Bottom: Kernel-averaged phase velocity (circles), kernel-averaged aspect width (triangles), and ion-acoustic speed ranges (lines). Bottom of the line corresponds to isothermal electrons, while the top of the line corresponds to adiabatic electrons with 1 degree of freedom.

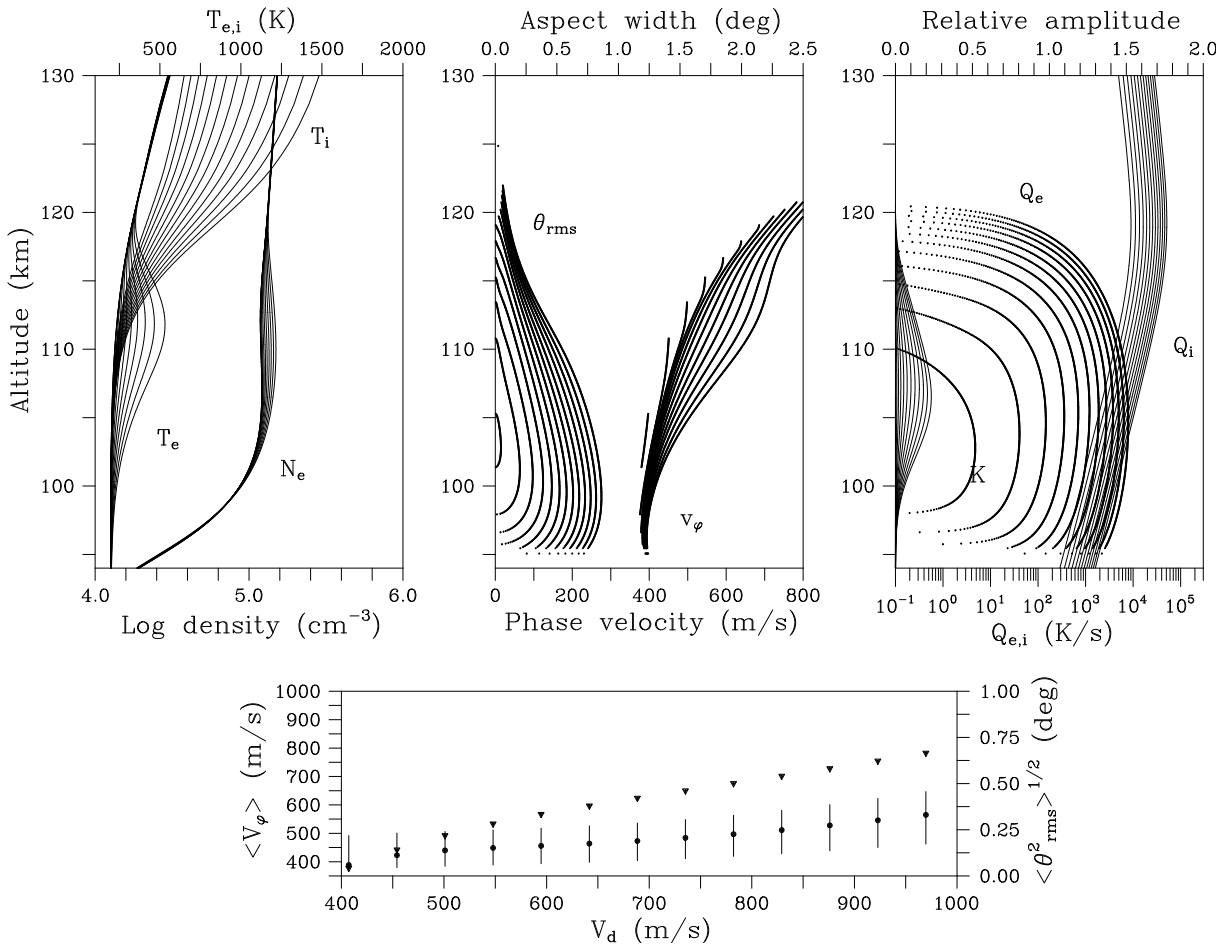

Figure 5.2: Results from the Farley Buneman wave model for 1 m wavelength waves.

The kernel-averaged values phase velocities in the bottom panel of Figure 5.2 represent the Doppler shift that a coherent scatter radar would measure if the line of sight was directly aligned with the direction of wave propagation and if the geometry of the radar was not taken into account.

The plots presented for 1 m and 5 m waves only represent two wavelength of the broadband Farley Buneman wave spectrum. The 1 and 5 m wavelength cases cover two of the dominant scale lengths of the plasma waves, which makes it easy to compare with single frequency radars. However, in order to understand the entire

picture, a model that includes the broadband spectrum of the Farley Buneman waves would be required.

The model has been validated against numerous radar and sounding rocket observations and theoretical studies [*Hysell et al.*, 2013]. The span of ranges where the Farley Buneman waves propagate in the model agree with the sounding rocket experiments of *Ogawa et al.* [1976]; *Pfaff et al.* [1984], among others. The Chatanika, Alaska incoherent scatter radar recorded temperatures between 600 and 1400 K at 112 km altitude [*Schlegel and St.-Maurice*, 1981]. These observations are consistent with the profiles produced by the model. *St.-Maurice et al.* [1981b] developed a quasi-linear theory to explain anomalous electron heating near 110 km altitude and verified the results with the same electron temperature measurements from the Chatanika radar. They produced similar electron temperature and density profiles shapes as the model. Other incoherent scatter radars including EISCAT (European Incoherent Scatter Facility) [*Igarashi and Schlegel*, 1987] and the Str. Strømfjord ISR [*Stauning and Olesen*, 1989] have independently observed comparable electron temperature and density profiles. The next section compares measurements from the PFISR to further validate the modeled profiles.

Nielsen and Schlegel [1985] studied the relationship between the measured Doppler velocities and the electron convection velocity. The empirical formulas they developed agree with the kernel-averaged phase velocities from in the 1 m wavelength Farley Buneman model (Figure 5.2 and *Hysell et al.* [2013] Figure 2). This empirical relationship can be used to invert coherent scatter radar spectra into electron convection velocities.

The convection velocities used in the model are supported by measurements from the SuperDARN network of coherent scatter radars. *Bristow* [2008] calculated

statistics over a 6 year period of the auroral convection pattern during periods when the interplanetary magnetic field was aligned southward. The average velocities were on the order of about 250 to 300 m/s with standard deviations as large as 400 m/s. These statistics reveal the highly variable nature of the ionospheric flow velocities. The Farley Buneman wave model accounts for convection speeds between 400 and 1000 m/s which covers approximately 1.75 standard deviations from the mean values determined by *Bristow* [2008].

The range of values of the ion acoustic speed, shown in the bottom panel of Figures 5.1 and 5.2, highlights the importance of Equation (5.13). The ion acoustic speed depends on the electron and ion temperatures, and the electron and ion ratio of specific heat, which all vary in altitude. This analysis shows that estimating the ion acoustic speed as a constant value for all altitudes and ionospheric conditions will result in inaccurate ion acoustic speeds and misinterpretations of the Farley Buneman threshold phase velocity.

Finally, the model reveals that although Farley Buneman waves primarily generate meter scale irregularities, they affect ionospheric state parameters over tens of kilometers in altitude. The variations of these values with altitude are important to consider when analyzing radar observations, which effectively average the variations in altitude due to the finite span of the region satisfying the condition for field aligned backscatter. In addition to the averaging kernel plotted in the right-most panel of Figures 5.1 and 5.2, kernels accounting for the geometry of the radar and the effects of refraction should be considered when comparing modeled phase velocities with measured Doppler velocities from coherent scatter radars.

5.2 Comparison of model with radar observations

In this section, we attempt to validate the Farley Buneman model with measurements from the Poker Flat incoherent scatter radar and the Homer VHF coherent scatter radar. The PFISR profiles of electron density, electron temperature, and ion temperature are compared with the modeled profiles. The errors between the data/model profiles are used as an assessment of the Farley Buneman wave model. The data/model comparison can also be used to estimate profiles of Farley Buneman wave phase speed and RMS aspect width during periods when the PFISR observes Farley Buneman wave heating. Additionally, Doppler velocity measurements from the Homer radar can be compared with kernel-averaged phase velocities from the model. The modeled estimates are shown to be within a reasonable range of the measured Doppler velocities, despite the fact that the averaging kernel does not account for the specific geometry of the radar. Finally, moments of the Homer radar Doppler spectra are inverted to estimate flow angle and kernel-averaged phase velocities. These values are compared with model estimated phase velocities and with PFISR measurements of the flow angle.

5.2.1 Incoherent scatter radar observations

As the convection speed increases within the model, electron temperature enhancements form around 112 km altitude for both 1 m and 5 m scale Farley Buneman waves. These enhancements can be verified with incoherent scatter measurements from the PFISR. A model of ionospheric plasma parameters is used to invert the measured ACF data from the PFISR to obtain electron density, electron and ion temperature, ion velocity, and ion-neutral collision frequency profiles. See Sec-

tion 4.2.3 for an overview of the capabilities and system parameters of the PFISR.

The Farley Buneman wave model introduced in the previous section was run 13 times for different electron convection speeds between 400 and 1000 m/s. Each run corresponds to a single profile in Figures 5.1 and 5.2. To determine the model run that best matched the PFISR data for a three minute interval, the model profile was selected that minimized the discrepancy between the model and measured PFISR electron temperature profile in a least squares sense. The differences between the electron temperature profiles were evaluated from 108 and 116 km altitude. This region of enhanced electron temperature is the best indication of Farly Buneman wave heating from the PFISR data, and therefore, we use this parameter as a metric of model-data agreement. Once an electron temperature profile is selected for a given time period, the corresponding modeled profiles at the same convection speed are generated. These profiles include electron density, ion temperature, phase velocity, aspect width, and averaging kernel.

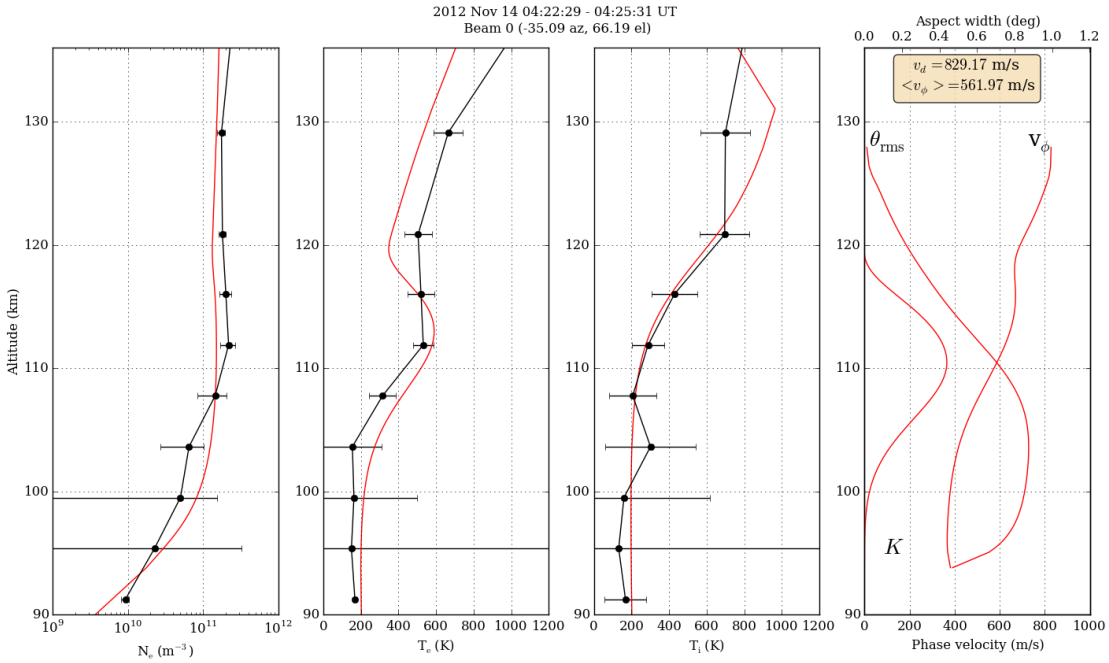

Figure 5.3: Measured PFISR density and temperature profiles (black) together with modeled profiles (red). The model assumes a convection speed of 829 m/s. Altitude averaging kernel, predicted phase velocity, and aspect width profiles are shown on the right and labeled as K, v_ϕ, and θ_{rms} respectively.

Figures 5.3 to 5.11 compare model runs for 5 m scale Farley Buneman waves with profile measurements from the PFISR, which was configured in an 11 beam pattern. The plots show periods of measured elevated electron temperatures between 105 and 120 km altitude on November 14, 2012 from 0030 to 0500 UT. The black points in Figure 4.3 represent the geographic locations of the center of each range bin within each of the 11 beams. Alternating coded pulses were used and measurements were integrated at 3 minute intervals. The plots show PFISR measurements of electron density, electron temperature, and ion temperature with their estimated errors. The red curves represent individual profiles from the Farley Buneman wave model that best matched the PFISR measurements. The box in the top right corner of each figure indicates the convection speed and kernel-averaged

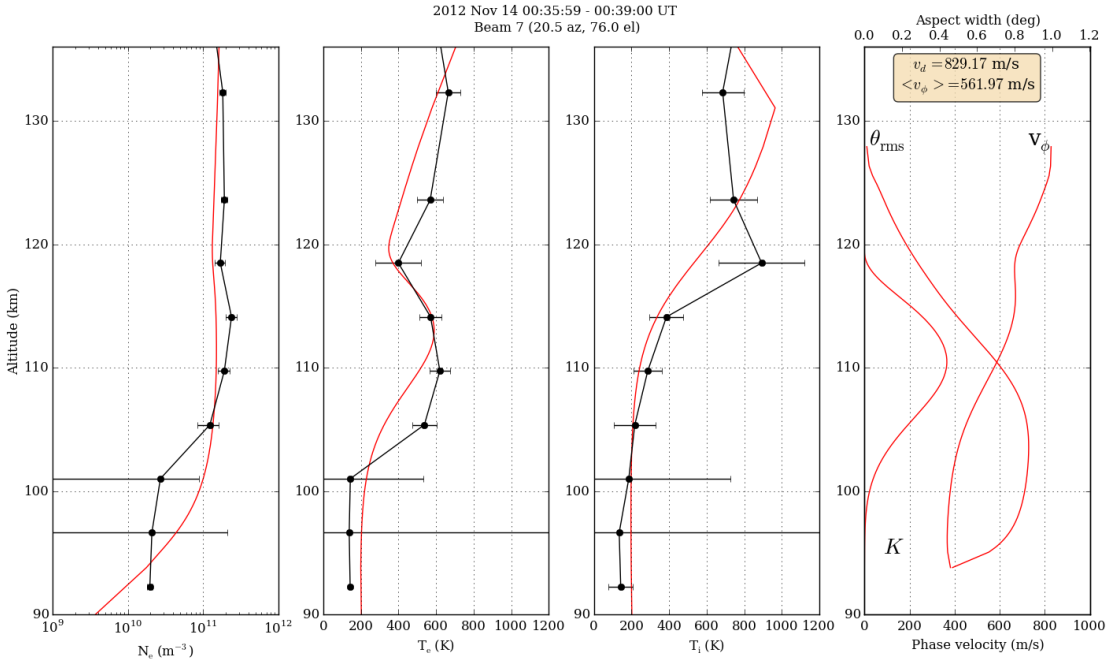

Figure 5.4: PFISR profiles compared with Farley Buneman wave model

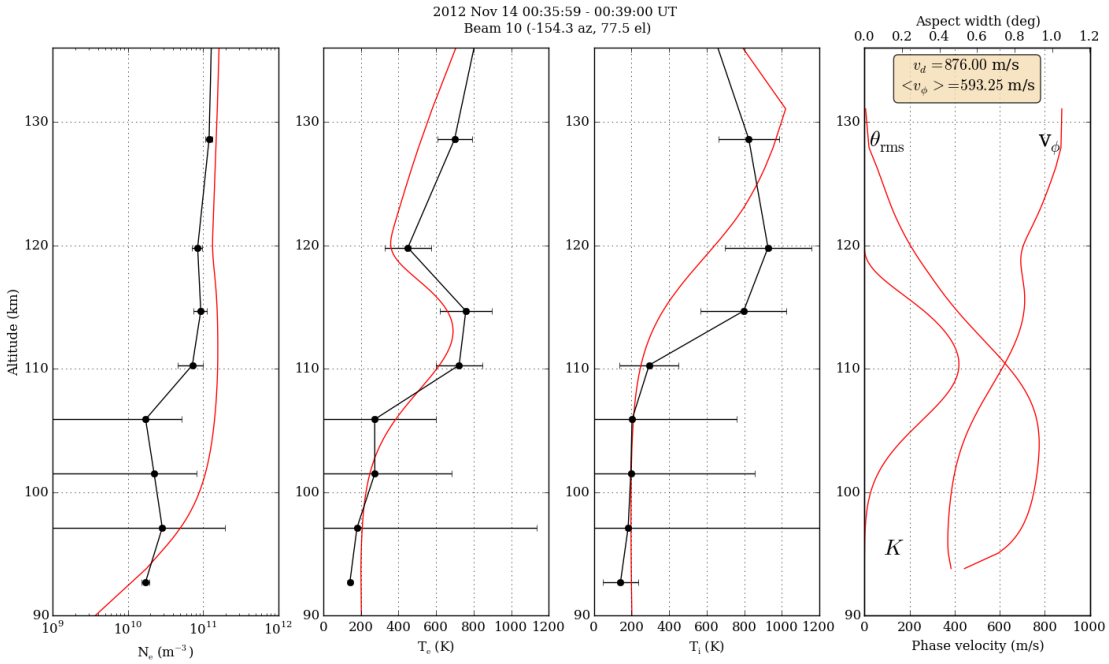

Figure 5.5: PFISR profiles compared with Farley Buneman wave model

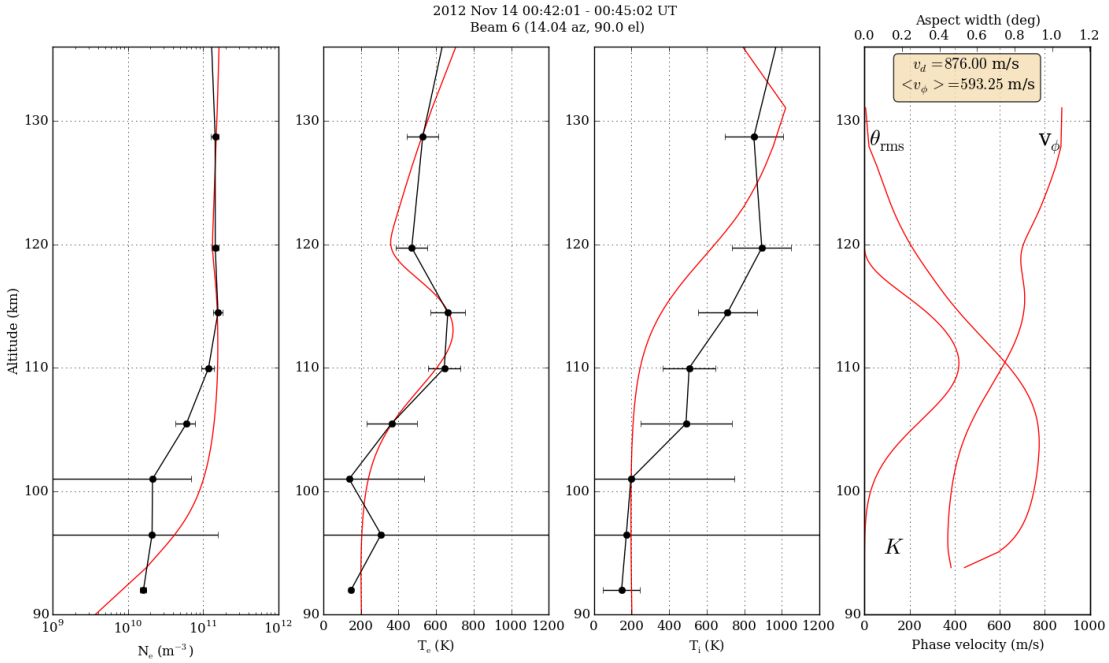

Figure 5.6: PFISR profiles compared with Farley Buneman wave model

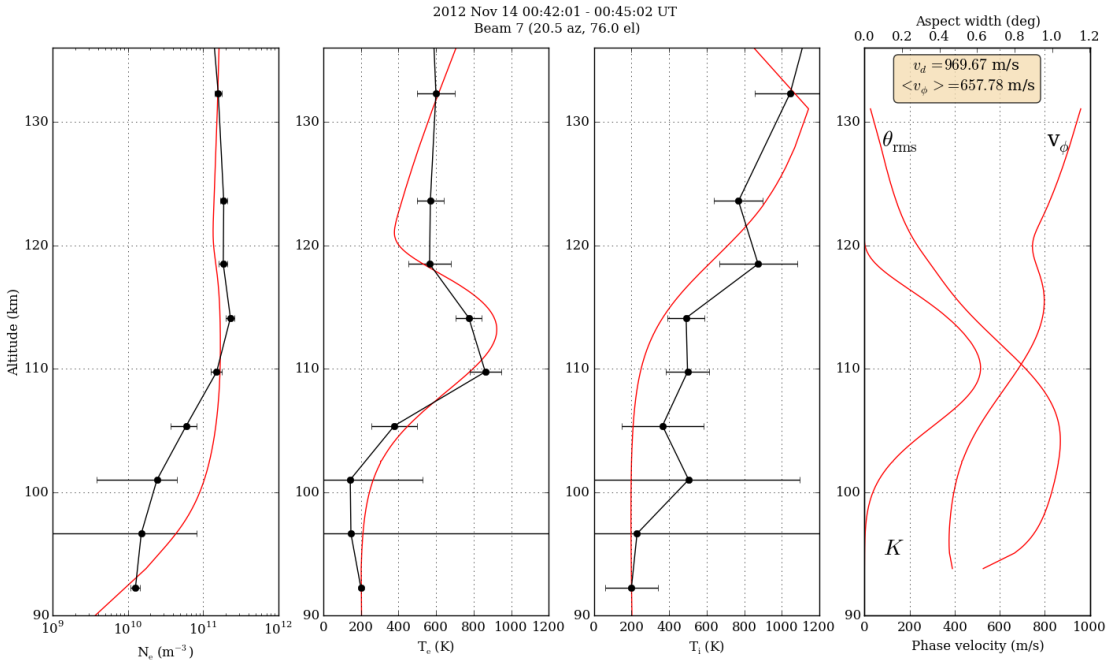

Figure 5.7: PFISR profiles compared with Farley Buneman wave model

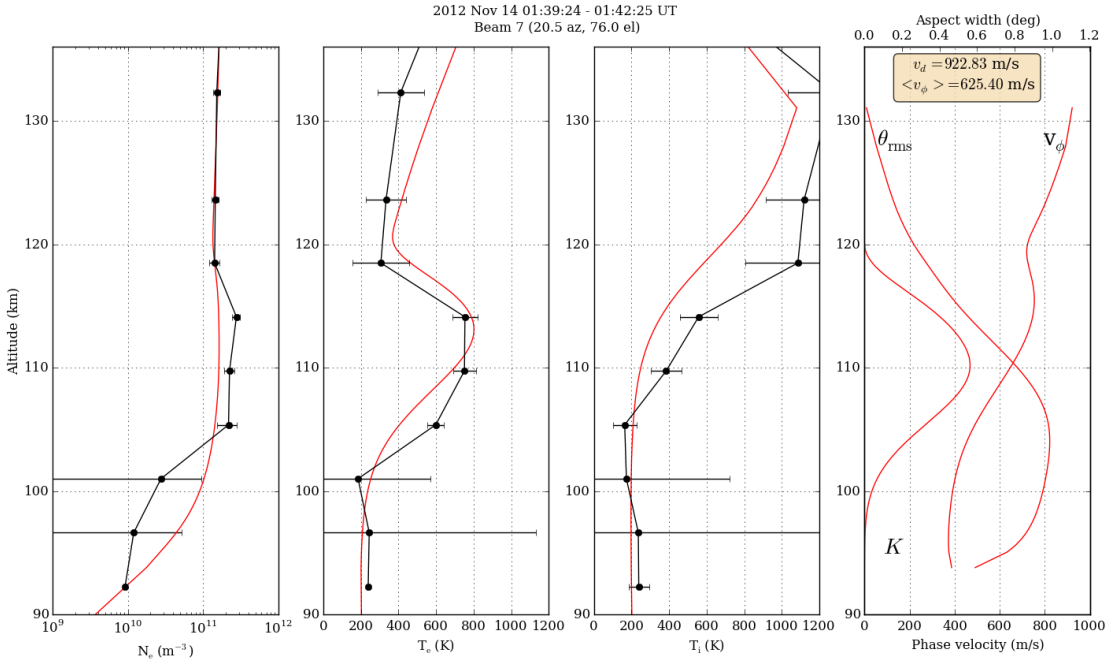

Figure 5.8: PFISR profiles compared with Farley Buneman wave model

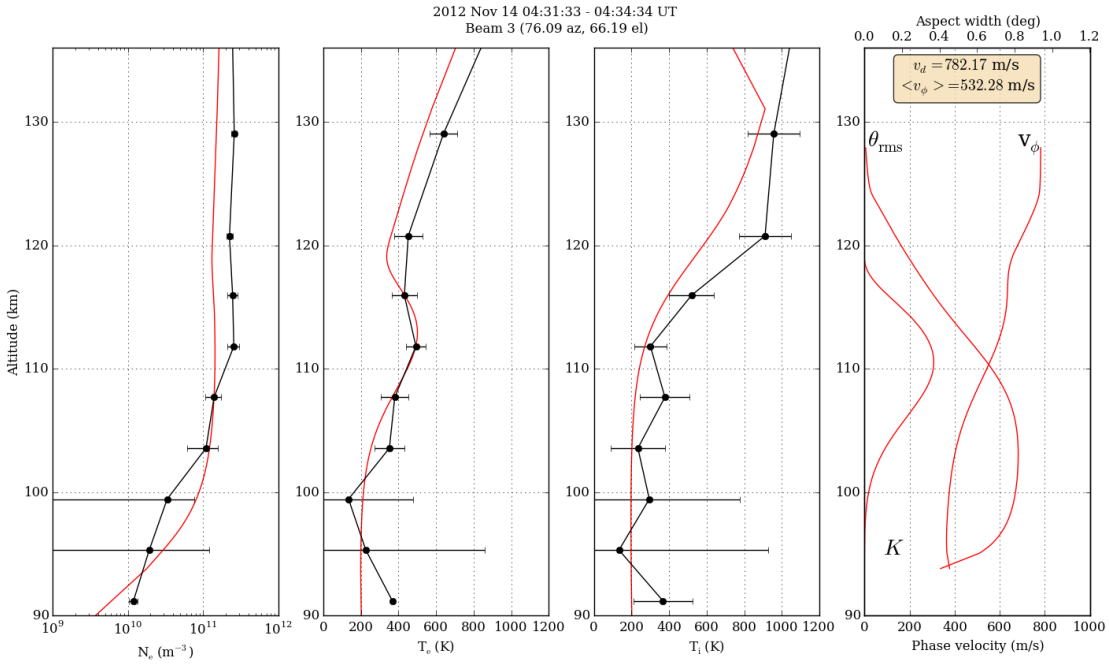

Figure 5.9: PFISR profiles compared with Farley Buneman wave model

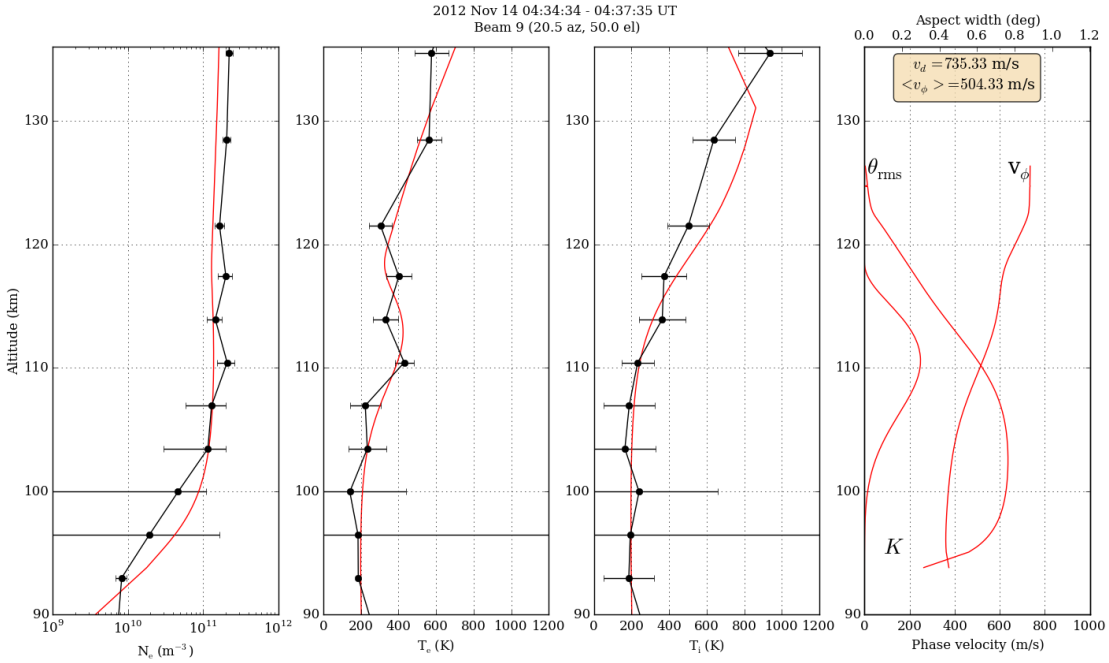

Figure 5.10: PFISR profiles compared with Farley Buneman wave model

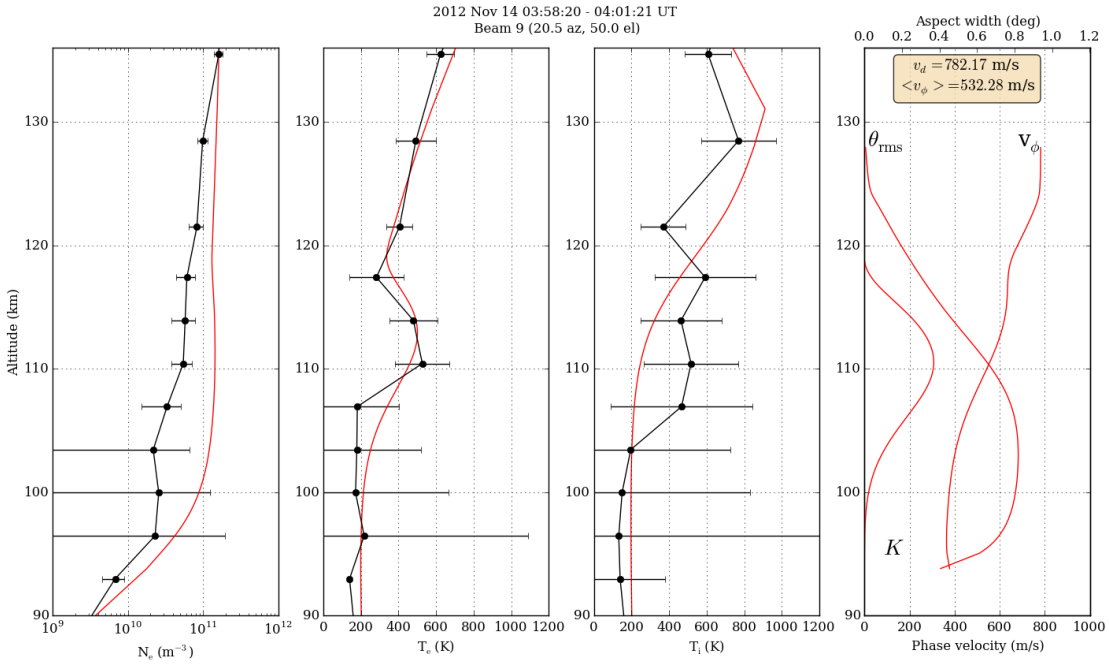

Figure 5.11: PFISR profiles compared with Farley Buneman wave model

phase velocity. This kernel-averaged phase velocity times the cosine of the flow angle represents an estimated Doppler velocity that a coherent scatter radar might observe without accounting for the radar's viewing geometry.

In Figure 5.3, the PFISR measurements from beam 0 on Nov 14, 2012 at 0422 UT were used to compare with the wave heating model. Beam 0 points to the northwest at -35.1° azimuth and 66.2° elevation and is labeled in Figure 4.3. For this three minute interval, in the region between 100 and 125 km, the χ^2 values for the electron density, electron temperature, and ion temperature profiles are 55.09, 6.27, and 7.72, respectively. These correspond to p-values of 0.00, 0.39, and 0.26. The p-values were calculated from a χ^2 distribution with 6 degrees of freedom. For the electron temperature profile, a p-value of 0.39 represents the probability of observing the same or more extreme result. Assuming a significance level of 0.05, the modeled profiles of electron and ion temperature meet the criteria for a good fit. The electron density profile in this figure does not meet the p-value significance level, however the model does not directly calculate the electron density due to Farley Buneman wave effects, and therefore we expect only an approximate model/data agreement for the density profiles.

The electron density and temperature measurements below 100 km have large error bars due to the lower density in the region. Above 100 km, the maximum percent difference between the modeled electron density profile and measurements is 48%. The model captures the enhanced electron temperatures that peak at 113 km altitude. The electron temperature decreases slightly at 121 km but does not decrease as dramatically as the modeled curve. Error bars on the ion temperature measurements are about two times larger than the electron temperature error bars for this time period. The modeled ion temperature curve also agrees

well with the PFISR measurements and the maximum percent difference between 100 and 125 km is 43%. The corresponding aspect width, wave phase velocity, and averaging kernel profiles are plotted on right most plot. The convection speed for these curves was 829 m/s and the kernel-averaged phase velocity was determined to be 561 m/s. This kernel-averaged phase velocity represents the maximum Doppler shift measurement a coherent scatter radar would observe if the line of sight of the radar was directly aligned with the Farley Buneman wavevector.

The other comparison plots (Figures 5.4 to 5.11) show similar model-data agreement. The electron density profiles generally agree with the PFISR measurements and the discrepancies in density are less than one order of magnitude. Similar to Figure 5.3, the error bars on the measurements below 100 km on the other plots are also larger due to lower densities in this region. The lower density results in a lower signal-to-noise ratio and a higher uncertainty in the measurements. The enhancements in the modeled electron temperature profiles peak at approximately the same altitude where the maximum temperature measurement was observed, although the altitude resolution for the PFISR is much lower than the model. The modeled ion temperatures increase in altitude similarly to the measured profiles, but slightly underestimate the ion temperatures between 105 and 125 km. The estimated background convection speed is greater than 780 m/s for all the datasets which is well above the required threshold velocity.

The χ^2 and p-values for all the PFISR/model comparison plots are shown in Table 5.1. Overall, the results show that the model is capable of reproducing fairly accurate electron and ion temperature profiles compared to the measured PFISR profiles. The majority of the electron and ion temperature profiles are above the p-value significance level of 0.05 which suggests that the model estimates meaningful

	N_e	T_e	T_i
Figure 5.3	13.82, 0.03	11.72, 0.06	2.67, 0.85
Figure 5.4	16.64, 0.01	19.86, 0.00	3.25, 0.78
Figure 5.5	53.72, 0.00	6.26, 0.39	5.84, 0.44
Figure 5.6	27.29, 0.00	2.03, 0.92	13.06, 0.04
Figure 5.7	42.88, 0.00	9.80, 0.13	9.99, 0.13
Figure 5.8	18.13, 0.00	23.53, 0.00	12.13, 0.06
Figure 5.9	55.09, 0.00	6.27, 0.39	7.72, 0.26
Figure 5.10	12.18, 0.06	6.08, 0.41	3.77, 0.71
Figure 5.11	24.97, 0.00	36.05, 0.00	2.95, 0.82

Table 5.1: χ^2 and p-values for the electron density, electron temperature, and ion temperature modeled profiles compared with profiles measured by the PFISR.

temperature profiles. Figure 5.6 had the best electron temperature agreement and Figure 5.3 had the best ion temperature agreement for the χ^2 test. The modeled electron density profiles do not reproduce the PFISR measurements as accurately as the temperature profiles and are not above the p-value significance threshold. However, the model reproduces the general shape of the electron density which is reasonable for the purposes of this study.

In the case of the 1 m wavelength Farley Buneman wave model, the maximum electron temperature is approximately 600 K for a convection speed of 970 m/s. At the same convection speed, the 5 m modeled waves reach a maximum electron temperature of 950 K. The difference is mostly due to stronger Landau damping at shorter wavelengths which results in less electron heating. When Farley Buneman waves were present, measurements of the maximum electron temperature between 100 and 120 km were typically between 600 and 1000 K. Thus, the 5 m wavelength model runs were chosen for the comparison plots.

The Farley Buneman wave model accounts for a single wavelength wave dur-

ing each run, however, the measurements from the PFISR contain a broadband spectrum of Farley Buneman wavelengths. The model runs of 1 m and 5 m waves display similar characteristics and capture many of the observed properties of Farley Buneman waves. While the 5 m wavelength modeled profiles agree with the ISR profiles of electron density and temperature and ion temperature, a broadband model of Farley Buneman wave heating would help to improve this agreement.

5.2.2 Coherent scatter radar observations

The PFISR/model comparison plots from the previous section showed that the model was capable of producing reasonable profiles of electron and ion temperatures. Additionally, the comparison provided estimates of the electron drift velocity and kernel-averaged phase velocity for three minute periods for a specific PFISR beam. To further validate the model, we compare these modeled kernel-averaged phase velocity estimates with Doppler velocity measurements observed concurrently from the Homer coherent scatter radar. The Homer spectral measurements can be inverted to estimate the wave phase velocity and flow angle. These values can then be compared with the model predicted, kernel-averaged phase velocities and the flow angle calculated from the PFISR line of sight drift measurements.

One challenge with comparing the Homer and PFISR datasets arises from the dissimilar spatial and temporal resolution of the two instruments. The Homer radar covers a wide region in latitude and longitude and a narrow range of altitudes over a short period of time ($\sim$5 seconds). On the other hand, the PFISR covers a smaller area in latitude and longitude and a wider range of altitudes over longer periods of time ($\sim$180 – 300 seconds). As a result of the longer PFISR integration times, several minute periods of constant convection are necessary for comparison

between the two radars. Typically, the convection is changing more rapidly than the PFISR can resolve, and it is difficult to find overlapping datasets with constant convection speeds.

To make a sensible comparison between the two radars, the Homer radar must observe backscatter from volumes that are co-located with the PFISR and the PFISR must observe the Farley Buneman wave heating. For the PFISR data, the presence of Farley Buneman waves is indicated by enhanced electron temperatures that peak at approximately 110 km altitude. For the coherent scatter radar data, two types of echoes, "diffuse" and "discrete" radar aurora, have been described by *Greenwald et al.* [1973]. The diffuse radar aurora are typically observed equatorward of auroral arcs. Both types of echoes are observed with the Homer radar, however due to high conductivity within the arcs, electric fields and Farley Buneman waves are suppressed, and a coherent scatter radar will not observe any echoes from within the arc region. If an auroral arc extends through the co-located volumes of the PFISR and Homer radar, a comparison can not be made due to the lack of coherent backscatter. When a time interval meeting these criteria is found, the PFISR profiles can be matched with the modeled profiles, and a kernel-averaged phase velocity can be estimated. This can then be compared with the Doppler velocity measured by the Homer radar by using the relationship that states that the Doppler velocity is equal to the wave phase velocity times the cosine of the flow angle.

As described in Section 4.2.1, the Homer coherent scatter radar can process RTI plots and 2-D imagery of the coherent backscatter spectral moments. Figure 5.12 shows an RTI plot for an hour of data starting at 0400 UT on November 14, 2012. The brightness and hue of each pixel corresponds to the echo intensity and Doppler

velocity, respectively. The Doppler shift measurements are organized such that red (blue) pixels are moving away (toward) the radar line of sight. Line of sight Doppler measurements can be made between ±675 m/s without aliasing. A brief data gap exists around 0418 UT and a strong meteor echo occurs around 0442 UT and 240 km range. Figures 5.13 and 5.14 display spectral images at 0422 and 0423 UT on the same day as the RTI plot. Each pixel in these figures represents the first three moments of the Doppler spectrum measured in the particular range and azimuth bin. The brightness, hue, and saturation of the pixel corresponds to the echo intensity, Doppler shift, and spectral width respectively. The signal to noise ratio ranges from 0 to 17 dB in both images. The spectral width measurements are arranged such that narrow spectral widths are plotted with pure tones, while wide spectra are plotted with pastel tones. The spectral width measurements range between 0 and 675 m/s. The incoherent integration time for the coherent scatter radar imagery was approximately 5 seconds.

This radar imagery was recorded during the same interval as Figure 5.3. The imagery shows intense backscatter with small Doppler shifts and broad spectra. The radar line of sight is centered on magnetic north and measures along a broad range of azimuth angles. Farley Buneman waves generally propagate in the zonal direction, and therefore, small Doppler shifts are expected for this radar geometry.

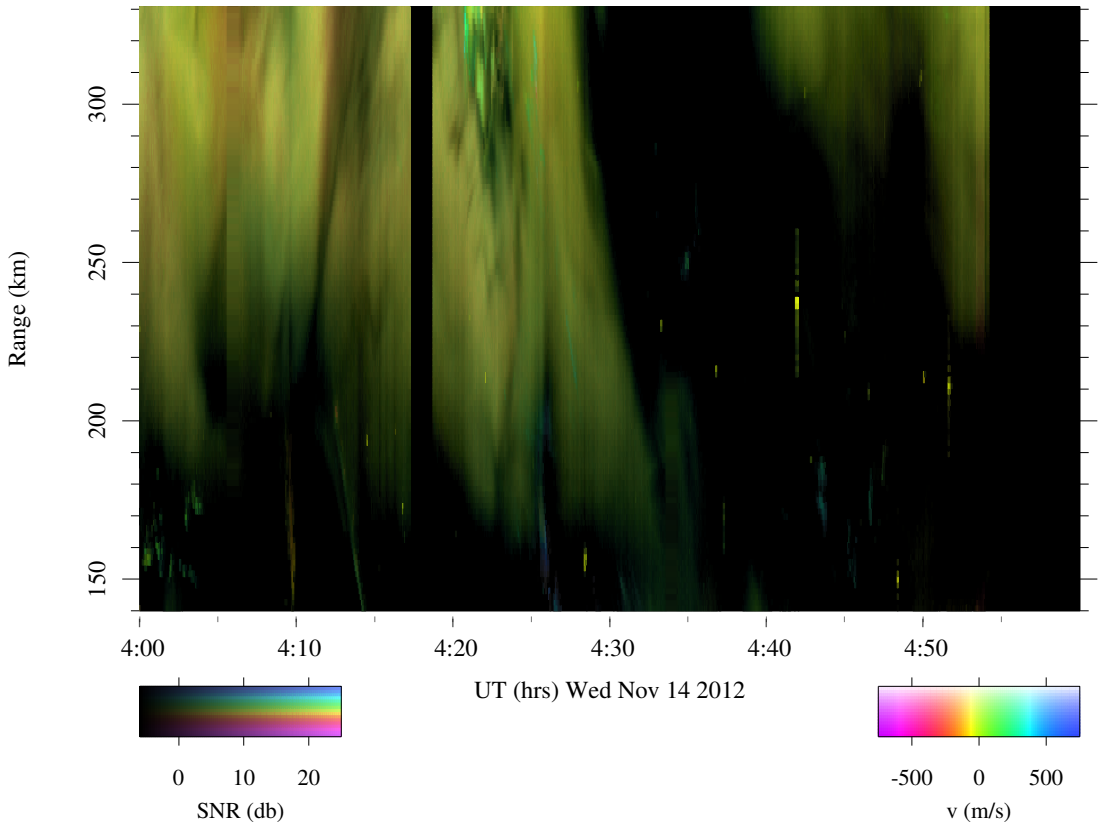

Figure 5.12: Range-Time-Intensity (RTI) plot from Homer radar for November 14, 2012. The color value and hue represent the SNR and Doppler shift, respectively. The range axis represents the apparent range to the target. Add 500 km to this axis for the true range to the target.

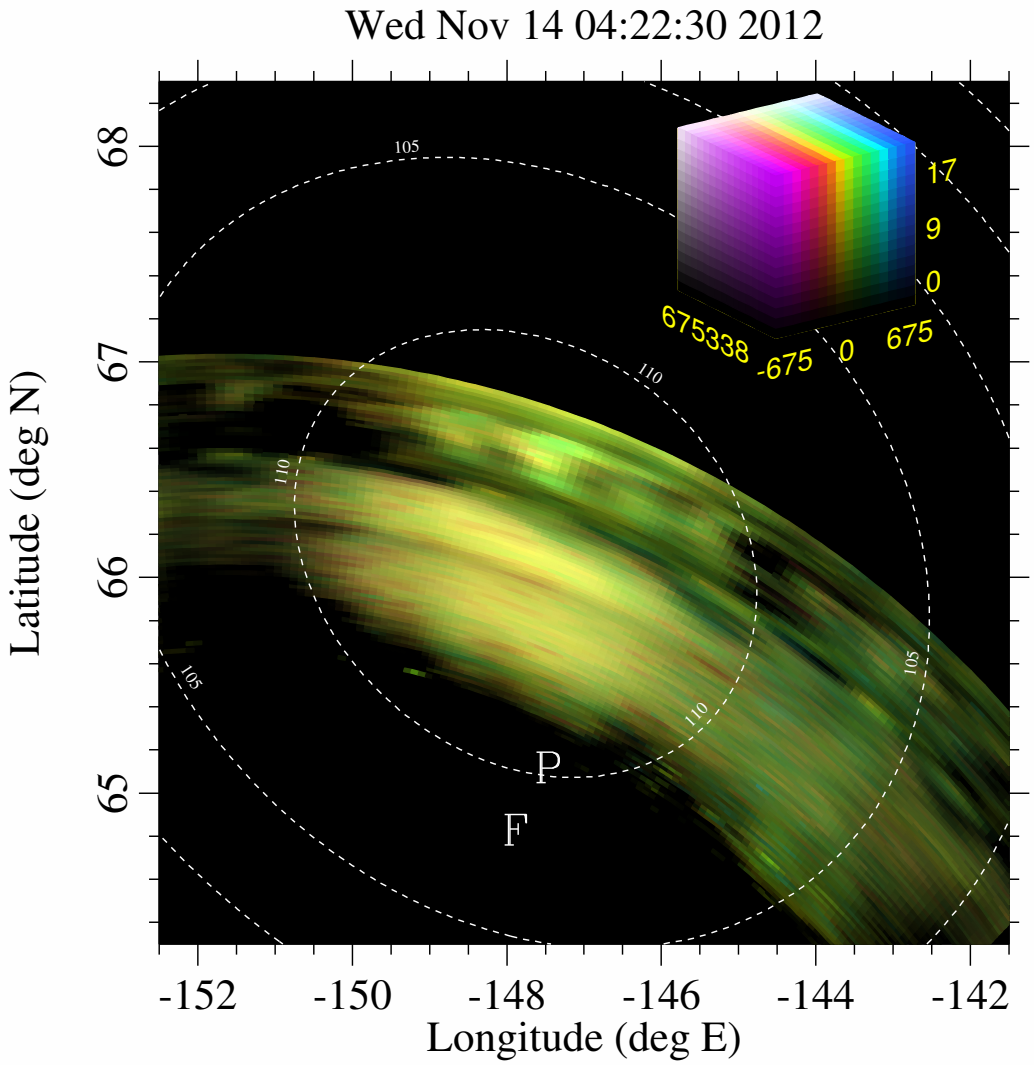

Figure 5.13: Imagery from Homer radar for November 14, 2012. The color value, hue, and saturation represent the SNR, Doppler shift, and spectral width respectively. The "P" symbol marks the location of the PFISR radar and the "F" marks Fairbanks, Alaska.

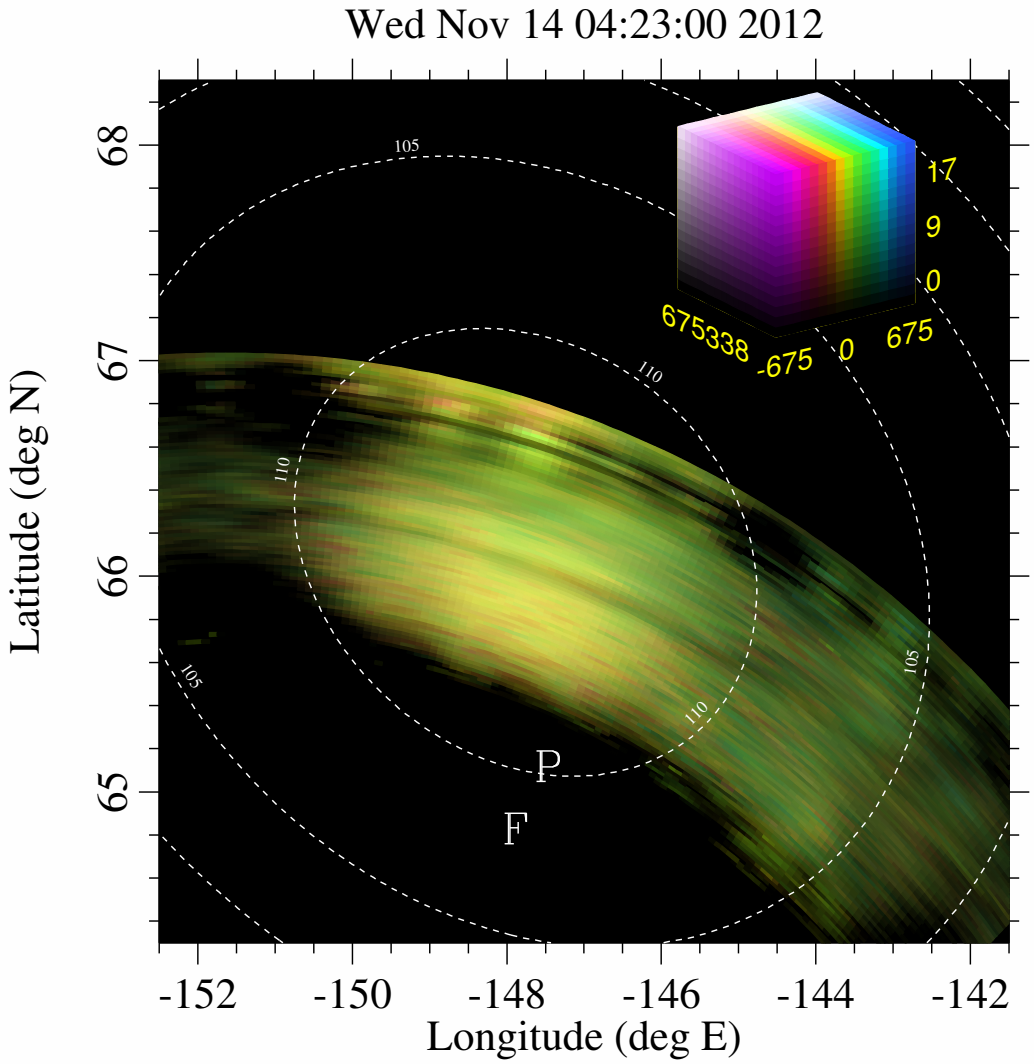

Figure 5.14: Imagery from Homer 30 seconds after Figure 5.13.

To compare the spectral data in Figures 5.13 and 5.14 with the PFISR measurements, we identify the common volumes of both radars. First, the geocentric location of each scattering volume of the PFISR is computed from the elevation, azimuth, and range of each volume to the PFISR ground station. Next, the range and bearing of each PFISR volume to the Homer radar ground station is calculated. These range and bearing values can be equated to a particular range and azimuth bin in the spectral images shown in Figures 5.13 and 5.14. This allows us to determine the Doppler velocity and spectral width component of the Farley Buneman waves relative to the Homer radar within each scattering volume of the PFISR radar.

To evaluate whether the coherent scatter spectral moments of Doppler velocity and spectral width support the phase velocity estimates from the model, the flow angle (the angle between the radar line of sight and the direction of wave propagation) must be estimated. As reviewed in Section 2.1, Doppler velocities measured by radars has shown sensitivity to the flow angle of Farley Buneman waves. Simulations of radar backscatter from Farley Buneman waves developed by *Oppenheim et al.* [2008]; *Oppenheim and Dimant* [2013] revealed further insight to this relationship. The simulations show that the Doppler shifts of the echoes follow a cosine dependence with respect to the flow angle, while the spectral width follows a sine dependence. The simulated Doppler shift measurements were calculated by computing the frequency spectrum of the electron density at 4 particular wavelengths (0.75, 1.5, 3.0, and 6.0 m) for varying flow angles. The simulated spectral width measurements were computed by calculating the standard deviation of a Gaussian fit to the density spectra.

Experimental evidence of field aligned irregularities from Jicamarca during day-

time counter equatorial electrojet conditions also validated the cosine of the flow angle and sine of the flow angle relationship between the Doppler shift and spectral width, respectively [*Woodman and Chau*, 2002; *Hysell et al.*, 2014]. Under counter electrojet conditions, current flows westward, opposite from the typical daytime direction of the flow and irregularities arising from the gradient drift instability are suppressed. These conditions allow radars to observe the characteristics of "pure two-stream waves", which are also observed by rockets when they pass through the topside of the ionosphere, above the density gradient *Pfaff et al.* [1982, 1987]. Analysis of the pure two stream wave data from both the radar and rocket experiments confirmed this cosine relationship.

To account for flow angle effects on coherent scatter radar measurements, we can use the fact that the spectral moments of the altitude average are the altitude average of the spectral moments. The Doppler shift of the coherent backscatter at the altitude z is given by

$$\overline{\omega/k} = C_s(z)\cos\theta \tag{5.14}$$

where the overbar represents a Doppler spectrum-weighted frequency average, and θ is the flow angle, which is assumed to be independent of altitude. The $\cos\theta$ term incorporates the cosine dependence observed in radar experiments like *Hanuise* [1983]; *Nielsen and Schlegel* [1983] and in the simulations of *Oppenheim et al.* [2008]. Taking the altitude average of this Doppler shift yields

$$\overline{\langle\omega/k\rangle} = \langle\overline{\omega/k}\rangle = \langle C_s\rangle\cos\theta \tag{5.15}$$

where the angle brackets denote a kernel-weighted altitude average, and $\langle C_s\rangle$ is the kernel-averaged phase velocity. This equation states that the first moment of the altitude averaged spectrum is the altitude average of the spectral first moments.

Similarly, we can use radar observations and Farley Buneman simulations to define the spectral width as

$$\overline{(\omega/k)^2} - \overline{\omega/k}^2 = \beta^2 C_s^2(z) \sin^2\theta \tag{5.16}$$

where β is a constant less than unity. This constant can be adjusted until the measured spectral moments are reproduced. Values of β^2 close to 1/2 have been found to match the auroral observations of the Homer radar, as well as equatorial electrojet observations [*Hysell et al.*, 2008a, 2009]. From this, the altitude-averaged spectral width can be calculated by

$$\begin{aligned}
\overline{\langle(\omega/k)^2\rangle} - \overline{\langle\omega/k\rangle}^2 =& \langle\overline{(\omega/k)^2}\rangle - \langle C_s\rangle^2 \cos^2\theta \\
=& \langle\beta^2 C_s^2(z)\sin^2\theta\rangle + \langle C_s^2(z)\cos^2\theta\rangle - \langle C_s\rangle^2\cos^2\theta \\
=& \beta^2\sin^2\theta\langle C_s^2\rangle + \cos^2\theta\left(\langle C_s^2\rangle - \langle C_s\rangle^2\right) \qquad (5.17) \\
\geq& \beta^2\sin^2\theta\langle C_s\rangle^2 \qquad (5.18)
\end{aligned}$$

For both the 1 m and 5 m model runs, $\langle C_s\rangle^2$ is approximately equal to $\langle C_s^2\rangle$ and the spectral width of the altitude-averaged spectrum can be estimated with $\beta^2\sin^2\theta\langle C_s\rangle^2$. Therefore, with two equations and two unknowns, these equations can be solved to estimate the convection speed and direction from the Doppler shift and spectral width measurements.

To compare the spectral measurements from the Homer radar with the model and PFISR data, Equations (5.15) and (5.18) can be inverted to estimate the kernel-averaged wave phase velocity, $\langle V_\phi\rangle$, and the flow angle, θ, from the Homer radar spectral measurements. The wave phase velocity derived from the Homer measurements can be compared with the estimated kernel-averaged phase velocity from the model, and the flow angle estimated from the Homer measurements can

be compared with the flow angle independently estimated from the PFISR line of sight drifts.

For the time interval on between 0358 and 0401 UT on November 14, 2012, the Homer radar measured average Doppler shifts of 78 m/s and average spectral widths of 340 m/s in the region that shared a common volume with the PFISR beam 9. The spectral measurements used to calculate the averages had signal to noise ratios greater than 7 dB. Solving Equations (5.15) and (5.18) for $\langle V_\phi \rangle$ and θ yields

$$\langle V_\phi \rangle = \sqrt{m_1^2 + m_2^2} \tag{5.19}$$

$$\theta = \arctan(-m_2/m_1) \tag{5.20}$$

where $m_1 = \overline{\langle \omega/k \rangle}$ and $m_2 = \frac{1}{\beta}\left[\overline{\langle (\omega/k)^2 \rangle} - \overline{\langle \omega/k \rangle}^2\right]$. Adapting the value of $\beta = 1/2$ from *Hysell et al.* [2009], estimates of the kernel-averaged phase velocity and flow angle for this time interval and volume are 684 m/s and 96.5 degrees, respectively.

Figure 5.11 shows the PFISR/model comparison for the same time interval between 0358 and 0401 UT on November 14, 2012. The estimated convection velocity for 5 m wavelength Farley Buneman waves for this 3 minute interval was 782 m/s and the kernel-averaged phase velocity approximately 532 m/s. This phase velocity estimate agrees with the phase velocity estimate from the Homer radar (684 m/s) with 22% relative error. The long integration time of the PFISR is most likely the largest source of this error. Averaging the coherent scatter measurements for 3 minute periods is not ideal because of the dynamic nature of the convection. However, for this example, the model estimates are reasonably accurate to predict the kernel-averaged phase velocity of the Farley Buneman waves.

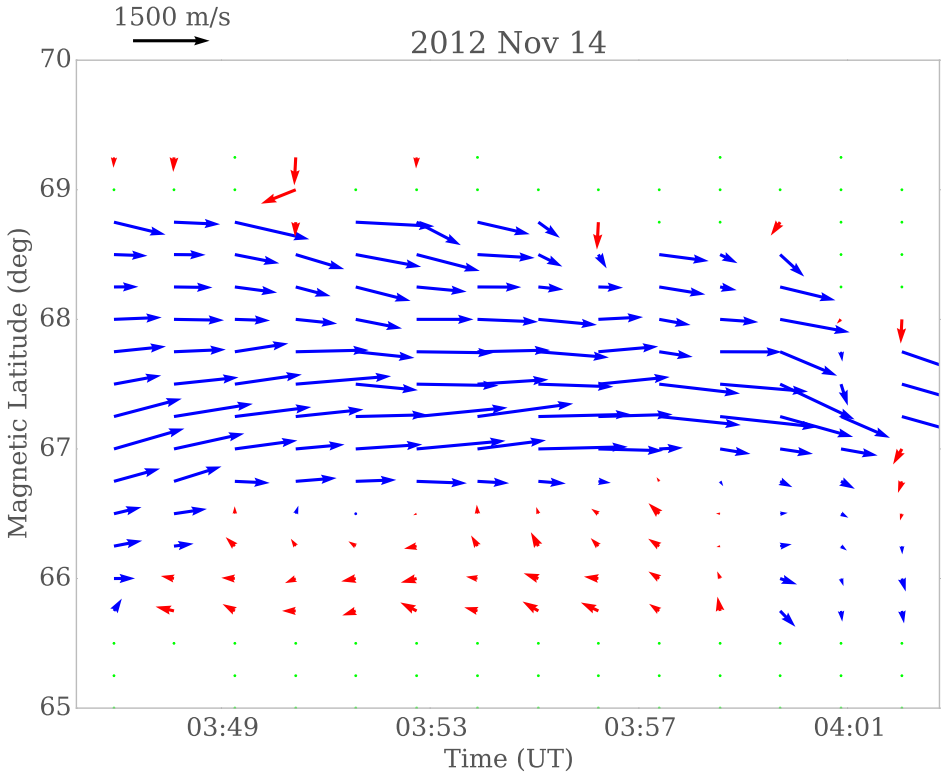

Figure 5.15: Line of sight drift velocities estimated by the PFISR on November 14, 2012. Green dots indicate that the estimated error was greater than 300 m/s and the velocity estimates were omitted.

The PFISR line of sight drift measurements can be used to estimate the flow angle, i.e., the angle between the direction of wave propagation and the Homer radar line of sight. Figure 5.15 shows the line of sight drift velocity vectors estimated every 60 seconds between magnetic latitudes of 65.5 and 69.5 degrees. Red (blue) vectors indicate flows to the west (east). During the interval from 0358 and 0401 UT, the average line of sight drift was directed approximately 8 degrees south of geomagnetic east. The center of the Homer radar beam is nominally directed toward geomagnetic north which makes the flow angle equal to approximately 82 degrees. This estimate agrees with the Homer estimate of the flow angle (96.5 degrees) with 15% relative error. We would expect this error to improve with

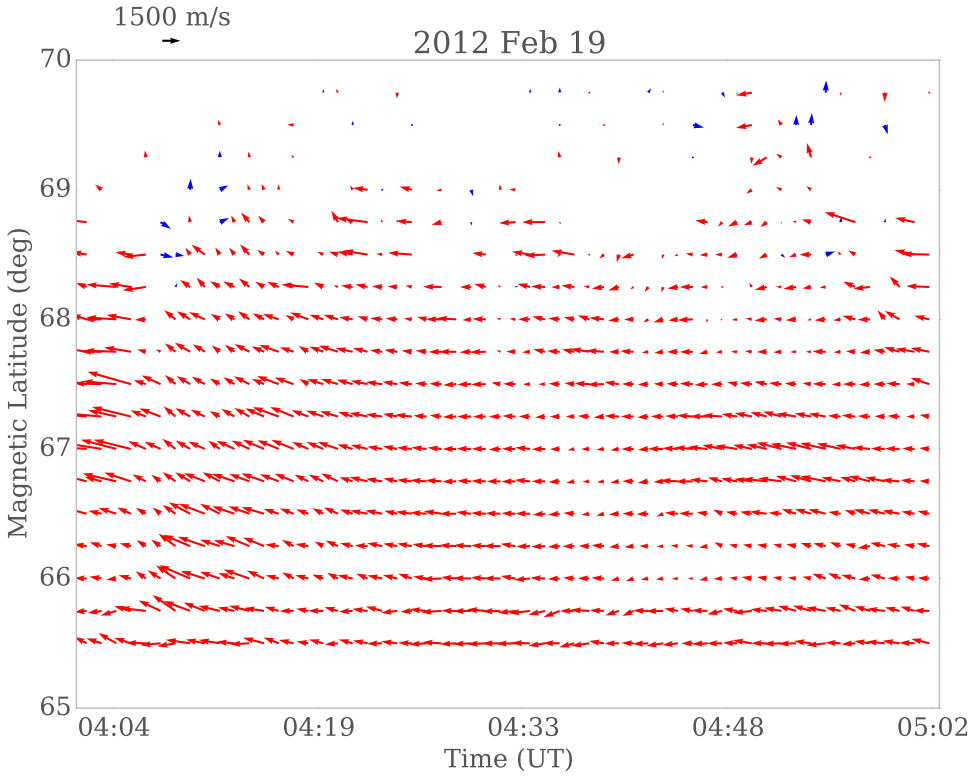

Figure 5.16: Line of sight drift velocities estimated by the PFISR on February 19, 2012.

higher temporal and spatial resolution data from the PFISR.

Table 5.2 shows kernel-averaged phase velocity and flow angle estimates for different intervals and different common radar volumes. The first three columns show the date, time, and PFISR beam number. The next two columns compare the estimated kernel-averaged phase velocity from the Homer spectral measurements with the estimates from the Farley Buneman wave model. Overall, the average relative error between the independently derived estimates was 7.5%. The next two columns compare the flow angle estimated from the Homer spectral measurements with the estimates from the PFISR line of sight drifts. The average relative error between these estimates was 12.9%.

			$\langle V_\phi \rangle$ (m/s)		θ (deg)	
Date	Time (UT)	Beam	Homer	Model	Homer	PFISR
2012-11-14	03:58 - 04:01	9	684	532	96.5	82.0
2012-11-14	04:22 - 04:25	0	481	562	95.1	51.0
2012-02-19	04:34 - 04:37	0	659	657	92.2	99.6
2012-02-19	04:34 - 04:37	3	587	657	92.0	99.6
2012-02-19	04:34 - 04:37	8	568	562	91.5	99.6
2012-02-19	04:37 - 04:40	0	655	657	91.9	83.6
2012-02-19	04:37 - 04:40	3	593	625	92.5	83.6
2012-02-19	04:37 - 04:40	8	565	593	91.4	83.6
2012-02-19	04:40 - 04:43	0	645	657	91.8	83.3
2012-02-19	04:40 - 04:43	3	493	562	92.6	83.3
2012-02-19	04:40 - 04:43	8	388	421	92.5	83.3

Table 5.2: Comparison of kernel-averaged wave phase velocity, $\langle V_\phi \rangle$, and flow angle, θ, predicted from Homer spectral measurements, PFISR LOS drift measurements, and Farley Buneman wave model.

The comparison from Table 5.2 reveals that for periods of constant convection, the Farley Buneman wave model produces reasonable estimates of the kernel-averaged phase velocity. Relative errors of 7.5% are acceptable considering the long integration times and low spatial resolution of the PFISR. Additionally, the discrete number of convection speeds chosen for the model runs influences the accuracy of the estimated phase velocities from the model. Since the model was run for 13 convection speeds, there are only 13 estimates of kernel-averaged phase velocities that can be matched with the Homer measurements. In most cases, the model phase velocity estimate matches the measured data fairly close, but the agreement would most likely improve by running the model for more convection speeds.

The comparison in Table 5.2 also shows that the inversion of the Homer spectra can reasonably estimate the flow angle. The line of sight drifts from the PFISR

are estimated every 0.25 degrees of magnetic latitude and every 60 seconds. The measurements are made using a 72 km long pulse that probes the F region. The oversampling of this long pulse results in spatial filtering and poor spatial resolution. The long integration times result in low temporal resolution which effectively filters out fast moving, small-scale features. Despite these issues, the agreement between the Homer and PFISR estimated flow angle is satisfactory.

Coherent scatter radar measurements could also contribute to estimate errors if spectral aliasing of the data occurs, if the radar measures backscatter from meteor echoes, or if there is large amounts of ground clutter. Additionally, estimate errors can increase if the neutral wind velocity is not uniform throughout the radar field of view or if there is a significant amount of E region Joule heating.

5.3 Conclusions

This chapter outlined a model of Farley Buneman waves and heating that incorporated the heuristic model of *Milikh and Dimant* [2002] into the global ionospheric model, SAMI2. The model reconstructed profiles of electron temperature, electron density, ion temperature, and heating rates to show the finite span of altitudes that are effected by the Farley Buneman instability. The modeled electron temperature profiles predicted enhancements at altitudes that were consistent with sounding rocket experiments and theoretical calculations. Profiles of wave phase velocity and aspect width provided insight into the behavior of the Farley Buneman waves that can not be observed with ground based instrumentation. Additionally, the model emphasized the importance of using a temperature dependent ion acoustic speed when considering the threshold phase velocity of Farley Buneman waves.

The modeled profiles were weighted with an averaging kernel to assess the phase velocities and aspect widths that a coherent scatter radar might observe.

The model was then compared with measured profiles from the PFISR to validate the estimates and to estimate the kernel-averaged phase velocity at a particular time interval and beam volume. The PFISR electron and ion temperature profiles were found to be consistent with the modeled profiles. However, this comparison is not possible when the convection changes more rapidly than the PFISR can resolve. Integration times for the PFISR are typically $3 - 5$ minutes, while the convection velocity can change within a few seconds. We expect that the model and empirical formulas would still be valid under periods of rapidly varying convection because the properties of Farley Buneman waves do not change dramatically as a function of time.

Coherent scatter radars were also used to validate that the model convection speeds and model estimates of kernel-averaged phase velocities were reasonable. The range of convection speeds used in the model was validated by the average convection velocity obtained by analyzing 6 years of SuperDARN observations. Doppler spectra measurements from the Homer 30 MHz coherent scatter radar were inverted to estimate the kernel-averaged wave phase velocity and flow angle. These estimates were compared with estimates from the Farley Buneman wave model and measurements from the PFISR. Reasonable agreement was found between the different data sets. The long integration times and poor spatial resolution of the PFISR limited the data intervals that could be analyzed, but we expect that similar results could be obtained during periods of varying convection.

CHAPTER 6

ESTIMATING AURORAL CONVECTION WITH COHERENT SCATTER RADAR OBSERVATIONS

In this chapter, coherent backscatter measurements from plasma density irregularities are inverted with a heuristic model to estimate convection velocity and the auroral convection pattern. The heuristic equations developed by *Bahcivan et al.* [2005]; *Hysell et al.* [2008a] are used to invert the moments of the measured Doppler spectra to estimate the electron convection velocity in the radar's field of view. To estimate the convection pattern, the convection velocities are fit using a least squares solver with regularization to estimate potential contours that minimize the discrepancy between the convection velocity estimates while enforcing a smoothness constraint on the contours. Overall, the convection velocity estimates derived from the measured Doppler spectra are found to be reasonably accurate and can be used to develop regional maps of the convection pattern.

6.1 Estimating convection with coherent backscatter spectra

The small-scale spatial structure of the auroral ionosphere is thought to be closely related to magnetosphere-ionosphere system. Therefore, information about the small-scale electrodynamics is required to fully understand how energy is coupled between the magnetosphere and ionosphere. Ground based instruments cannot directly measure these parameters, and in-situ instruments cannot completely capture the dynamics of the region for long periods of time. Coherent scatter radar spectral measurements can be used to estimate the convection speed and the con-

vective potential electric field at small scales. These quantities are important for understanding the characteristics of Farley Buneman waves and for producing high resolution maps of the electric fields in the E region.

6.1.1 Empirical model

The methods outlined in *Bahcivan et al.* [2005] and *Hysell et al.* [2008a] can be used to estimate the electron convection speed using coherent scatter radar spectra. The forward model is given by

$$\langle \omega/k \rangle = V_o \cos(\theta - \theta_o) + v_i \tag{6.1}$$

$$\langle \delta\omega/k \rangle_{rms} = \frac{1}{2} V_o |\sin(\theta - \theta_o)| \tag{6.2}$$

$$V_o = 350 + (V_d/100)^2 \tag{6.3}$$

where $\langle \omega/k \rangle$ is the Doppler shift, $\langle \delta\omega/k \rangle_{rms}$ is the spectral width, v_i is the E region line of sight, wind-induced ion drift speed, θ is the flow angle with respect to the radar line of sight, and θ_o is an offset angle used to account for turning due to thermal effects. For the datasets presented in this chapter, we take $\theta_0 = 10^\circ$ and assume that the neutral winds are mainly transverse to the radar line of sight, i.e., $v_i = 0$.

The forward model described with Equations (6.1) to (6.3) can be inverted to estimate the V_d and θ variables from the spectral measurements of the coherent scatter radar (Doppler shift and spectral width). This method requires knowledge of the general direction of the convection, either strictly westward (right-to-left) or eastward (left-to-right) from the point of view of the radar. Additionally, the model restricts the convection speed estimates to be greater than 350 m/s. This is

a sufficient assumption for our data because irregularities will only form when the convection is greater than the ion acoustic speed which is variable, but typically never less than 350 m/s. These equations can be inverted in every bin in the radar field of view which provides high resolution convection velocity estimates in the auroral E region.

To estimate a convection pattern from the electron convection velocity vectors, a regularized, nonlinear least squares solver, as outlined in *Aster et al.* [2005], was used to numerically solve for the potential field on a 2-D grid. The solver minimizes the sum of the model predicted error and the model curvature. The regularization scheme weights the penalties on the errors and model curvature to estimate a smooth convection pattern with small residuals. The initial guess for the algorithm is computed by calculating a potential grid from the velocity estimates in each bin. This initial guess is input to the solver which implements the Levenberg-Marquardt algorithm to solve the nonlinear least squares problem. The algorithm stops when the relative error of the sum of the squares is less than 1×10^{-6}.

6.1.2 Results

The data in Figure 6.1 plots coherent scatter spectral moments (colored pixels), estimated convection velocity (blue lines), and estimated convection pattern (green contours) from December 8, 2013 at 05:07:48 UT. To the right of the figure, the color legend shows the values of the spectral moments and the blue line segment represents the scale of the convection velocity vectors in mV/m. The first three moments of the coherent scatter radar spectra are plotted in the same format as previous datasets with the brightness, hue, and saturation signifying the SNR,

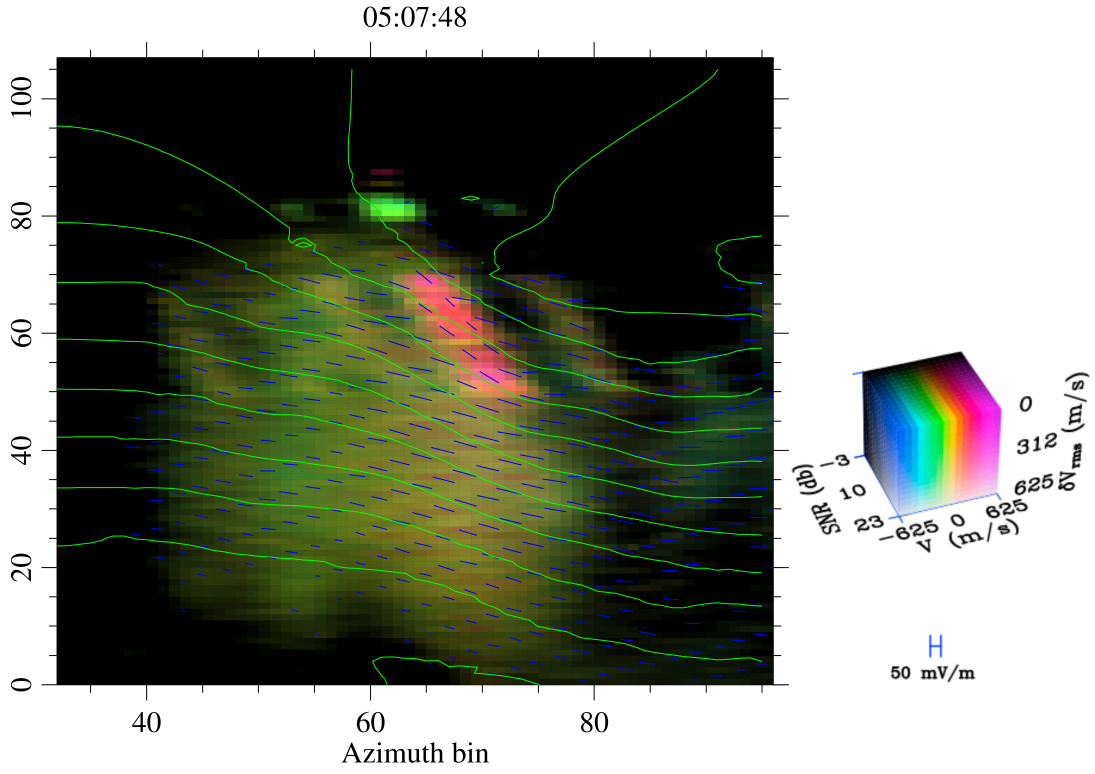

Figure 6.1: Convection pattern from Homer radar at 05:07:48 UT December 8, 2013. Colored pixels represent the first three spectral moments measured by the coherent scatter radar. Blue lines represent the convection velocity. Green contours represent the convection pattern.

Doppler shift, and spectral width, respectively. The convection velocity is estimated at every range and azimuth bin, but a limited number of vectors are plotted here to make the figure easier to view. The estimated equipotential contours are plotted with green lines and the spacing between each of these contour lines is 1 kV.

The coordinate system of the plot is in the frame of reference of the coherent scatter radar with azimuth bins on the abscissa and range bins on the ordinate. There are 120 range bins, each bin has a width of 1.8 km, and 127 azimuth bins,

corresponding to direction cosines uniformly sampled between ±0.4. The direction cosine represents the sine of the azimuth angle relative to the direction of the main beam of the radar. The first range bin is approximately 660 km from Homer. The range of azimuth bins on the plot (numbers 31 to 95) are focused on the region of the main antenna beam pattern and correspond to a direction cosine of ±0.2.

Diffuse radar aurora fills almost the entire Homer radar field of view, except in the most distant range bins, above bin 85. The enhanced SNR and varying Doppler shifts near the far boundary suggests the presence of field aligned currents between the radar aurora and the auroral arc. The wide separation between the contour lines suggests that the convective electric field is of constant strength in this volume of the E region. In areas where there is weak or no coherent backscatter, the empirical equations can not be inverted, and we assume that the electric field remains uniform in this area. The absence of radar backscatter suggests that there is weak convection in these areas and the threshold for the Farley Buneman instability is not met.

Estimates of convection speed and direction generally change slowly and conform to changes in the measured Doppler spectra. Based on PFISR line of sight drift measurements, we assumed a westward convection for this time interval. In a majority of the volume, the convection is westward and slightly increases at further range bins. Since the convection is mostly perpendicular to the line of sight of the radar, the radar measures small Doppler shifts. In the northern part of the scattering volume, around range bin 60, azimuth bin 70, the radar detects irregularities travelling away from the radar line of sight. In this region, the empirical model estimates convection speeds aligned closer along the line of sight of the radar.

The residuals of the nonlinear least squares fit indicate the quality of the es-

timated convection pattern. Solutions with small residuals imply a good fit and that the potential flow field is incompressible, i.e., the divergence of the flow velocity is zero. This fact allows the algorithm to be self-validated to the extent that a unique potential function can be found that gives rise to a flow that conforms to the forward model with small residuals. The residuals are calculated as the RMS discrepancy between the velocity estimates from the model convection pattern as a fraction of the total model RMS electric field. For the data shown in Figure 6.1, this fraction, or relative RMS error, is less than 24%. It is possible to improve the residuals by relaxing the penalties on the smoothness parameter, however this compromises the stability of the algorithm. Inconsistencies with the coherent scatter spectral measurements also can contribute to these errors. These inconsistencies can arise from spectral aliasing, ground clutter, or meteor echoes. Additionally, larger residuals will arise if the neutral winds or wave turning are non-uniform throughout the illuminated volume.

Figures 6.2 and 6.3 show convection patterns from February 19, 2012, separated by 16 seconds. These two figures reveal the dynamic nature of the convection in the auroral region. Within this short period, observed Doppler shifts increase throughout the volume in both the positive and negative direction. Additionally, the estimated convection speeds and pattern change from a general alignment in the zonal direction to a more variable flow with more components in the meridional direction. Diffuse radar aurora was observed from range bins 0 to 40 in Figure 6.2 and 16 seconds later, the radar aurora expanded northward approximately 180 km (10 range bins) in Figure 6.3. The relative RMS errors for these two time frames were 19% and 28%, respectively. The reason for the larger residuals in the second time interval is most likely due to the enforcement of the smoothness parameter on a turbulent convection pattern.

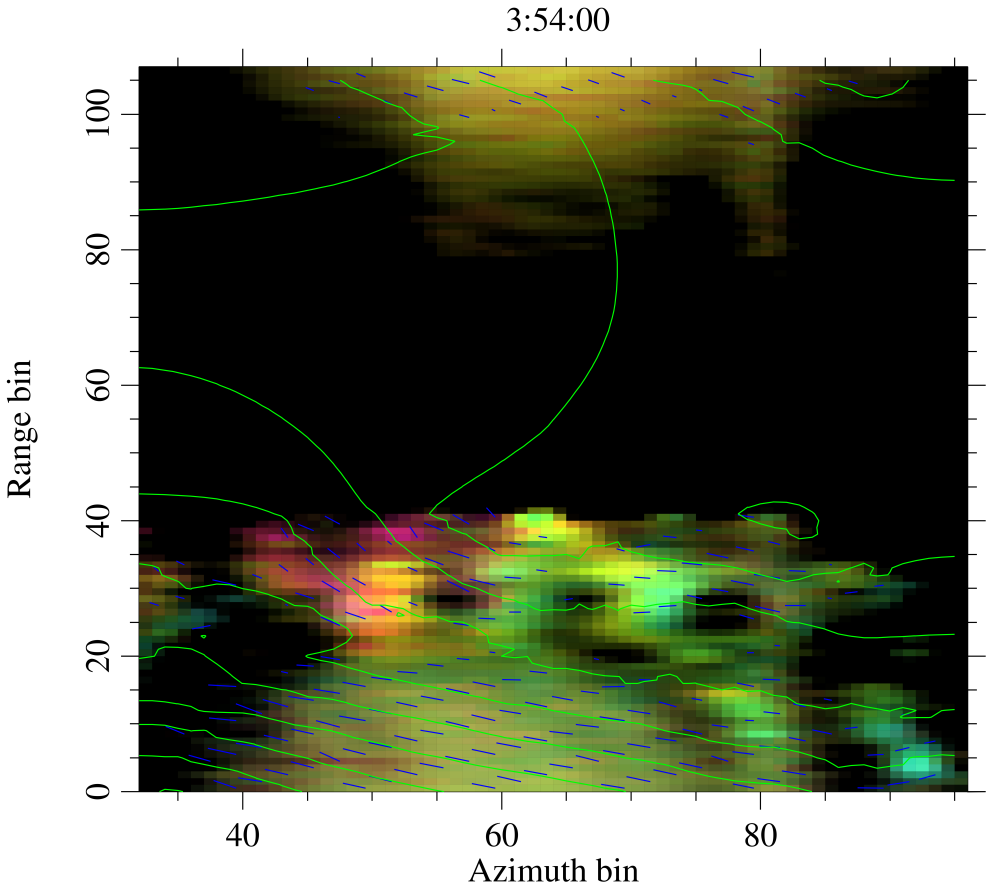

Figure 6.2: Convection pattern from Homer radar at 03:54:00 UT February 19, 2012

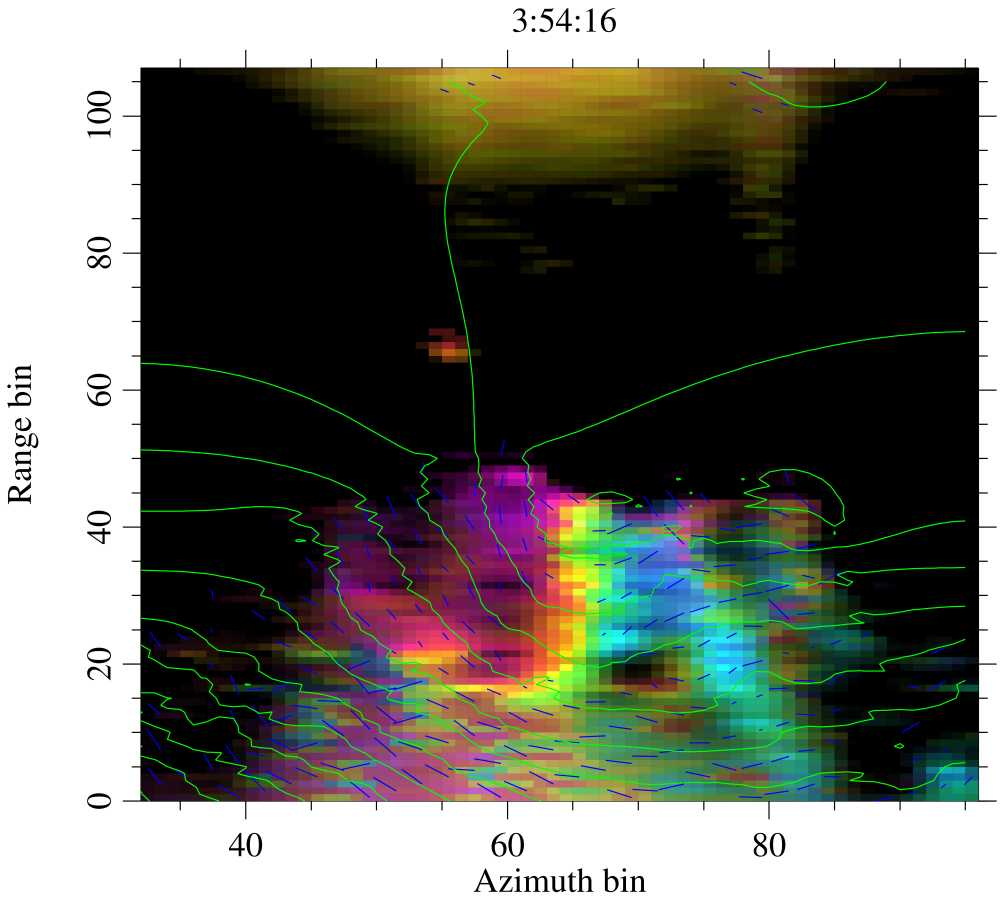

Figure 6.3: Convection pattern from Homer radar at 03:54:16 UT February 19, 2012

6.2 Conclusions

This chapter discussed the methods required to invert coherent scatter spectral measurements to estimate the convection velocity. The velocity estimates were then used as input to a nonlinear least squares solver which estimated the convection pattern within the radar image. Different datasets with uniform and non-uniform convection patterns were processed and were shown to have relatively small residuals. These small residuals indicate that the flow is incompressible which can only be represented by a solution that is found in nature. These convection velocity and convection pattern estimates show how coherent scatter radar data can be processed to provide more insight about the small-scale auroral convection pattern.

CHAPTER 7

ARTIFICIAL FIELD ALIGNED IRREGULARITIES DUE TO HF HEATING

This chapter examines artificial field aligned irregularities, or AFAIs, with experiments performed at HAARP and numerical simulations of these experiments, as previously reported by *Miceli et al.* [2013]. The purpose of the experiments was to determine the threshold of AFAIs generated by O-mode heating while they were being suppressed by simultaneous X-mode heating. The AFAIs were observed from Homer, Alaska with a 30 MHz coherent scatter radar. The importance of X-mode heating, D region absorption, and the pump standing wave ratio at the interaction height were evaluated with a numeral model based on the SAMI2 model.

7.1 Background

A hallmark of ionospheric modification experiments is the generation of field-aligned plasma density irregularities, which are sometimes termed "artificial" irregularities (see reviews by *Robinson* [1989]; *Frolov et al.* [1997]; *Gurevich* [2007]). The irregularities are believed to be generated by thermal parametric instabilities [*Grach et al.*, 1978; *Das and Fejer*, 1979; *Fejer*, 1979; *Kuo and Lee*, 1982; *Dysthe et al.*, 1983; *Mjlhus*, 1990] and, having entered nonlinear stages of development, by resonance instability [*Vaskov and Gurevich*, 1977; *Inhester et al.*, 1981; *Grach et al.*, 1981; *Dysthe et al.*, 1982; *Lee and Kuo*, 1983; *Mjlhus*, 1993]. Most research has concentrated on F region AFAIs, including a rocket experiment that flew through the artificially generated irregularities [*Kelley et al.*, 1995]. The volume was found to have hundreds of 10 m irregularities and the spectrum of the irregularities displayed a change in slope at high k numbers [*Franz et al.*, 1999].

This was verified by multiple radar observations from irregularities generated by the Platteville heater. *Franz et al.* [1999] predicted that the high k waves are likely due to the thermal parametric instability. Irregularities can also be generated in the E region by pump waves with sufficiently low frequency. Examples of E region AFAI generation have been described by *Djuth et al.* [1985]; *Coster et al.* [1985], and *Hysell et al.* [2010], among others.

Thermal parametric instability involves the linear mode conversion of an electromagnetic O-mode pump wave into an electrostatic mode (an upper hybrid wave, primarily) in the presence of zero-frequency field-aligned plasma density irregularities (the purely-growing mode) that grow in amplitude under the action of wave heating, leading to instability. Wave trapping can ultimately occur, giving rise to resonance instability. Whereas the latter can be sustained with very low pump-mode amplitudes, the former only occurs when the pump mode amplitude exceeds some threshold. *Dysthe et al.* [1983] presented a detailed derivation of the threshold for thermal parametric instability in the F region, and *Hysell et al.* [2010] generalized their work slightly for application in the E region, where the relatively high electron-neutral collision frequency and electron cooling due to inelastic collisions must be considered. Experiments with E region AFAIs showed reasonable agreement with the theory.

Since the threshold electric field increases with electron temperature, it would seem to be possible to increase the threshold and inhibit thermal parametric instability using X-mode heating at an offset frequency where the X-mode interaction height matches the upper-hybrid interaction height of the O-mode emission. The situation is complicated by at least two related factors, however. The first is D-region absorption, which will also be increased by X-mode heating and inhibit

AFAI generation in a manner unrelated to threshold considerations. The second is that the threshold for thermal parametric instability is influenced by the pump standing wave ratio at the upper-hybrid interaction height, itself related to local absorption. For E region experiments, all of these factors may be important.

Frolov et al. [1999] tested AFAI suppression in the F region by simultaneous X-mode heating. They concluded that both parametric decay instabilities and thermal parametric instabilities could be suppressed by X-mode heating at the optimal choice of interaction height. They identified three different timescales for the observed X-mode effects. *Gustavsson et al.* [2009] conducted F region experiments at HAARP, using optical airglow as a diagnostic. In their experiments, X-mode heating was found to reduce 6300 Å emissions. This was interpreted in terms of two of the three aforementioned effects: increased absorption due to X-mode heating and the temperature dependence of the threshold electric field for thermal parametric instability.

Afterward, *Hysell et al.* [2011] performed related experiments at HAARP, examining whether X-mode heating altered the threshold for O mode-induced E region AFAIs observed by coherent scatter radar. They found a drastic increase (more than a factor of four) in the O-mode pump power needed for AFAI generation when half the HAARP array was emitting X-mode at a selected offset frequency. Simple calculations suggested that all three of the aforementioned mechanisms working together could account for the increase. However, subsequent numerical modeling (described below) showed that such a drastic effect was unlikely. A subsequent review of the experimental procedure raised doubt about whether the effective radiated power (ERP) of the O-mode radiation in the 2010 experiments was consistent during periods with and without X-mode heating. The experiments have

consequently been repeated and accompanied by a more comprehensive modeling approach.

We report on a new series of experiments performed at HAARP in the summer of 2012. For these experiments, O-mode pumping at fixed ERP was accompanied by X-mode heating at an offset frequency. *E* region AFAIs were detected using the 30 MHz coherent scatter radar. O-mode power levels were varied, and the effect of X-mode heating on the threshold for AFAI generation was reassessed. This time, we find that the power required for irregularity generation increases by a factor of two or less when half the HAARP array emitted X-mode at a suitable offset frequency. These findings are more consistent with numerical modeling results.

7.2 Coherent scatter radar observations

The Ionospheric Research Instrument (IRI) at HAARP (High Frequency Active Auroral Research Program – 62.39N, 145.15W) was used to generate *E* region AFAIs. Experiments were performed using O- and X-mode emissions, vertical pointing, and changing, finely graduated O-mode power levels. The O-mode emission frequency was 2.75 MHz for all of our experiments. The frequency of the X-mode waves must be carefully selected such that the transmitted waves reflect at the upper-hybrid interaction height. This X-mode frequency can be calculated from the thermal parametric instability relation

$$\omega_o^2 = \omega_p^2 + \Omega_e^2 \tag{7.1}$$

and from the equation for the refractive index of an X-mode mode wave

$$0 = 1 - \frac{\omega_p^2}{\omega_x(\omega_x - \Omega_e)} \tag{7.2}$$

where ω_o is the pump wave frequency (2.75 MHz for these experiments), ω_x is the X-mode wave frequency, ω_p is the plasma frequency, and Ω_e is the electron gyrofrequency. Above HAARP, $\Omega_e \approx 1.75$ MHz. Combining Equations (7.1) and (7.2) yields

$$\omega_x^2 - \Omega_e \omega_x - \omega_o^2 + \Omega_e^2 = 0 \tag{7.3}$$

Solving this quadratic equation for ω_x yields the X-mode frequency at which the X-mode reflection height matches the upper-hybrid interaction height. For the experiments presented in this section, the X-mode frequency that satisfied these equations was 3.169 MHz.

For the experiments described in this chapter, the HAARP antenna array was divided into two subarrays, each an array of 7x12 elements. O- and X-mode emissions were generated using the two different subarrays. Using 100% of available subarray power, the 2.75 MHz O-mode and 3.169 MHz X-mode emissions would have had 79.9 dBW and 81.1 dBW effective radiated power (ERP), respectively. The ERP of a system is equal to the power supplied to the antenna times the gain of the antenna. While the X- and O-mode rays deviate spatially as the waves propagate upward, the deviation is very slight below the upper-hybrid interaction height in the *E* region. Consequently, the main beams of the two subarrays could both be directed toward zenith for these experiments.

The ionosphere over HAARP was probed with a coherent scatter radar interferometer located on Diamond Ridge overlooking Homer, Alaska. The locus of perpendicularity is at precisely 100 km altitude over HAARP, as required for observing artificial *E* region FAIs monostatically. The experiments utilized a 13-baud Barker coded pulse with a 9 μs baud length. The interpulse period for the radar experiments was 2.46 ms or 370 km. Doppler velocities as large as $\sim$1000 m/s can

be measured without frequency aliasing, which is necessary for observing natural auroral irregularities, although the Doppler shifts encountered during ionospheric modification experiments are typically an order of magnitude smaller. Specifications for the radar were given by *Hysell et al.* [2010]. The radar was recently relocated to Diamond Ridge and its array of receiving antennas expanded such that the longest interferometry baseline is presently 15 wavelengths long.

Experiments were performed during the week of May 6, 2012. A geomagnetic storm caused significant absorption during the experiments starting on May 8. Furthermore, the ionosphere was sufficiently dense during this time for sky waves and attendant radio interference to be present around midday when experiments were occurring. Data discussed in this section were selected from time intervals when absorption and interference were minimal. Additional experiments were subsequently performed the week of August 5, 2012, during geomagnetically quiet conditions.

In the experiments to test X-mode suppression of AFAIs, O-mode signals were generated at power levels (relative to the maximum available power) that varied in steps according to the schedule shown in Table 1. Power levels were sustained for 10 seconds intervals. Over time, the power was incremented or decremented in discrete steps according to a quadratic formula so that the electric field incident on the ionosphere varied approximately linearly. A one-minute gap introduced at the end of the cycle provided a total cycle time of 5 minutes. X-mode heating, meanwhile, was performed at full subarray power throughout every other O-mode heating interval. Consequently, the overall cycle time for the combined experiment was 10 minutes.

Figure 7.1 shows results from the experiments on May 7, 2012. The figure

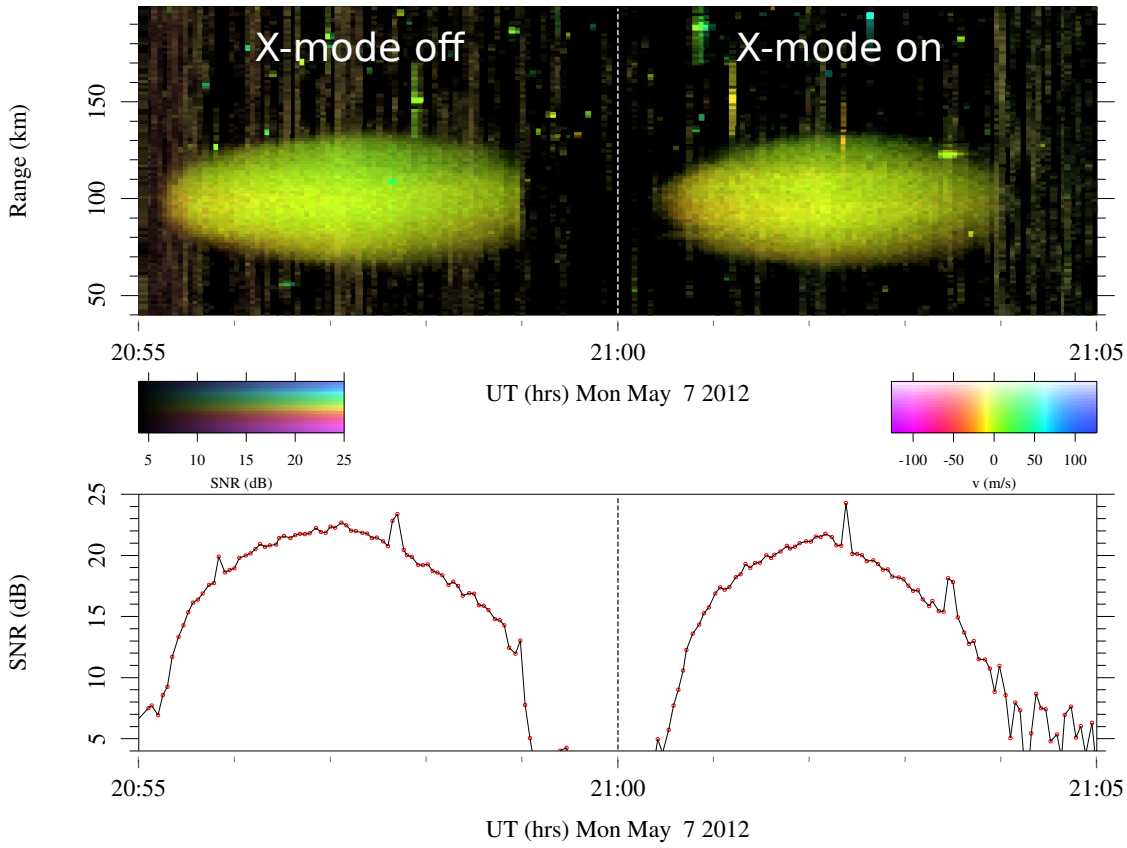

Figure 7.1: Range-time Doppler intensity (RTDI) plot of backscatter from artificial E region FAIs over HAARP observed on May 7, 2012. Here, the brightness, hue, and saturation of the pixels denote echo signal-to-noise ratio (SNR) from 3–25 dB, Doppler shifts from $\pm$ 125 m/s, and spectral width from 0–125 m/s RMS, according to the legends shown. Note that the echoes from heater-induced FAIs are range aliased and that their true range is greater than their apparent range by 370 km. The average signal-to-noise ratio for apparent ranges between 70–130 km is plotted beneath the RTDI plot. Variations in the line plot reflect both changes in the size of the modified volume and in the scattering intensity of regions within the volume. Echoes from meteor trails are visible throughout the figure. The incoherent integration time for the figure is about 3 s. X-mode heating was present during only the second 5-min. heating cycle.

Start	O-mode power (%)	
time (s)	May 2012	Aug 2012
0	0.00	0.00
10	11.25	4.00
	15.30	6.71
	20.00	10.12
	25.30	14.23
	31.25	19.04
60	37.80	24.55
	45.00	30.75
	53.00	37.65
	61.50	45.26
	70.50	53.56
	80.00	62.55
120	90.00	72.25
	80.00	62.55
	70.50	53.56
	61.50	45.26
	53.00	37.65
	45.00	30.75
180	37.80	24.55
	31.25	19.04
	25.30	14.23
	20.00	10.12
	15.30	6.71
	11.25	4.00

Table 7.1: O-mode heating power levels for onset threshold experiments. The second column corresponds to the observations in Figures 7.1 and 7.2, while the third column corresponds to the observations in Figure 7.3. Power step levels were maintained for 10-s intervals. The power percentages are with respect to the power available from an IRI subarray. X-mode emission was at full subarray power.

shows coherent scatter received by the 30 MHz radar versus slant range and time. The range extent of the AFAIs is mainly indicative of the horizontal width of the modified E region along the radar line of sight, which is northeastward. The spatial structure of the AFAI backscatter will be examined in more detail later in the paper. The Doppler shifts are relatively small throughout the modified volume, and only the lowest frequency Doppler bins resulting from spectral analysis are

utilized in constructing this figure.

Close inspection shows that backscatter from AFAIs was detectable within the first 20 seconds of the heating cycle beginning at 2055 UT when X-mode heating was absent. This means that AFAIs could be generated using 11% of available O-mode subarray power or less, since 11% was the lowest power level in the schedule. In contrast, echoes could only be detected within the first 40 seconds of the cycle beginning at 2100 UT when X-mode heating was present, meaning that 20% of subarray power was required. These results typified the May 7 experiments, which did not include sufficiently low power levels to determine the threshold for AFAI generation when X-mode heating was absent but which did demonstrate that the power threshold level at least doubled when X-mode heating took place. At the end of all the heating cycles, irregularities could be sustained over broad spatial regions at the lowest power level, with and without X-mode heating. In no case did the echo power saturate, i.e., echo power always increased with increasing pump power.

Figure 7.2 shows comparable results obtained on May 8, 2012. Geomagnetic activity was already beginning to increase by this time. Here, as is often the case during geomagnetically active times, the Doppler shifts of the echoes were significant and also structured. Backscatter power levels and heating efficiency were also somewhat reduced due to increased background absorption. The associated loss in heating efficiency made it possible to determine the threshold for AFAI onset both with and without X-mode heating. In this example, AFAIs were detectable within the first 30 seconds of the heating cycle (beginning at 2140 UT) when X-mode heating was absent but just within the first 50 seconds of the cycle (beginning at 2135 UT) when X-mode heating was present. The corresponding subarray power

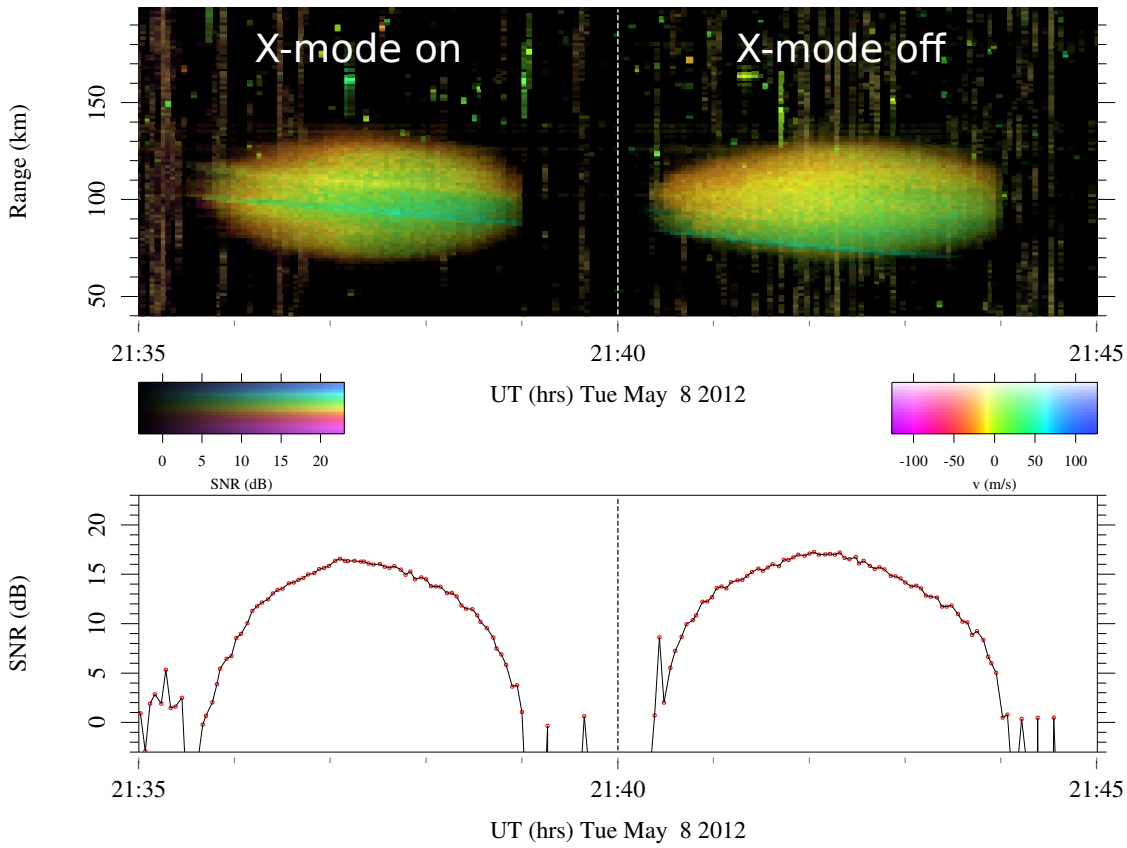

Figure 7.2: Range-time Doppler intensity (RTDI) plot of backscatter from artificial *E* region FAIs over HAARP observed on May 8, 2012. This example shows considerable fine structure in backscattered power and Doppler shift versus range and time. X-mode heating was present during only the first 5-min. heating cycle.

fractions required for AFAI generation were 15% and 25%, respectively, the ratio being somewhat less then a doubling.

Similar experiments except with a heating power schedule that included lower and more finely graduated O-mode power levels were performed during the week of August 5, 2012. The O-mode power levels still followed a quadratic progression, as shown in Table 1. The heater power increased for 2 minutes from zero to about 72% of the maximum available subarray power and then decreased for 2 minutes

back to zero. Figure 7.3 shows the echoes observed by the coherent scatter radar during these experiments. Irregularities were observed within 40 seconds for the heating cycle starting at 2220 UT, in the absence of X-mode emissions. This corresponds to about 14% of the maximum subarray power. For the cycle starting at 2215 UT, irregularities were first observed at 2226 UT, 60 seconds into the experiment. This corresponds to about 24.5% of the maximum subarray power. Like the May experiments, the heating power required to excite irregularities with X-mode emissions was slightly less than twice what was required without them.

In all cases we observed, the threshold power level for E region AFAI generation approximately doubled under X-mode heating with a HAARP subarray excited at full power. In the remainder of this paper, we examine the degree to which this finding is consistent with contemporary thermal parametric instability theory.

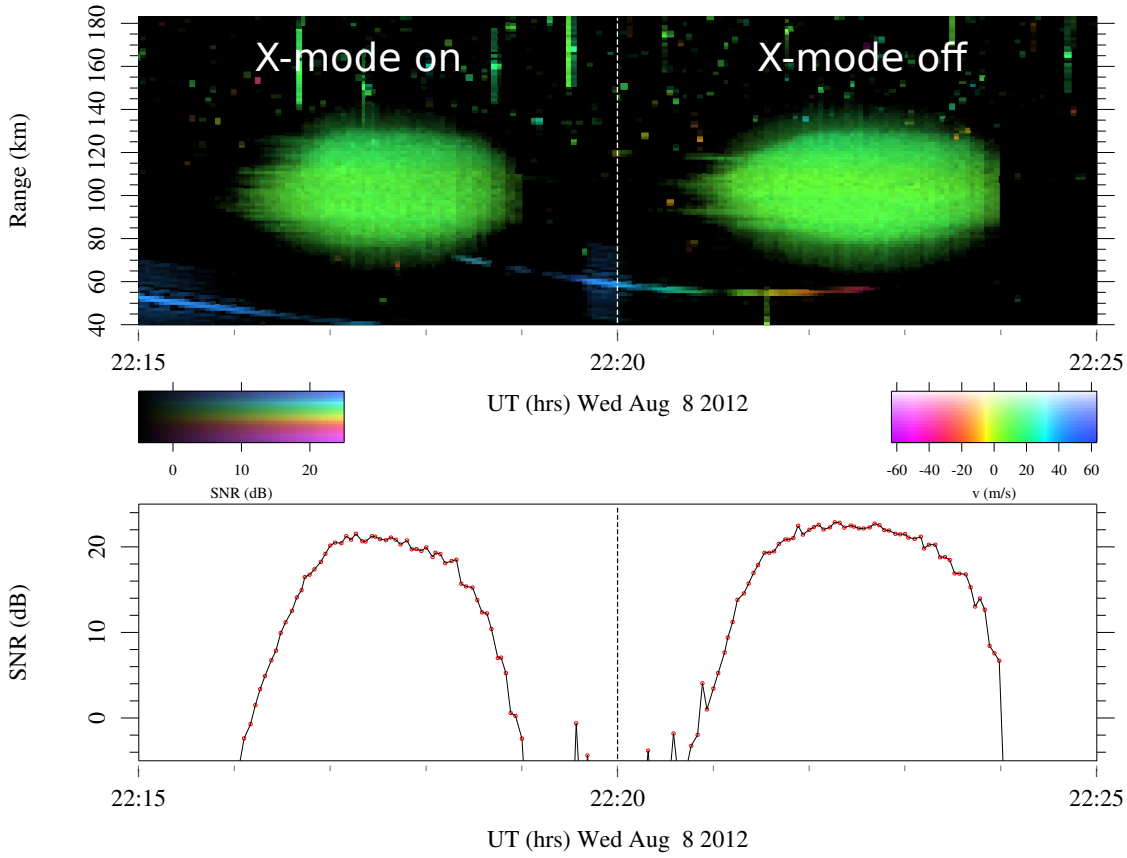

Figure 7.3: Range-time Doppler intensity (RTDI) plot of backscatter from artificial E region FAIs over HAARP observed on August 8, 2012. O-mode heating power steps were taken in smaller increments to better assess the power threshold. X-mode heating was present during only the first 5-min. heating cycle.

7.3 Analysis

According to *Dysthe et al.* [1983] (with adaptations from *Hysell et al.* [2010]), the threshold peak electric field for thermal parametric instability in the E region at high latitudes can be estimated from:

$$|E_{\rm th}|^2 = 2n_\circ\epsilon_\circ^{-1}K_B T_e\,(1 + T_i/T_e)\,\sqrt{\delta_e}k_4 l_c/L \tag{7.4}$$

where

$$\begin{aligned} l_c &= \sqrt{K_B T_e/m_e}\nu_{\rm en}^{-1} \\ \delta_e &= 4.8\times10^{-3}(185/T_e)^{3/2} \\ k_4 &= \cos\alpha/(ra\,\exp(-2k_p\delta L)) \\ \delta &= Z(1+Y^2)/(1-Y^2) \\ a &= (1+Y)^2/(1-Y) \end{aligned}$$

Here, $n_\circ$ is the background electron density, T_e and T_i are electron and ion temperatures, $\nu_{\rm en}$ is the electron-neutral collision frequency, l_c is the electron mean free path, L is the vertical plasma density scale length, k_p is the pump mode wavenumber at the upper-hybrid interaction height, and α is the zenith angle of the geomagnetic field. Also, $Y \equiv \Omega_e/\omega$, and $Z \equiv \nu_{en}/\omega$. The δ_e expression is the electron cooling rate due to inelastic collisions with neutrals, adapted from figures given by *Gurevich* [1978] and accurate for electron temperatures below about 400 K.

The term involving the factors $2k_p\delta L$ represents the effects of the finite vertical extent of the interaction region. The significance of this term and the inelastic cooling rate term for E region ionospheric modifications was highlighted by *Hysell et al.* [2010]. Finally, r is the effective reflection coefficient, the ratio of the incident

and reflected pump mode wave amplitudes at the interaction height. A pump-mode standing wave is crucial for breaking the symmetry that would otherwise prevent thermal parametric instability for a circularly polarized pump wave [*Das and Fejer*, 1979; *Dysthe et al.*, 1983]. The formulas above assume that the O-mode is purely circularly polarized; a different formulation is required for near-vertical incidence at middle and low latitudes.

Estimating the parameters for E region field aligned irregularities at 99 km over HAARP and taking $T_e = T_i = 209$ K, $L = 6$ km, and $\nu_{en} = 4{\times}10^4$ s^{-1} predicts (according to the aforementioned theory) a threshold electric field of approximately 190 mV/m in the absence of X-mode heating. This is consistent with our experimental results, taking into consideration magneto-ionic effects and nominal D region absorption, which we show how to estimate below. However, this estimate depends strongly on a number of parameters that are difficult to measure or estimate precisely, the vertical plasma gradient density scale length at the interaction height chief among them. A more accurate test of threshold theory can be performed by modifying ionospheric conditions in a limited, tractable way and then measuring the corresponding effect on the threshold for irregularity onset. This is the rationale for the present experiments.

The threshold theory exemplifies three possible mechanisms for X-mode affects on the efficiency of AFAI generation by O-mode heating. The first is the explicit dependence of the threshold electric field on temperature at the upper hybrid interaction height. The second is X-mode enhanced D region absorption caused by X-mode heating. The third is the change in the effective reflection coefficient that also occurs when absorption near the interaction height increases. Some of these mechanisms can be measured experimentally. For example *Langston and Moore*

[2013] measure D region absorption caused by X-mode heating. Quantifying the combined affects of these mechanisms, however, requires numerical modeling.

7.3.1 Artificial heating model

In order to evaluate and rank the possible influences on and temperature dependencies of AFAI generation efficiency, we have modified the SAMI2 model described in *Huba et al.* [2000] and Section 3.3.1. These modifications include 1) simple D region chemistry 2) a high resolution grid at low altitudes and 3) a pump mode solver to examine how X- and O-mode waves would propagate under specific conditions generated by SAMI2. Results from the modified model are then analyzed in the second part of this section.

Modifications to SAMI2

By default, SAMI2 incorporates seven ion species (H^+, He^+, N^+, O^+, N_2^+, NO^+, and O_2^+), coupled through a system of 21 chemical reactions plus recombination reactions. This system is sufficient for E and F region simulations but lacks negative ions important in the D region. In particular, *Enell et al.* [2005] have shown how increasing the D region electron temperature during ionospheric modification experiments increases the electron attachment rate and the ratio of negative ions to electrons, a process with implications for the overall absorption rate (see also *Rodriguez and Inan* [1994]). We have consequently augmented SAMI2 with the introduction of some simplified negative ion chemistry.

Following the prescription of *Rodriguez and Inan* [1994], we have added provisions for a negative ions and positive cluster ions. The production and loss of these

species in this prescription are adapted from the simplified set of rate equations given in the reference. Most importantly, the electron attachment rate leading to the production of negative ions is temperature dependent. We neglect transport for the new species and regard them as being locally produced and consumed.

Another modification made to SAMI2 was to add a nested fine grid at D and E region altitudes. The grid places 3000 points between 50–110 km altitude. This is sufficient for resolving the Airy pattern of the pump mode.

The final modification was the addition of a pump-mode solver. The solver was based on the work of *Thid and Lundborg* [1986] and permits the calculation of the X- and O-mode pump waves based on SAMI2 model parameters (electron density, temperature, gyrofrequency, electron-neutral collision frequency, and magnetic field) at every time step. Electron-neutral collision frequencies were calculated using formulas given by *Schunk and Nagy* [2004] and were adjusted to account for a velocity-dependent collision frequency using the formulation given by *Sen and Wyller* [1960]. The heating rate, estimated from the magneto-ionic solver and reintroduced to the SAMI2 heat transport model, is given by

$$q(z) = \Im(n)\frac{2\omega I}{c} \tag{7.5}$$

where n, ω, and I refer to the X-mode index of refraction, frequency, and intensity (Poynting flux), respectively.

Model results

The profiles in Figure 7.4 show diagnostic parameters for the case of negligible X- and O-mode power emissions. The left-hand panel shows background electron temperature and density profiles as calculated by the modified SAMI2 model. The

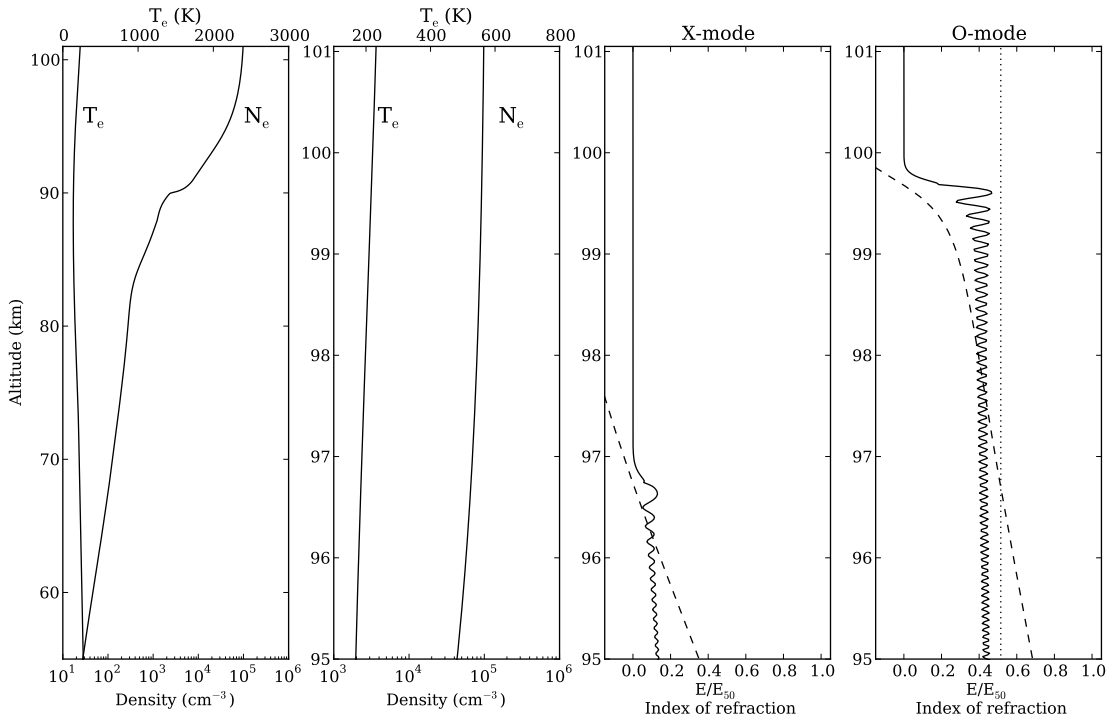

Figure 7.4: Figure showing X- and O-mode wave envelopes for a hypothetical experiment using low power emissions. From left to right: (1) Electron temperature and density. (2) Detailed view of electron temperature and density near the upper hybrid interaction height. (3) X-mode wave envelope (solid) and the index of refraction (dashed). (4) O-mode wave envelope (solid), index of refraction (dashed), and the index of refraction corresponding to upper hybrid resonance (dotted-dashed).

center and right panels show the amplitude envelopes (solid lines) (relative to their amplitudes at 50 km altitude) and the index of refraction (dashed lines) of the X- and O-mode waves, respectively. Additionally, the right-hand panel shows a third curve (dotted-dashed line) representing the value of the index of refraction for the O-mode wave corresponding to upper hybrid resonance. The interaction height is where this curve intercepts the actual O-mode index of refraction.

Figure 7.5 shows similar information, this time for the case of X-mode emissions

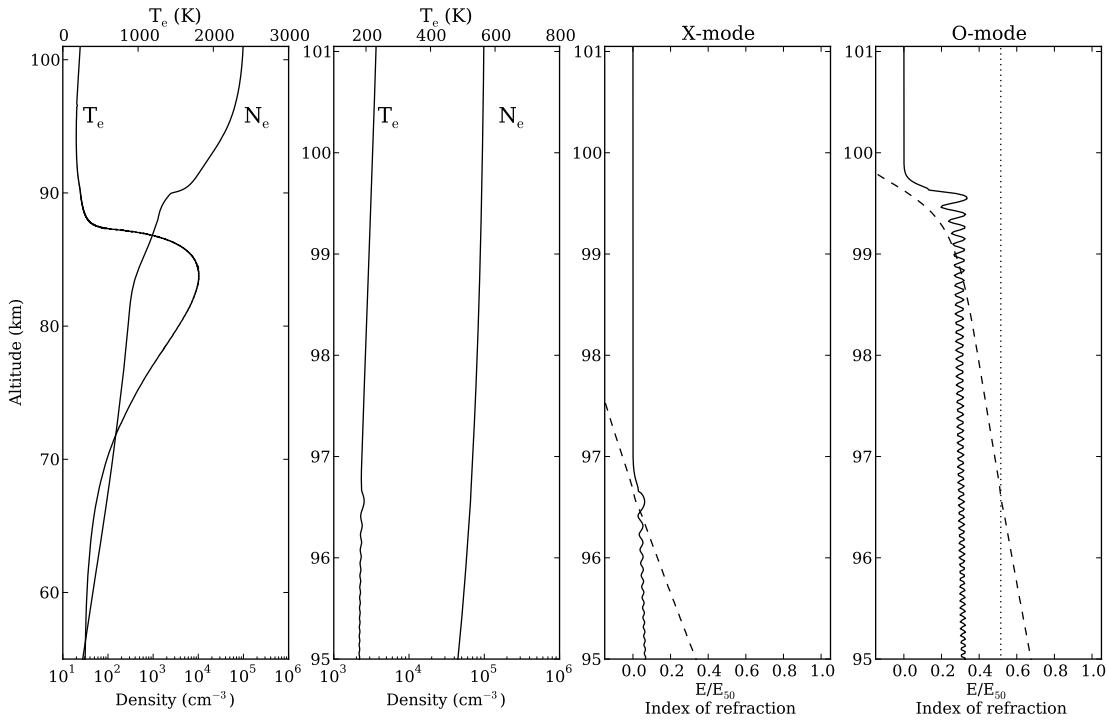

Figure 7.5: Same as Figure 7.4, only with full subarray X-mode heating.

at full subarray power. (Since we are considering the threshold condition, the O-mode power is regarded as being too small itself to modify the ionosphere.) Comparing with the profiles in Figure 7.4 shows that the O-mode pump power reaching the upper-hybrid interaction height has decreased significantly. This is due to the heater-induced absorption between about 70 and 88 km altitude. The O-mode wave amplitude reaching the interaction height with X-mode heating is about 75% what it is in the absence of heating. The power lost to absorption is consequently a little under half.

The fraction of X-mode pump power reaching the interaction height is also greatly reduced. Consequently, the heating taking place at this altitude is modest. This can be seen more clearly in the second panel of Figure 7.5, which provides

more detailed state parameter profiles near the interaction height. The temperature increase due to direct heating here is only about 10 K. While small, this increase was enough to shift the X-mode reflection height downward by about 60 m, making it fall slightly below the upper-hybrid interaction height. This is an unanticipated complication, likely rendering the direct heating effect experimentally undetectable. Finally, direct heating near and above the upper-hybrid interaction height can be seen to be insufficient to alter the effective O-mode reflection coefficient. The modeling consequently indicates that the only important effect of X-mode emission is to increase the absorption of the O-mode signal below the interaction height.

7.4 Summary and conclusions

The HAARP experiments were originally designed to test the theory of the threshold pump power required for thermal parametric instability and its dependence on electron temperature at the upper-hybrid interaction height in particular. One long-term goal of the investigation is the ability to measure electron temperatures and temperature profiles using heating in an altitude regime that is difficult to investigate with conventional remote sensing approaches. However, the modified SAMI2 model indicates that the main effect of X-mode heating in our experiments was to increase D region absorption, with very little X-mode power propagating to or being deposited at the upper-hybrid interaction height. This means that the aspect of the theory regarding the threshold dependence on temperature remains unvalidated. In order to compensate for the unanticipated experimental effects we encountered, the experiment could be modified to be run at higher X- and O-mode mode frequencies to reduce the amount of absorption. Relatively low E region den-

sities restrict the range of frequencies available severely, however. Additionally, the experiment could be improved by varying the X- and O-mode frequency offset so as to make the heating near the X-mode reflection height coincide more closely with the upper-hybrid interaction height.

The experimental methodology described here could also be modified and used as a powerful diagnostic of D region absorption. Our model predicts D region O-mode absorption as a function of X-mode pump power level, and our threshold power measurement can validate the prediction. The accuracy of the prediction rests upon the accuracy of the underlying D region photochemistry model and on the heater-induced variations in the electron density profile it predicts. Precise absorption measurements for a variety of X-mode pump power levels would give incisive diagnostic information and permit precise photochemical model tuning and refinement.

CHAPTER 8

CONCLUSIONS AND SUGGESTIONS FOR FURTHER RESEARCH

This thesis presented radar-based experiments that were performed to study both natural and artificial field aligned irregularities. The natural irregularities were generated by the Farley Buneman instability. Previous auroral E region experiments and theory for Farley Buneman waves were reviewed in the first few chapters. The 2-D SAMI2 ionospheric model was extended to include the local, heuristic Farley Buneman wave model proposed by *Milikh and Dimant* [2002]. The model predicted profiles of wave phase velocity, aspect width, and the associated electron and ion heating caused by the waves. These profiles were generated for convection speeds ranging from 400 to 1000 m/s. The Farley Buneman wave model was shown to accurately reproduce known characteristics of the waves. Electron temperature profiles from the PFISR were compared with the modeled curves and validated that the model was producing sensible results that were observable in nature. Furthermore, spectral moments from the 30 MHz Homer coherent scatter radar were compared with kernel-averaged phase velocities along with measurements from the PFISR within overlapping volumes. The dissimilar spatial and temporal resolutions of the coherent and incoherent scatter radars made it challenging to find data that made sense to compare. The flow angle, θ, was estimated from the relationship, $v_p = \langle C_s \rangle \cos\theta$, and this estimate agreed with the line of sight drifts measured by the PFISR.

Homer radar Doppler spectra were inverted using a forward model to estimate the convection speed and pattern within the radar's field of view. The forward model was based on empirical formulas that related the Doppler velocity and spectral width to the convection speed. Equipotential contours of the convec-

tion pattern were then constructed from the convection speed estimates by using a nonlinear least squares solver that minimized the sum of the model predicted error and the nonuniformity of the potential curves. The velocity estimates were shown to have small residuals considering the regularization constraints. This suggests that the velocity estimates represent an incompressible flow.

Lastly, the Homer radar was used to study the effects of X-mode suppression for artificial heating experiments conducted at HAARP. The artificial field aligned irregularities required approximately twice the power to form while being actively suppressed by the X-mode pump wave. Modelling efforts of this experiment revealed that the X-mode wave power mainly increased D region absorption and did not effect electron temperatures at the upper hybrid interaction height.

8.1 Suggestions for further research

The work performed in this thesis provided some insight into the physics behind natural and artificial field aligned irregularities. We suggest several experiments that could be used to enhance this understanding and to provide further validation of the principles and techniques.

8.1.1 Comparison with vector electric fields estimated from incoherent scatter radar observations

Incoherent scatter radar measurements can also be used to estimate the vector electric fields with high resolution in a region that covers about 4 degrees in magnetic latitude and 8 degrees in magnetic longitude [*Nicolls et al.*, 2014]. The radar

measures a component of the convection velocity in the direction perpendicular to the beam. Therefore, to image the vector electric field, an inversion of the LOS velocity measurements can be performed. *Nicolls et al.* [2014] invert the data with the Lagrange method of undetermined multipliers to regularize the underdetermined problem. These detailed maps can be used to verify the convection map estimates from the Homer coherent scatter radar.

The spatial and temporal resolution of the maps derived from the incoherent scatter radar measurements is reduced compared with the resolution of the Homer radar. As a result, a period of constant convection for several minutes would be required to effectively compare the data between the two instruments. Once the inversion techniques used by the Homer radar are validated, the measurements can be used to look at more interesting periods of auroral activity.

8.1.2 Multi-frequency radar experiments

With information from multiple frequencies, it would be possible to construct a k spectrum from the data at each frequency. In order to perform a reasonable analysis of the data, the observation geometry of each radar needs to be considered in addition to the different observation frequencies. If the radars were configured in a multi-static configuration, accounting for the geometry would be less complicated, however, such experiments are still difficult to perform. One example of this type of experiment was performed in the F region over the Platteville heater using radars at White Sands and other sites [*Franz et al.*, 1999].

8.1.3 Simultaneous sounding rocket experiment

With a rocket payload equipped with electric field probes, it would be possible to associate the in-situ electric field measurements with coherent scatter radar Doppler spectra within the same volume. These electric fields can also be used to validate the convection pattern estimates discussed in Chapter 6. Recent experiments performed by *Pfaff et al.* [1992]; *Bahcivan et al.* [2005]; *Hysell et al.* [2008a] all discuss simultaneous radar and sounding rocket experiments.

BIBLIOGRAPHY

Aster, R., C. Thurber, and B. Borchers (2005), *Parameter Estimation and Inverse Problems*, no. v. 1 in International geophysics series, Elsevier Academic Press.

Bahcivan, H., D. L. Hysell, M. F. Larsen, and R. F. Pfaff (2005), The 30 MHz imaging radar observations of auroral irregularities during the JOULE campaign, *Journal of Geophysical Research: Space Physics*, *110*(A5), n/a–n/a, doi: 10.1029/2004JA010975.

Bahnsen, A., E. Ungstrup, C. G. Flthammar, U. Fahleson, J. K. Olesen, F. Primdahl, F. Spangslev, and A. Pedersen (1978), Electrostatic waves observed in an unstable polar cap ionosphere, *Journal of Geophysical Research: Space Physics*, *83*(A11), 5191–5197, doi:10.1029/JA083iA11p05191.

Balsley, B. B., and D. T. Farley (1971), Radar studies of the equatorial electrojet at three frequencies, *Journal of Geophysical Research*, *76*(34), 8341–8351, doi: 10.1029/JA076i034p08341.

Bellan, P. M. (2006), *Fundamentals of Plasma Physics*, Cambridge University Press.

Booker, H. G. (1956), A theory of scattering by nonisotropic irregularities with application to radar reflections from the aurora, *Journal of Atmospheric and Terrestrial Physics*, *8*(45), 204–221, doi:10.1016/0021-9169(56)90126-X.

Bowles, K. L. (1954), Doppler shifted radio echoes from aurora, *Journal of Geophysical Research*, *59*(4), 553–555, doi:10.1029/JZ059i004p00553.

Bowles, K. L. (1958), Observation of vertical-incidence scatter from the ionosphere at 41 Mc/sec, *Physical Review Letters*, *1*(12), 454–455, doi:10.1103/ PhysRevLett.1.454.

Bowles, K. L., R. Cohen, G. R. Ochs, and B. B. Balsley (1960), Radio echoes from field-aligned ionization above the magnetic equator and their resemblance to auroral echoes, *Journal of Geophysical Research*, *65*(6), 1853–1855, doi:10.1029/JZ065i006p01853.

Bowles, K. L., B. B. Balsley, and R. Cohen (1963), Field-aligned E-region irregularities identified with acoustic plasma waves, *Journal of Geophysical Research*, *68*(9), 2485–2501, doi:10.1029/JZ068i009p02485.

Bristow, W. (2008), Statistics of velocity fluctuations observed by SuperDARN under steady interplanetary magnetic field conditions, *Journal of Geophysical Research: Space Physics*, *113*(A11), A11,202, doi:10.1029/2008JA013203.

Bullough, K., and T. R. Kaiser (1954), Radio reflections from aurorae, *Journal of Atmospheric and Terrestrial Physics*, *5*(16), 189–200, doi:10.1016/0021-9169(54)90035-5.

Buneman, O. (1963), Excitation of field aligned sound waves by electron streams, *Physical Review Letters*, *10*(7), 285–287, doi:10.1103/PhysRevLett.10.285.

Coster, A. J., F. T. Djuth, R. J. Jost, and W. E. Gordon (1985), The temporal evolution of 3-m striations in the modified ionosphere, *Journal of Geophysical Research: Space Physics*, *90*(A3), 2807–2818, doi:10.1029/JA090iA03p02807.

Das, A., and J. Fejer (1979), Resonance instability of small-scale field-aligned irregularities, *Journal of Geophysical Research: Space Physics*, *84*(A11), 6701–6704, doi:10.1029/JA084iA11p06701.

Dimant, Y. S., and G. M. Milikh (2003), Model of anomalous electron heating in the E region: 1. basic theory, *Journal of Geophysical Research: Space Physics*, *108*(A9), n/a–n/a, doi:10.1029/2002JA009524.

Djuth, F. T., et al. (1985), Observations of E region irregularities generated at auroral latitudes by a high-power radio wave, *Journal of Geophysical Research: Space Physics*, *90*(A12), 12,293–12,306, doi:10.1029/JA090iA12p12293.

Dougherty, J. P. (1963), The conductivity of a partially ionized gas in alternating electric fields, *Journal of Fluid Mechanics*, *16*(01), 126–137, doi:10.1017/S002211206300063X.

Dougherty, J. P., and D. T. Farley (1960), A theory of incoherent scattering of radio waves by a plasma, *Proceedings of the Royal Society of London. Series A. Mathematical and Physical Sciences*, *259*(1296), 79–99, doi:10.1098/rspa.1960.0212.

Dougherty, J. P., and D. T. Farley (1963), A theory of incoherent scattering of radio waves by a plasma: 3. Scattering in a partly ionized gas, *Journal of Geophysical Research*, *68*(19), 5473–5486, doi:10.1029/JZ068i019p05473.

Dougherty, J. P., and D. T. Farley (1967), Ionospheric E-region irregularities produced by nonlinear coupling of unstable plasma waves, *Journal of Geophysical Research*, *72*(3), 895–901, doi:10.1029/JZ072i003p00895.

Dysthe, K. B., E. Mjlhus, H. Pcseli, and K. Rypdal (1982), Thermal cavitons, *Physica Scripta*, *1982*(T2B), 548.

Dysthe, K. B., E. Mjolhus, K. Rypdal, and H. L. Pecseli (1983), A thermal oscillating two-stream instability, *Physics of Fluids*, *26*, 146–157, doi:10.1063/1.863993.

Eckersley, T. L. (1937), Irregular ionic clouds in the E layer of the ionosphere, *Nature*, *140*(3550), 846–847, doi:10.1038/140846a0.

Enell, C.-F., A. Kero, E. Turunen, T. Ulich, P. T. Verronen, A. Seppälä, S. Marple, F. Honary, and A. Senior (2005), Effects of D-region RF heating studied with

the Sodankylä Ion Chemistry model, *Annales Geophysicae*, *23*(5), 1575–1583, doi:10.5194/angeo-23-1575-2005.

Farley, D., and J. Providakes (1989), The variation with Te and Ti of the velocity of unstable ionospheric two-stream waves, *Journal of Geophysical Research: Space Physics*, *94*(A11), 15,415–15,420, doi:10.1029/JA094iA11p15415.

Farley, D. T. (1963), A plasma instability resulting in field-aligned irregularities in the ionosphere, *Journal of Geophysical Research*, *68*(22), 6083–6097, doi:10.1029/JZ068i022p06083.

Farley, D. T. (1966), A theory of incoherent scattering of radio waves by a plasma: 4. The effect of unequal ion and electron temperatures, *Journal of Geophysical Research*, *71*(17), 4091–4098, doi:10.1029/JZ071i017p04091.

Farley, D. T. (1972), Multiple-pulse incoherent scatter correlation function measurements, *Radio Science*, *7*(6), 661–666, doi:10.1029/RS007i006p00661.

Farley, D. T. (1985), Theory of equatorial electrojet plasma waves: new developments and current status, *Journal of Atmospheric and Terrestrial Physics*, *47*(810), 729–744, doi:10.1016/0021-9169(85)90050-9.

Farley, D. T., J. P. Dougherty, and D. W. Barron (1961), A theory of incoherent scattering of radio waves by a plasma 2. Scattering in a magnetic field, *Proceedings of the Royal Society of London. Series A. Mathematical and Physical Sciences*, *263*(1313), 238–258, doi:10.1098/rspa.1961.0158.

Fejer, B. G., and M. C. Kelley (1980), Ionospheric irregularities, *Reviews of Geophysics*, *18*(2), 401–454, doi:10.1029/RG018i002p00401.

Fejer, J. A. (1960a), Scattering of radio waves by an ionized gas in thermal equilibrium, *Canadian Journal of Physics*, *38*(8), 1114–1133, doi:10.1139/p60-119.

Fejer, J. A. (1960b), Radio-wave scattering by an ionized gas in thermal equilibrium, *Journal of Geophysical Research*, *65*(9), 2635–2636, doi:10.1029/JZ065i009p02635.

Fejer, J. A. (1961), Scattering of radio waves by an ionized gas in thermal equilibrium in the presence of a uniform magnetic field, *Canadian Journal of Physics*, *39*(5), 716–740, doi:10.1139/p61-081.

Fejer, J. A. (1979), Ionospheric modification and parametric instabilities, *Reviews of Geophysics*, *17*(1), 135–153, doi:10.1029/RG017i001p00135.

Flood, W. A. (1960), Simultaneous VHF auroral backscatter measurements, *Journal of Geophysical Research*, *65*(8), 2261–2268, doi:10.1029/JZ065i008p02261.

Franz, T. L., M. C. Kelley, and A. V. Gurevich (1999), Radar backscattering from artificial field-aligned irregularities, *Radio Science*, *34*(2), 465–475, doi:10.1029/1998RS900035.

Fried, B. D., and S. D. Conte (1961), *The Plasma Dispersion Function*, Academic Press.

Frolov, V., L. Erukhimov, S. Metelev, and E. Sergeev (1997), Temporal behaviour of artificial small-scale ionospheric irregularities: Review of experimental results, *Journal of Atmospheric and Solar-Terrestrial Physics*, *59*(18), 2317 – 2333, doi:http://dx.doi.org/10.1016/S1364-6826(96)00126-5, artificial Modification of the Ionosphere.

Frolov, V. L., L. M. Kagan, E. N. Sergeev, G. P. Komrakov, P. A. Bernhardt, J. A. Goldstein, L. S. Wagner, C. A. Selcher, and P. Stubbe (1999), Ionospheric observations of F region artificial plasma turbulence, modified by powerful X-

mode radio waves, *Journal of Geophysical Research: Space Physics*, *104*(A6), 12,695–12,704, doi:10.1029/1998JA900182.

Gordon, W. (1958), Incoherent scattering of radio waves by free electrons with applications to space exploration by radar, *Proceedings of the IRE*, *46*(11), 1824–1829, doi:10.1109/JRPROC.1958.286852.

Grach, S., N. Mityakov, V. Rapoport, and V. Trakhtengertz (1981), Thermal parametric turbulence in a plasma, *Physica D: Nonlinear Phenomena*, *2*(1), 102 – 106, doi:http://dx.doi.org/10.1016/0167-2789(81)90063-4.

Grach, S. M., A. N. Karashtin, N. A. Mitiakov, V. O. Rapoport, and V. I. Trakhtengerts (1978), Theory of the thermal parametric instability in an inhomogeneous plasma, *Fizika Plazmy*, *4*, 1321–1329.

Gray, R. W., and D. T. Farley (1973), Theory of incoherent-scatter measurements using compressed pulses, *Radio Science*, *8*(2), 123–131, doi:10.1029/RS008i002p00123.

Greenwald, R. (1996), The role of coherent radars in ionospheric and magnetospheric research, *Modern Ionospheric Science*, pp. 391–414.

Greenwald, R. A. (1974), Diffuse radar aurora and the gradient drift instability, *Journal of Geophysical Research*, *79*(31), 4807–4810, doi:10.1029/JA079i031p04807.

Greenwald, R. A., and W. L. Ecklund (1975), A new look at radar auroral motions, *Journal of Geophysical Research*, *80*(25), 3642–3648, doi:10.1029/JA080i025p03642.

Greenwald, R. A., W. L. Ecklund, and B. B. Balsley (1973), Auroral currents,

irregularities, and luminosity, *Journal of Geophysical Research*, *78*(34), 8193–8203, doi:10.1029/JA078i034p08193.

Greenwald, R. A., et al. (1995), DARN/SuperDARN, *Space Science Reviews*, *71*(1-4), 761–796, doi:10.1007/BF00751350.

Gurevich, A. (1978), *Nonlinear phenomena in the ionosphere*, Physics and chemistry in space, Springer Verlag.

Gurevich, A. V. (2007), Nonlinear effects in the ionosphere, *Physics-Uspekhi*, *50*(11), 1091–1121, doi:10.1070/PU2007v050n11ABEH006212.

Gustavsson, B., R. Newsome, T. B. Leyser, M. J. Kosch, L. Norin, M. McCarrick, T. Pedersen, and B. J. Watkins (2009), First observations of X-mode suppression of O-mode HF enhancements at 6300 Å, *Geophysical Research Letters*, *36*(20), n/a–n/a, doi:10.1029/2009GL039421.

Hagfors, T. (1961), Density fluctuations in a plasma in a magnetic field, with applications to the ionosphere, *Journal of Geophysical Research*, *66*(6), 1699–1712, doi:10.1029/JZ066i006p01699.

Haldoupis, C., and K. Schlegel (1990), Direct comparison of 1-m irregularity phase velocities and ion acoustic speeds in the auroral E region ionosphere, *Journal of Geophysical Research: Space Physics*, *95*(A11), 18,989–19,000, doi:10.1029/JA095iA11p18989.

Hanuise, C. (1983), High-latitude ionospheric irregularities: A review of recent radar results, *Radio Science*, *18*(6), 1093–1121, doi:10.1029/RS018i006p01093.

Harang, L., and B. Landmark (1954), Radio echoes observed during aurorae and geomagnetic storms using 35 and 74mc/s waves simultaneously, *Journal of At-*

mospheric and Terrestrial Physics, *4*(6), 322–IN7, doi:10.1016/0021-9169(54)90063-X.

Harang, L., and W. Stoffregen (1938), Scattered reflections of radio waves from a height of more than 1,000 km, *Nature*, *142*, 832, doi:10.1038/142832a0.

Hedin, A. E., et al. (1991), Revised global model of thermosphere winds using satellite and ground-based observations, *Journal of Geophysical Research: Space Physics*, *96*(A5), 7657–7688, doi:10.1029/91JA00251.

Holt, J. M., D. A. Rhoda, D. Tetenbaum, and A. P. van Eyken (1992), Optimal analysis of incoherent scatter radar data, *Radio Science*, *27*(3), 435–447, doi:10.1029/91RS02922.

Holtet, J. A. (1973), Electric field microstructures in the auroral E region, *Tech. rep.*, Norske Institutt for Kosmisk Fysikk, Oslo.

Huba, J. D., G. Joyce, and J. A. Fedder (2000), SAMI2 is another model of the ionosphere (SAMI2): A new low-latitude ionosphere model, *Journal of Geophysical Research: Space Physics*, *105*(A10), 23,035–23,053, doi:10.1029/2000JA000035.

Huba, J. D., K. F. Dymond, G. Joyce, S. A. Budzien, S. E. Thonnard, J. A. Fedder, and R. P. McCoy (2002), Comparison of O+ density from ARGOS LORAAS data analysis and SAMI2 model results, *Geophysical Research Letters*, *29*(7), 6–1–6–4, doi:10.1029/2001GL013089.

Huba, J. D., G. Joyce, and J. A. Fedder (2003), Simulation study of mid-latitude ionosphere fluctuations observed at Millstone Hill, *Geophysical Research Letters*, *30*(18), n/a–n/a, doi:10.1029/2003GL018018.

Hughes, J. M., W. A. Bristow, R. T. Parris, and E. Lundell (2003), SuperDARN

observations of ionospheric heater-induced upper hybrid waves, *Geophysical Research Letters*, *30*(24), n/a–n/a, doi:10.1029/2003GL018772.

Hysell, D. L., and J. L. Chau (2006), Optimal aperture synthesis radar imaging, *Radio Science*, *41*(2), n/a–n/a, doi:10.1029/2005RS003383.

Hysell, D. L., J. Drexler, E. B. Shume, J. L. Chau, D. E. Scipion, M. Vlasov, R. Cuevas, and C. Heinselman (2007), Combined radar observations of equatorial electrojet irregularities at Jicamarca, *Ann. Geophys.*, *25*(2), 457–473, doi:10.5194/angeo-25-457-2007.

Hysell, D. L., G. Michhue, M. F. Larsen, R. Pfaff, M. Nicolls, C. Heinselman, and H. Bahcivan (2008a), Imaging radar observations of Farley Buneman waves during the JOULE II experiment, *Ann. Geophys.*, *26*(7), 1837–1850, doi:10.5194/angeo-26-1837-2008.

Hysell, D. L., F. S. Rodrigues, J. L. Chau, and J. D. Huba (2008b), Full profile incoherent scatter analysis at Jicamarca, *Annales Geophysicae*, *26*, 59–75, doi:10.5194/angeo-26-59-2008.

Hysell, D. L., G. Michhue, M. J. Nicolls, C. J. Heinselman, and M. F. Larsen (2009), Assessing auroral electric field variance with coherent and incoherent scatter radar, *Journal of Atmospheric and Solar-Terrestrial Physics*, *71*, 697–707, doi:10.1016/j.jastp.2008.10.013.

Hysell, D. L., E. Nossa, and M. McCarrick (2010), Excitation threshold and gyroharmonic suppression of artificial E region field-aligned plasma density irregularities, *Radio Science*, *45*(6), n/a–n/a, doi:10.1029/2010RS004360.

Hysell, D. L., E. Nossa, and M. McCarrick (2011), X-mode suppression of artificial

E region field-aligned plasma density irregularities, *Radio Science*, *46*(2), n/a–n/a, doi:10.1029/2010RS004551.

Hysell, D. L., R. J. Miceli, and J. D. Huba (2013), Implications of a heuristic model of auroral Farley Buneman waves and heating, *Radio Science*, *48*(5), 527–534, doi:10.1002/rds.20061.

Hysell, D. L., H. C. Aveiro, and J. L. Chau (2014), Ionospheric Irregularities, in *Modeling the IonosphereThermosphere System*, edited by J. Huba, R. Schunk, and G. Khazanov, pp. 217–240, John Wiley & Sons, Ltd.

Igarashi, K., and K. Schlegel (1987), Electron temperature enhancements in the polar E-region measured with EISCAT, *Journal of Atmospheric and Terrestrial Physics*, *49*(3), 273–280, doi:10.1016/0021-9169(87)90062-6.

Inhester, B., A. C. Das, and J. A. Fejer (1981), Generation of small-scale field-aligned irregularities in ionospheric heating experiments, *Journal of Geophysical Research: Space Physics*, *86*(A11), 9101–9106, doi:10.1029/JA086iA11p09101.

Janhunen, P. (1994), Perpendicular particle simulation of the E region Farley-Buneman instability, *Journal of Geophysical Research: Space Physics*, *99*(A6), 11,461–11,473, doi:10.1029/94JA00206.

Johnson, C. Y. (1969), Ion and neutral composition of the ionosphere., *Annals of the IQSY*, *5*, 197–213.

Kagan, L. M., R. S. Kissack, M. C. Kelley, and R. Cuevas (2008), Unexpected rapid decrease in phase velocity of submeter Farley-Buneman waves with altitude, *Geophysical Research Letters*, *35*(3), L03,106, doi:10.1029/2007GL032459.

Kelley, M. C. (2009), *The Earth's Ionosphere: Plasma Physics & Electrodynamics*, Academic Press.

Kelley, M. C., and F. S. Mozer (1973), Electric field and plasma density oscillations due to the high-frequency Hall current two-stream instability in the auroral E region, *Journal of Geophysical Research*, *78*(13), 2214–2221, doi:10.1029/JA078i013p02214.

Kelley, M. C., T. L. Arce, J. Salowey, M. Sulzer, W. T. Armstrong, M. Carter, and L. Duncan (1995), Density depletions at the 10-m scale induced by the Arecibo heater, *Journal of Geophysical Research: Space Physics*, *100*(A9), 17,367–17,376, doi:10.1029/95JA00063.

Kelley, M. C., R. A. Cuevas, and D. L. Hysell (2008), Radar scatter from equatorial electrojet waves: An explanation for the constancy of the Type I Doppler shift with zenith angle, *Geophysical Research Letters*, *35*(4), L04,106, doi:10.1029/2007GL032848.

Kissack, R. S., J.-P. St.-Maurice, and D. R. Moorcroft (1997), The effect of electron-neutral energy exchange on the fluid Farley-Buneman instability threshold, *Journal of Geophysical Research: Space Physics*, *102*(A11), 24,091–24,115, doi:10.1029/97JA02036.

Kuo, S., and M. Lee (1982), On the parametric excitation of plasma modes at upper hybrid resonance, *Physics Letters A*, *91*(9), 444 – 446, doi:http://dx.doi.org/10.1016/0375-9601(82)90745-9.

Langston, J., and R. C. Moore (2013), High time resolution observations of HF cross-modulation within the D region ionosphere, *Geophysical Research Letters*, *40*(10), 1912–1916, doi:10.1002/grl.50391.

Leadabrand, R. L., J. C. Schlobohm, and M. J. Baron (1965), Simultaneous very high frequency and ultra high frequency observations of the aurora at

Fraserburgh, Scotland, *Journal of Geophysical Research*, *70*(17), 4235–4284, doi:10.1029/JZ070i017p04235.

Lee, K., C. F. Kennel, and J. M. Kindel (1971), High-frequency Hall current instability, *Radio Science*, *6*(2), 209–213, doi:10.1029/RS006i002p00209.

Lee, M. C., and S. P. Kuo (1983), Excitation of upper-hybrid waves by a thermal parametric instability, *Journal of Plasma Physics*, *30*, 463–478, doi:10.1017/S002237780000129X.

Lehtinen, M. S. (1986), Statistical theory of incoherent scatter radar measurements, *Tech. Rep. 86/45*, EISCAT Scientific Association, Kiruna, Sweden.

Lehtinen, M. S., and I. Hggstrm (1987), A new modulation principle for incoherent scatter measurements, *Radio Science*, *22*(4), 625–634, doi:10.1029/RS022i004p00625.

Lehtinen, M. S., A. Huuskonen, and J. Pirttil (1996), First experiences of full-profile analysis with GUISDAP, *Annales Geophysicae*, *14*(12), 1487–1495, doi:10.1007/s00585-996-1487-3.

Lovell, A. C. B., J. A. Clegg, and C. D. Ellyett (1947), Radio echoes from the Aurora Borealis, *Nature*, *160*, 372, doi:10.1038/160372a0.

Machida, S., and C. K. Goertz (1988), Computer simulation of the Farley-Buneman instability and anomalous electron heating in the auroral ionosphere, *Journal of Geophysical Research: Space Physics*, *93*(A9), 9993–10,000, doi:10.1029/JA093iA09p09993.

Makarevich, R. A. (2008), HF radar observations of high-velocity E region echoes from the eastward auroral electrojet, *Journal of Geophysical Research: Space Physics*, *113*(A9), A09,321, doi:10.1029/2008JA013204.

McNamara, A. G. (1955), Double-doppler radar investigations of aurora, *Journal of Geophysical Research*, *60*(3), 257–269, doi:10.1029/JZ060i003p00257.

Miceli, R. J., D. L. Hysell, J. Munk, M. McCarrick, and J. D. Huba (2013), Reexamining X-mode suppression and fine structure in artificial E region field-aligned plasma density irregularities, *Radio Science*, *48*(5), 482–490, doi: 10.1002/rds.20054.

Michhue Vela, G. P. (2010), Electron heating by Farley-Buneman waves at polar latitudes, Ph.D. thesis, Cornell University.

Milikh, G. M., and Y. S. Dimant (2002), Kinetic model of electron heating by turbulent electric field in the E region, *Geophysical Research Letters*, *29*(12), 16–1, doi:10.1029/2001GL013935.

Milikh, G. M., and Y. S. Dimant (2003), Model of anomalous electron heating in the E region: 2. detailed numerical modeling, *Journal of Geophysical Research: Space Physics*, *108*(A9), n/a–n/a, doi:10.1029/2002JA009527.

Milikh, G. M., et al. (2001), Modeling ionospheric absorption modified by anomalous heating during substorms, *Geophysical Research Letters*, *28*(3), 487–490, doi:10.1029/2000GL003823.

Mjlhus, E. (1990), On linear conversion in a magnetized plasma, *Radio Science*, *25*(6), 1321–1339, doi:10.1029/RS025i006p01321.

Mjlhus, E. (1993), On the small scale striation effect in ionospheric radio modification experiments near harmonics of the electron gyro frequency, *Journal of Atmospheric and Terrestrial Physics*, *55*(6), 907 – 918, doi:http://dx.doi.org/10.1016/0021-9169(93)90030-3.

Moorcroft, D. R. (1979), Dependence of radio aurora at 398MHz on electron density and electric field, *Canadian Journal of Physics*, *57*(5), 687–697, doi:10.1139/p79-097.

Newman, A. L., and E. Ott (1981), Nonlinear simulations of type 1 irregularities in the equatorial electrojet, *Journal of Geophysical Research: Space Physics*, *86*(A8), 6879–6891, doi:10.1029/JA086iA08p06879.

Nicolls, M. J., R. Cosgrove, and H. Bahcivan (2014), Estimating the vector electric field using monostatic, multibeam incoherent scatter radar measurements, *Radio Science*, *49*(11), 1124–1139, doi:10.1002/2014RS005519.

Nielsen, E., and K. Schlegel (1983), A first comparison of STARE and EISCAT electron drift velocity measurements, *Journal of Geophysical Research: Space Physics*, *88*(A7), 5745–5750, doi:10.1029/JA088iA07p05745.

Nielsen, E., and K. Schlegel (1985), Coherent radar Doppler measurements and their relationship to the ionospheric electron drift velocity, *Journal of Geophysical Research: Space Physics*, *90*(A4), 3498–3504, doi:10.1029/JA090iA04p03498.

Ogawa, T., H. Mori, and S. Miyazaki (1976), Rocket observations of electron density irregularities in the Antarctic auroral E region, *Journal of Geophysical Research*, *81*(22), 4013–4015, doi:10.1029/JA081i022p04013.

Oppenheim, M. M., and Y. S. Dimant (2013), Kinetic simulations of 3-D Farley-Buneman turbulence and anomalous electron heating, *Journal of Geophysical Research: Space Physics*, *118*(3), 1306–1318, doi:10.1002/jgra.50196.

Oppenheim, M. M., Y. Dimant, and L. P. Dyrud (2008), Large-scale simulations of 2-D fully kinetic Farley-Buneman turbulence, *Ann. Geophys.*, *26*(3), 543–553, doi:10.5194/angeo-26-543-2008.

Ossakow, S. L., K. Papadopoulos, J. Orens, and T. Coffey (1975), Parallel propagation effects on the type 1 electrojet instability, *Journal of Geophysical Research*, *80*(1), 141–148, doi:10.1029/JA080i001p00141.

Pfaff, R., M. Kelley, B. Fejer, and M. Smiddy (1982), Rocket observations of coherent electrostatic waves on the topside of the auroral electrojet turbulent region, *Eos Trans. AGU*, *63*, 393.

Pfaff, R. F. (1995), Comparison of wave electric field measurements of two-stream instabilities in the auroral and equatorial electrojets, in *Plasma Instabilities in the Ionospheric E-Region. Proceedings of a workshop held at the Max-Planck-Institute für Aeronomie in Katlenburg-Lindau*, edited by K. Schlegel, p. 19, Cuvillier, Germany.

Pfaff, R. F., M. C. Kelley, B. G. Fejer, E. Kudeki, C. W. Carlson, A. Pedersen, and B. Hausler (1984), Electric field and plasma density measurements in the auroral electrojet, *Journal of Geophysical Research: Space Physics*, *89*(A1), 236–244, doi:10.1029/JA089iA01p00236.

Pfaff, R. F., M. C. Kelley, E. Kudeki, B. G. Fejer, and K. D. Baker (1987), Electric field and plasma density measurements in the strongly driven daytime equatorial electrojet: 2. Two-stream waves, *Journal of Geophysical Research: Space Physics*, *92*(A12), 13,597–13,612, doi:10.1029/JA092iA12p13597.

Pfaff, R. F., et al. (1992), The E-region rocket/radar instability study (ERRRIS): scientific objectives and campaign overview, *Journal of Atmospheric and Terrestrial Physics*, *54*(6), 779–808, doi:10.1016/0021-9169(92)90116-3.

Picone, J. M., A. E. Hedin, D. P. Drob, and A. C. Aikin (2002), NRLMSISE-00 empirical model of the atmosphere: Statistical comparisons and scientific

issues, *Journal of Geophysical Research: Space Physics*, *107*(A12), 1468, doi: 10.1029/2002JA009430.

Powell, M. J. (1970), A hybrid method for nonlinear equations, *Numerical methods for nonlinear algebraic equations*, *7*, 87–114.

Powell, M. J. D. (1964), An efficient method for finding the minimum of a function of several variables without calculating derivatives, *The Computer Journal*, *7*(2), 155–162, doi:10.1093/comjnl/7.2.155.

Providakes, J., D. T. Farley, B. G. Fejer, J. Sahr, W. E. Swartz, I. Hggstrm, . Hedberg, and J. A. Nordling (1988), Observations of auroral E-region plasma waves and electron heating with EISCAT and a VHF radar interferometer, *Journal of Atmospheric and Terrestrial Physics*, *50*(45), 339–356, doi: 10.1016/0021-9169(88)90019-0.

Reinleitner, L. A., and E. Nielsen (1985), Self-consistent analysis of electron drift velocity measurements with the STARE/SABRE System, *Journal of Geophysical Research: Space Physics*, *90*(A9), 8477–8486, doi:10.1029/JA090iA09p08477.

Rishbeth, H., and O. Garriott (1969), *Introduction to Ionosphere Physics*, International geophysics series, Academic Press.

Robinson, T. (1989), *The Heating of the High Latitude Ionosphere by High Power Radio Waves*, Physics reports, North-Holland.

Robinson, T. R. (1986), Towards a self-consistent non-linear theory of radar auroral backscatter, *Journal of Atmospheric and Terrestrial Physics*, *48*(5), 417–422, doi:10.1016/0021-9169(86)90118-2.

Rodriguez, J. V., and U. S. Inan (1994), Electron density changes in the nighttime D region due to heating by very-low-frequency transmitters, *Geophysical Research Letters*, *21*(2), 93–96, doi:10.1029/93GL03007.

Rose, G., et al. (1992), The ROSE project. Scientific objectives and discussion of first results, *Journal of Atmospheric and Terrestrial Physics*, *54*(6), 657–667, doi:10.1016/0021-9169(92)90104-S.

Rosenbluth, M. N., and N. Rostoker (1962), Scattering of electromagnetic waves by a nonequilibrium plasma, *Physics of Fluids (1958-1988)*, *5*(7), 776–788, doi: 10.1063/1.1724446.

Sahr, J. D., and B. G. Fejer (1996), Auroral electrojet plasma irregularity theory and experiment: A critical review of present understanding and future directions, *Journal of Geophysical Research: Space Physics*, *101*(A12), 26,893–26,909, doi: 10.1029/96JA02404.

Sahr, J. D., D. T. Farley, W. E. Swartz, and J. F. Providakes (1991), The altitude of type 3 auroral irregularities: Radar interferometer observations and implications, *Journal of Geophysical Research: Space Physics*, *96*(A10), 17,805–17,811, doi: 10.1029/91JA01544.

Sahr, J. D., D. T. Farley, W. E. Swartz, J. F. Providakes, and R. F. Pfaff (1992), Observations of 3-m auroral irregularities during the ERRRIS campaigns, *Journal of Atmospheric and Terrestrial Physics*, *54*(6), 809–818, doi: 10.1016/0021-9169(92)90117-4.

Salpeter, E. E. (1960), Electron density fluctuations in a plasma, *Physical Review*, *120*(5), 1528–1535, doi:10.1103/PhysRev.120.1528.

Salpeter, E. E. (1961), Plasma density fluctuations in a magnetic field, *Physical Review*, *122*(6), 1663–1674, doi:10.1103/PhysRev.122.1663.

Scherliess, L., and B. G. Fejer (1999), Radar and satellite global equatorial F region vertical drift model, *Journal of Geophysical Research: Space Physics*, *104*(A4), 6829–6842, doi:10.1029/1999JA900025.

Schlegel, K., and C. Haldoupis (1994), Observation of the modified two-stream plasma instability in the midlatitude E region ionosphere, *Journal of Geophysical Research: Space Physics*, *99*(A4), 6219–6226, doi:10.1029/93JA02869.

Schlegel, K., and J. P. St.-Maurice (1981), Anomalous heating of the polar E region by unstable plasma waves 1. Observations, *Journal of Geophysical Research: Space Physics*, *86*(A3), 1447–1452, doi:10.1029/JA086iA03p01447.

Schunk, R., and A. Nagy (2004), *Ionospheres: Physics, Plasma Physics, and Chemistry*, Cambridge atmospheric and space science series, Cambridge University Press.

Schunk, R., and A. Nagy (2009), *Ionospheres: Physics, Plasma Physics, and Chemistry*, Cambridge atmospheric and space science series, Cambridge University Press.

Sen, H. K., and A. A. Wyller (1960), On the generalization of the Appleton-Hartree magnetoionic formulas, *Journal of Geophysical Research*, *65*(12), 3931–3950, doi:10.1029/JZ065i012p03931.

Senior, A., N. D. Borisov, M. J. Kosch, T. K. Yeoman, F. Honary, and M. T. Rietveld (2004), Multi-frequency HF radar measurements of artificial F-region field-aligned irregularities, *Ann. Geophys.*, *22*(10), 3503–3511, doi:10.5194/angeo-22-3503-2004.

Siren, J. C., J. R. Doupnik, and W. L. Ecklund (1977), A comparison of auroral currents measured by the Chatanika radar with 50-MHz backscatter observed from Anchorage, *Journal of Geophysical Research*, *82*(25), 3577–3584, doi:10.1029/JA082i025p03577.

St.-Maurice, J. P. (1990), Electron heating by plasma waves in the high latitude E-region and related effects: theory, *Advances in Space Research*, *10*(6), 239–249, doi:10.1016/0273-1177(90)90257-Z.

St.-Maurice, J.-P., and R. Laher (1985), Are observed broadband plasma wave amplitudes large enough to explain the enhanced electron temperatures of the high-latitude E region?, *Journal of Geophysical Research: Space Physics*, *90*(A3), 2843–2850, doi:10.1029/JA090iA03p02843.

St.-Maurice, J. P., K. Schlegel, and P. M. Banks (1981a), Anomalous heating of the polar E region by unstable plasma waves 2. theory, *Journal of Geophysical Research: Space Physics*, *86*(A3), 1453–1462, doi:10.1029/JA086iA03p01453.

St.-Maurice, J. P., K. Schlegel, and P. M. Banks (1981b), Anomalous heating of the polar E region by unstable plasma waves 2. Theory, *Journal of Geophysical Research: Space Physics*, *86*(A3), 1453–1462, doi:10.1029/JA086iA03p01453.

St.-Maurice, J.-P., R. K. Choudhary, W. L. Ecklund, and R. T. Tsunoda (2003), Fast type-I waves in the equatorial electrojet: Evidence for nonisothermal ion-acoustic speeds in the lower E region, *Journal of Geophysical Research: Space Physics*, *108*(A5), 1170, doi:10.1029/2002JA009648.

Stauning, P., and J. K. Olesen (1989), Observations of the unstable plasma in the disturbed polar E-region, *Physica Scripta*, *40*(3), 325, doi:10.1088/0031-8949/40/3/012.

Sulzer, M. P. (1986), A radar technique for high range resolution incoherent scatter autocorrelation function measurements utilizing the full average power of klystron radars, *Radio Science*, *21*(6), 1033–1040, doi:10.1029/RS021i006p01033.

Swartz, W. E., and D. T. Farley (1979), A theory of incoherent scattering of radio waves by a plasma, 5. The use of the Nyquist Theorem in general quasi-equilibrium situations, *Journal of Geophysical Research: Space Physics*, *84*(A5), 1930–1932, doi:10.1029/JA084iA05p01930.

Thayer, J. P. (1998), Height-resolved Joule heating rates in the high-latitude E region and the influence of neutral winds, *Journal of Geophysical Research: Space Physics*, *103*(A1), 471–487, doi:10.1029/97JA02536.

Thid, B., and B. Lundborg (1986), Structure of HF pump in ionospheric modification experiments. linear treatment, *Physica Scripta*, *33*(5), 475.

Tsunoda, R. T., and R. I. Presnell (1976), On a threshold electric field associated with the 398-MHz diffuse radar aurora, *Journal of Geophysical Research*, *81*(1), 88–96, doi:10.1029/JA081i001p00088.

Unwin, R. S. (1967), The morphology of the VHF radio aurora at sunspot maximumIII: Movement of echoes, *Journal of Atmospheric and Terrestrial Physics*, *29*(12), 1581–1593, doi:10.1016/0021-9169(67)90110-9.

Vaskov, V., and A. Gurevich (1977), Resonance instability of small-scale plasma perturbations, *Zhurnal Eksperimental'noi i Teoreticheskoi Fiziki*, *73*, 923–936.

Vaskov, V. V., and A. V. Gurevich (1975), Nonlinear resonant instability of a plasma in the field of an ordinary electromagnetic wave, *Zhurnal Eksperimentalnoi i Teoreticheskoi Fiziki*, *69*, 176–188.

Volland, H. (1995), *Handbook of Atmospheric Electrodynamics*, v. 2, Taylor & Francis.

Wilczek, R., and S. Drapatz (1985), A high accuracy algorithm for maximum entropy image restoration in the case of small data sets, *Astronomy and Astrophysics*, *142*, 9–12.

Woodman, R. F., and J. L. Chau (2002), First Jicamarca radar observations of two-stream E region irregularities under daytime counter equatorial electrojet conditions, *Journal of Geophysical Research: Space Physics*, *107*(A12), 1482, doi:10.1029/2002JA009362.